

# **Analysis and Visualization in Multidimensional Microscopy**

Dissertation zur Erlangung des  
naturwissenschaftlichen Doktorgrades  
der Bayerischen Julius-Maximilians-Universität Würzburg

vorgelegt von  
Kolja Alexander Wawrowsky  
geboren in Düsseldorf  
Würzburg, 2007

Eingereicht am: .....

Mitglieder der Promotionskommission:

Vorsitzender: .....

Gutachter : Dr. habil. Rainer Wolf

Gutachter: Prof. Dr. Dieter Weiss, Universität Rostock

Tag des Promotionskolloquiums: .....

Doktorurkunde ausgehändigt am: .....



## Zusammenfassung

Die biologische Forschung befindet sich in einem Paradigmenwandel, in dem Entdeckungen immer mehr von Computeranalyse ermöglicht werden.

Entdeckungen in der biologischen Forschung wurden historisch gesehen durch direkte Beobachtung und mit Hilfe chemischer Analysemethoden gemacht. Heute sehen wir einen wachsenden Trend zur computerunterstützten Analyse und Visualisierung. Dieser graduelle Umschwung spielt sich auch in der Mikroskopie ab. Multidimensionale Laser Scanning Mikroskopie kann sehr komplexe Multikanalbilder von fixierten oder lebenden Präparaten aufnehmen. Neue Methoden (wie z.B. fluoreszierende Proteine) erlauben es, Genexpression und Proteinlokalisierung direkt sichtbar zu machen. Ionensensitive Farbstoffe ändern ihre Helligkeit mit der Konzentration der Ionen in der Zelle. Die konfokale Mikroskopie erlaubt es, diese Änderungen dreidimensional über die Zeit aufzunehmen.

Die hier vorgestellte Arbeit demonstriert die Anwendung speziell entwickelter Software für die Analyse multidimensionaler Daten. Die hierbei entwickelten Methoden wurden für Volumendarstellung, Ionenfluxanalyse und zur molekularen Modellierung eingesetzt.

Die Visualisierungsmethoden basieren auf einem multidimensionalen Datenmodell, um auch komplexe Daten verarbeiten zu können. Die Software benutzt Vektorverarbeitung und Multiprozessorunterstützung um Volumendarstellung schneller und interaktiv zu machen. Die Algorithmen beruhen auf Erkenntnissen der Wahrnehmungsforschung und erlauben es dem Anwender, eine Reihe von verschiedenen Darstellungsmodi zu kombinieren. Die Software wurde erstmals verwendet, um einerseits die Entwicklung der Hypophyse im Zebrafisch zu rekonstruieren, und andererseits die Degenerierung von Neuronen im Mausmodell bildlich zu verfolgen.

Kalziumfarbstoffe wurden schon länger zum Studium von Kalziumoszillationen in Zellen eingesetzt. Wir optimierten die Bildaufnahmemethode um Schädigungen der Zelle zu minimieren. Zellen wurden kontinuierlich in 45 Minuten Zeitintervallen aufgenommen und dabei wachsenden Dosen der zu untersuchenden Substanz ausgesetzt. Durch Korrelation von Dosis und Oszillationsamplitude konnten pharmakologische Wirkungskurven für jede einzelne Zelle ermittelt werden. Diese Methode hat wegen der hohen Sensitivität und Auflösung bis zur einzelnen Zelle Potential für pharmakologische Untersuchungen.

Mikrotubuli formen ein dynamisches Zytoskelett, das für Zellform und intrazellularen Transport zuständig ist und eine integrale Rolle bei der Mitose spielt. Eine besondere Eigenschaft der Mikrotubuli ist die laterale Interaktion. Mikrotubuli werden von Motorproteinen zu dichten Strukturen gebündelt. Um den möglichen Einfluß dieses Vorgangs auf die Organisation der Mikrotubuli zu testen, wurde ein fraktales Modell erstellt.

Dieses Modell demonstriert, daß die komplexe Organisation der Mikrotubuli in einigen Fällen allein mit dem Bündelungsprozess erklärt werden kann.

Zusammenfassend konnte in dieser Arbeit demonstriert werden, daß der Einsatz speziell entwickelter Software für Visualisierung, Datenanalyse und Modellierung zu neuen wissenschaftlichen Erkenntnissen führen kann.

## Summary

The live sciences currently undergo a paradigm shift to computer aided discoveries. Discoveries in the live sciences were historically made by either direct observation or as a result of chemical assays. Today we see a growing shift toward computer aided analysis and visualization. This gradual process happens in microscopy. Multidimensional laser scanning microscopy can acquire very complex multichannel data from fixed or live specimen. New probes such as visible fluorescent proteins let us observe the expression of genes and track protein localization. Ion sensitive dyes change intensity with the concentration of ions in the cell. The laser scanning confocal allows us to record these processes in three dimensions over time.

This work demonstrates the application of software analysis to multidimensional microscopy data. We introduce methods for volume investigation, ion flux analysis and molecular modeling.

The visualization methods are based on a multidimensional data model to accommodate complex datasets. The software uses vector processing and multiple processors to accelerate volume rendering and achieve interactive rendering. The algorithms are based on human visual perception and allow the observer a wide range of mixed render modes.

The software was used to reconstruct the pituitary development in zebrafish and observe the degeneration of neurons after injury in a mouse model.

Calicum indicator dyes have long been used to study calcium fluxes. We optimized the imaging method to minimize impact on the cell. Live cells were imaged continuously for 45 minutes and subjected to increasing doses of a drug. We correlated the amplitude of calcium oscillations to increasing doses of a drug and obtain single cell dose response curves. Because this method is very sensitive and measures single cell responses it has potential in drug discovery and characterization.

Microtubules form a dynamic cytoskeleton, which is responsible for cell shape, intracellular transport and has an integral role in mitosis. A hallmark of microtubule organization is lateral interactions. Microtubules are bundles by proteins into dense structures. To estimate the contribution of this bundling process, we created a fractal model of microtubule organization. This model demonstrates that morphology of complex microtubule arrays can be explained by bundling alone.

In summary we showed that advances in software for visualization, data analysis and modeling lead to new discoveries.

# Inhaltsverzeichnis

<i>Zusammenfassung</i>	<i>iii</i>
<i>Summary</i>	<i>v</i>
<i>Inhaltsverzeichnis</i>	<i>vi</i>
<i>Introduction</i>	<i>1</i>
<b>Outline of this thesis</b> .....	<b>2</b>
<b>Goals</b> .....	<b>2</b>
<b>Volume Investigation</b>	<b>4</b>
<b>Volume Rendering</b> .....	<b>4</b>
Volume Rendering Pipeline .....	5
Direct Volume Rendering Methods.....	6
Average Intensity Projection .....	7
Maximum Intensity Projection (MIP).....	7
Transparency and Opacity (Alpha) Rendering.....	8
Simulated Fluorescent Process.....	8
<b>Surface Rendering</b> .....	<b>9</b>
Isosurface.....	9
<b>Perception of Spatial Depth</b> .....	<b>9</b>
<b>Volume Visualization Software</b> .....	<b>10</b>
Single Purpose Visualization Applications .....	11
Programmable Volume Rendering Application .....	12
Visualization Frameworks and Libraries.....	12
<b>Multimodal Microscopy</b> .....	<b>13</b>
Imaging Modalities in Light Microscopy .....	13
Bright field Microscopy .....	13
Phase Contrast.....	14
Nomarski Contrast.....	15
Reflection Contrast .....	15
Fluorescence Microscopy .....	16
Multimodal Confocal Microscopy .....	16
<b>Software Technologies</b> .....	<b>17</b>
Object Oriented Programming .....	17
Objective C Language .....	18
Integrated Development Environment.....	18
OpenGL .....	19
OS X Operating System .....	20
<b>Computing Hardware</b> .....	<b>21</b>
Vector Processing.....	21

Graphics Processing .....	23
<b>Perceptual Rendering as a New Paradigm .....</b>	<b>24</b>
Compositing Multimodal Images .....	25
Synthesizing Depth Cues .....	26
<b>Application Architecture .....</b>	<b>28</b>
Multidimensional Storage and Processing .....	31
Visualization Framework .....	32
Application Logic .....	33
Processing Pipeline .....	34
Acceleration by Motorola AltiVec Vector Unit .....	34
Acceleration of Copy Operation .....	34
Acceleration of Color Interleaving .....	35
Benchmark Results for SIMD Processing .....	36
A Basic Volume Renderer .....	37
Volume Transforms .....	38
Intensity Transfer Function .....	38
Realtime Volume Compositing .....	38
<b>Visualization of Cytoskeletons .....</b>	<b>41</b>
Improved Detail .....	42
Shadow Maps and Modulated Alpha .....	44
Embryonic Zebrafish Lactotrophs .....	46
PTTG1 is not Neuroprotective .....	48
<b>Calcium Flux</b> .....	<b>52</b>
Optical Calcium Recording .....	53
Pharmacological Analysis .....	54
Screening Methods .....	54
Automated Ion Imaging .....	54
Live Cell Imaging .....	55
Calcium Channel Agonists .....	56
Calcium in Endocrine Cells .....	56
Calcium Channel Types .....	56
Calcium in AtT20 Pituitary Tumor Cells .....	57
Materials and Methods .....	58
Cell Culture .....	58
Confocal Cytosolic Calcium Imaging .....	58
Dose Response Acquisition .....	59
Measurement and Analysis .....	59
<b>Results .....</b>	<b>59</b>
Confocal Imaging .....	59
Validating Sampling Frequency .....	60
Recording Calcium Oscillations .....	61
Controls for 45 min Interval .....	63
Dose Response .....	66

Discussion.....	67
<b>Modeling Microtubule Organization</b>	<b>69</b>
Introduction to Microtubule Cytoskeleton.....	69
Multidimensional Analysis.....	70
<b>Basic Facts about Microtubules and the Cytoskeleton</b> .....	<b>71</b>
Biochemistry of Tubulin .....	71
Tubulin Polymerization .....	72
Treadmilling.....	72
Dynamic Instability .....	72
Microtubule Associated Proteins.....	73
Motor Proteins.....	73
Terminology of Microtubule Arrays .....	73
Differences of Animal vs. Plant Tubulin.....	74
Microtubule Dynamics.....	75
Microtubule Organizing Centers.....	78
Structure and Function of the Kinetochore.....	79
Microtubule Motors as Organizing Factors .....	79
Transport Function of Motor Proteins.....	80
Chromosome movement during mitosis.....	80
Morphology and Function of the Centrosome.....	81
Microtubule Self-Nucleation.....	82
Structure and Dynamics of the Mitotic Spindle .....	82
Microtubule Self-Organization .....	83
Dynamics of the Kinetochore Fiber.....	84
Particle Translocation Studies .....	87
Pharmacological Effects on Spindle Dynamics.....	87
Special Properties of Plant Cytoskeletons.....	88
Intracellular Motion.....	89
<b>Model Systems for Organization</b> .....	<b>89</b>
Static Models.....	90
Dynamic Models.....	90
Euklidian Models.....	90
Fractal Models.....	90
L-systems.....	91
<b>Material and Methods</b> .....	<b>92</b>
Specimen Preparation.....	92
Video Systems .....	92
Tube Cameras .....	93
CCD Cameras .....	93
Signal Properties of the Video Signal .....	94
Multimedia.....	94
Analog to Digital Signal Conversion .....	94
Image Processing.....	95
Analog Signal Processing.....	95

Image Compression.....	96
Lossless Image Compression Techniques .....	97
Image Analysis .....	97
Basic Morphology of Microtubules During the Cell Cycle.....	98
Motion Analysis at the Kinetochore .....	98
MT Bundling .....	100
<b>Microtubule Self-Organization.....</b>	<b>103</b>
Fragments May Work like a Complete Systems.....	104
<b>Describing Microtubule Arrays with L-System Fractals.....</b>	<b>106</b>
<b><i>Conclusion</i></b>	<b>109</b>
<b><i>References</i></b>	<b>110</b>
<b><i>Danksagung</i></b>	<b>120</b>
<b><i>Lebenslauf</i></b>	<b>121</b>
<b><i>Publikationsliste</i></b>	<b>122</b>
<b><i>Ehrenwörtliche Erklärung</i></b>	<b>124</b>

*"It would be madness and inconsistency to suppose that things not yet done can be done, except by means not yet tried"*

- Sir Francis Bacon

## **Introduction**

Inquiry and knowledge of mankind have historically been associated with light. Plato uses light and shadows as a metaphor of enlightenment in Book VII of his work "The Republic". We learn by observation and experimentation. Optical instruments expand our observations into the otherwise invisible and open new horizons. One of these instruments is the light microscope. The word microscope itself is derived from the Greek (*mikron* = small and *skopein* = seeing). Galileo Galilei created an early compound microscope in 1609 by combining a convex and concave lens. He called it "occholino". Anton van Leeuwenhoek (1632 - 1723) is credited as the founder of microbiology not in small part for his use of early single-lens microscopes. It enabled him to discover cells and single celled organisms he called "animalcules".

Working with the light microscope is a unique experience. We look through the oculars and marvel the wonders of nature. Ghostly images of bright fluorescent colors may appear. The microscope greatly improves the way we see things. It lets us discover and eventually understand the processes of life. Many discoveries in life sciences were only possible by technical advances in microscopy. As one of the earliest instruments specifically designed for scientific inquiry, the light microscope became an icon for biomedical research.

Compared to x-rays and other forms of electromagnetic radiation, light is a very versatile imaging radiation. Optical imaging is non invasive. Contrast can be generated by different modalities such as absorption, phase shift or polarization. Fluorescent dyes may be used as molecular probes. This versatility has propelled researchers and engineers to advance the microscope substantially and create novel imaging techniques.

The physicist Ernst Abbe, instrument maker Carl Friederich Zeiss and glass chemist Otto Schott collaborated to produce the first modern light microscope in the 1870s. In 1886 Zeiss had already sold over 10,000 instruments. The convergence of advanced optics such as aspherical lenses, developments in electronics and sensors, and the computer revolution propelled microscopy to new heights. Marvin Minski had conceptualized confocal scanning microscopy in 1953. But confocal imaging became feasible only after computers were powerful enough to process the imaging data. Today confocal microscopes acquire multidimensional images in space, time, spectral and, fluorescent lifetime domains.

As microscopy transitioned into the digital age, digital image processing and analysis became vital. Analysis of three-dimensional confocal images is impossible without volume visualization. Visualization and analysis techniques, however, have not kept pace with rapid advances in imaging and detection methods. The mainstream software used today is still based on methods that were initially developed for medical imaging. These are inadequate for multidimensional and multi-modal microscopy.

Computer technology advanced rapidly during the last decade. The number of transistors on a microchip roughly double every two years, an observation made by Intel cofounder



Gordon Moore and dubbed Moore's law. Rapid progress in computing power allows us to develop software that was unthinkable only a few years ago. The computer has the capability to take complex data and process it rapidly to create advanced visualizations.

We take advantage of the confluence of advances in digital microscopy, computer hardware and software methodologies to visualize, analyze and model biological processes in novel ways. Integration of molecular biology and visualization methods opens new doors to *in vivo* observations. Image processing and analysis let us quantify processes in single cells on a molecular level. Fractal modeling provides us with the tools to describe molecular organization of cytoskeletons.

This work demonstrates the impact of bioinformatics driven advances in visualization, measurement, and modeling for scientific discovery.

### ***Outline of this thesis***

The thesis is divided into three independent parts: Volume investigation, calcium flux analysis and modeling of microtubule organization. Each section represents a different area of cell science: morphology, physiology, and molecular modeling respectively. Each area demonstrates how software can enhance the scientific discovery process. Imaging and biochemistry are two important complementary technologies. Fluorescent probes work as biological sensors for gene expression, protein localization, ion concentration, and molecular interaction. Imaging microscopy provides the tools to image, record, and measure fluorescent intensity and localization of these probes.

Software represents the glue that takes the imaging results and provides interactive visualization, quantitative analysis, and simulations of molecular mechanisms.

### ***Goals***

The goal of this project is to develop and employ visualization and analytic methods designed for scientific discovery in multidimensional multi-modal microscopy. Multidimensional image acquisition is a recent development in microscopy. We still lack adequate tools to fully analyze the data.

Many scientific fields such as meteorology or particle physics use multidimensional visualization. However, few of these methods are applicable to microscopy. Medical imaging works with single modality acquisition and dimensions limited to space and time. Visualization methods for medical data are not designed for multi-modal and higher dimensional data. This makes medical visualization software and techniques of limited use for microscopy.

Drawing on advances in software development techniques, computer graphics, molecular probes and microscopy we developed novel methods for visualization and data analysis.

Visualization methods were specifically designed for multi-modal confocal data. We apply those methods in several scientific projects and present the results. Advances in visualization improve the way we observe temporal and spatial relationships of processes taking place in biological specimen.

Advances in analysis let us quantify pharmacological effects and characterize molecular interactions. The project focuses on analysis and visualization in four specific areas:

1. Visualization of three and four dimensional multi-modal confocal images
2. Analysis of protein-protein interactions
3. Analysis of pharmacological effects on ion fluxes
4. Modeling organization of microtubules

Our developments present advances over already existing software and visualization methods and are based on practical experience. We drew on the advances of diverse fields such as software engineering, computer graphics, molecular probes, biological imaging, and mathematics. Consideration of human visual perception and psychology played an important role in the design of new visualization methods.

## **Volume Investigation**

Volume investigation describes the tools used to analyze data in three or higher dimensional diagnostic imaging (1). Computer Aided Tomography (CAT) and Magnetic Resonance Imaging (MRI) are examples of medical imaging techniques for volumetric imaging. Optical coherence tomography (OCT) and confocal microscopy images at high magnifications are examples of methods for biological samples.

Standard light microscopic methods create two-dimensional images and provide little information about the three-dimensional organization of cells and tissues. Confocal Laser Scanning Microscopy (CLSM) and multi-photon microscopy present advances over these methods by improving axial resolution and enabling multidimensional multi-modal acquisition.

However, analysis and visualization of multi-modal data is still in its infancy. Historically, visualization research focused on overcoming technical and computational limitations of computing hardware (2). Technical considerations are essential for a good volume rendering application, but represent only the first step. We present a review of current state in software development and visualization technology as a foundation for our improvements.

Optical properties of biological objects are often very different from everyday objects. Our understanding and comprehension of morphological features of biological samples, however, are essential for scientific discoveries. We know little a priori about morphology and physiology of new samples and have to account for two sources of error in visualization: One is the introduction of artifacts by the visualization application. Visualization artifacts can lead to a misinterpretation of morphological features. The second error is an inadequate quality of the visualization. The final image may not include important detail or obscure structures.

We will present a brief overview of currently used volume visualization techniques and evaluate the tradeoffs for each method. Finally, we review findings in human visual perception research to understand how we can improve visualization methods.

## **Volume Rendering**

Volume rendering transforms discretely sampled volumetric data into a two-dimensional image (3). The volume data is the result of imaging an object in three or more dimensions. Examples include magnetic resonance imaging (MRI), confocal microscopy and optical coherence tomography (OCT). Volume rendering shares techniques with computer graphics and image processing.

Traditional computer graphics were based on graphics primitives including lines, points and polygons. Those primitives can be combined in a variety of sizes, shapes, and colors to synthesize a scene. Addition of textures and shading to the pure geometric data enhances realism and adds detail.

Generating two-dimensional images from virtual scenes is called rendering. Rendering is a computationally expensive process. The complexity of the scene and the capability of the rendering hardware determine the amount of rendering time.

Two-dimensional surface patches represent all three-dimensional objects in virtual scenes. Objects resemble hollow shells and do not contain any information about internal structures. Slicing through such virtual objects would reveal nothing, and it would be difficult to modify surface models to add internal structure.

Direct volume rendering was invented to solve this problem. A volume rendering pipeline processes raw volume data and projects it onto a two dimensional plane to create a rendering. A rendering can be displayed on a screen, saved as a digital picture, or printed out on paper. The pipeline can produce different type of renderings depending on input data, application requirements, and output medium.

### **Volume Rendering Pipeline**

Volume rendering is achieved by a linear sequence of operations. This sequence is called a pipeline. Each operation is optional and can be left out if required. The result of each operation is passed on to the next processing step within the pipeline. The traditional pipeline consists of these operations (3):

1. Segmentation - The values in a volume are selected to either become part of the final rendering or not, based on a range of criteria. The simplest selection operation is a thresholding operation, which only passes values to the next step if they exceed a certain threshold value. Segmentation may need human intervention, if the data is very complex.
2. Gradient - The gradient is a measure of local change in intensity. The larger the change, the higher the gradient value. The gradient may or may not encode the direction or orientation of the change. Edges and boundaries often have large changes in intensities and cause large gradient signals. This makes gradient signals useful for segmentation. Gradients can be used to find boundaries between different material.
3. Resampling - This operation takes the output of the previous processing steps and simplifies the geometry, e.g. by decimating triangle strips (4). This saves storage space and accelerates processing. However, it can lead to loss of resolution.
4. Classification - The classifier modifies the data according to a set of rules. Changes include, but are not limited, to: intensity, opacity, and color.
5. Shading - Shadows and highlights (normally caused by light reflection) are created by applying a lighting model to the results of the previous stages. Lighting models can include multiple point light sources and ambient illumination terms.

6. Compositing - This step takes all elements from the pipeline and composites them in order to create the two-dimensional rendering. Input values contain information about intensity, color, depth and density. Multiple buffers are used for compositing depending on the render mode. Buffers include alpha (opacity), color, and depth values. The compositing process can be ordered e.g. from back-to-front (BTF) or front-to-back (FTB). Geometric data can be drawn in random orientation. Random orientation drawing relies on the depth buffer to create correct occlusion.

This pipeline uses a linear flow of processing steps. Parallel working processing units accelerate a single processing step in the pipeline. The units achieve this by working on several pieces of data simultaneously using vector operations. Multiple processors can be combined to work sequentially and in parallel to create a complete multistep rendering pipeline in hardware (5). Modern graphics cards use both principles to accelerate volume rendering (6).

### **Direct Volume Rendering Methods**

Direct volume rendering (DVR) methods create renderings of entire volumetric data sets without converting the data into geometries (7). Common volume rendering methods parallel physical optical models (8). They simulate how a sample emits, scatters, or occludes light. Volumetric data is typically a scalar field of values. The volume rendering method first maps these values to optical properties such as color intensity and opacity. The renderer integrates the optical effects along viewing rays into the volume. The result is called the volume rendering integral. Volume rendering is based on those three basic optical properties: absorption, emission and scattering. In case of absorption voxels are considered to consist of light absorbing black, or colored, particles. The emission model assumes voxels are particles that emit light of different color and intensity. The scattering model calculates surface normals and models light scattering off particle surfaces. The light source can be modeled as directional point sources, or as diffuse and ambient.

These three optical models can be combined to produce more complex and realistic lighting models. All direct volume rendering model integrate a combination of optical properties along the viewing axis, even if no explicit viewing rays are calculated by the renderer.

One method that uses explicit rays is called ray casting (9). It calculates the integral along a rays cast parallel to the vector originating from the eye and cast through the pixel into the volume for each pixel in the image. Splatting is the opposite method (7). It calculates the contribution of each voxel to each pixel in the image, in effect "splatting" the color and intensity onto the image.

The volume is represented by an evenly sampled array of discrete values. To avoid interference effects between the sampling frequency of the renderer and the sampling frequency of the data, filtering and interpolation might be required (10). Direct volume rendering methods are especially suited to confocal imaging data (11). The confocal scanning process samples objects in a regular spaced grid of voxels. The raw imaging data is represented as scalar values on this regular grid.

The main disadvantage of direct rendering is the enormous amount of data processed for each rendered frame (11). A small confocal dataset of 30 megabyte (MB) size rendered with a frame rate of 15 frames per second would require a minimum memory bandwidth of 450 MB per second. If data needs to be transferred several times between different processing units, required bandwidth is a multiple of the transfers. This restricted volume-rendering applications initially to expensive and specialized graphics workstations.

Recent advances in chip technology and bus architecture for personal computers (PCs) were mostly driven by the developments in the commercial gaming industry (12). Gaming requires high frame rates and detail, similar to DVR. These advances allow DVR applications to run on many standard PCs (11). Enabling technologies include Intel's advanced graphics port (AGP), PCI express, and programmable graphic chip designs. Modern graphic chips have multiple parallel working texture units and some limited per-fragment operations. They meet and exceed the processing requirements even for large datasets.

These acceleration techniques allow calculation of the volume rendering integral much faster than a general-purpose processing unit (6). They can simulate physical lighting models in hardware. Volume rendering applications offer several models. The most common ones are average intensity projection, maximum intensity projection, and alpha rendering.

### **Average Intensity Projection**

The simplest method for direct volume rendering is the average intensity projection, also referred to as X-ray projection. The algorithm simply calculates average intensity values along each ray. Ray tracing, ray casting or shear warp transforms can be used to calculate the result. There are no parameters for the user to adjust. Projections of fluorescence microscopy data resemble very closely to what can be observed by normal wide-field fluorescence microscopy. Rendered images appear familiar to users of conventional video microscopy or photographic methods. Every structure contributes equally to the final rendering, depending only on its locally imaged intensity including out-of-focus blur and noise. Another advantage is that averaging data over multiple planes smooths out image noise. Quality of renderings remains generally higher in comparison to wide-field images because the confocal microscope removes out-of-focus blur, which commonly plagues normal wide-field images. Fast and easy to use, this reconstruction method is widely accepted as the gold standard for scientific publications of fluorescent data and images.

However, average intensity projection is not without shortcomings. By simple averaging voxel intensities any existing depth information is lost, similar to the effect of standard X-ray images. The averaging effect also averages out small structures, textures, dots, or speckles, even if they are very bright. This can be partially compensated by limiting the stack size, so that fewer planes are averaged.

### **Maximum Intensity Projection (MIP)**

Maximum intensity projection is a method where the voxel with the highest intensity along the viewing ray is selected. The resulting projection only contains the brightest voxels of the original 3-D data. This is in essence a topographic projection of a surface connecting

the brightest data points of the original dataset. Only those selected voxels form the final 3-D rendering, and all other data is discarded.

The advantage of this algorithm is the preservation of fine detail like small dots and fibers. Especially cell biological samples contain small dotted structures. These are very important and make this rendering method the method of choice for high detail preservation. It produces significant artifacts, though. Since only one pixel is chosen along the viewing ray it acts like a segmentation algorithm and can completely suppress important data. Depth information is not only lost, but bright structures in the background can “jump” into the foreground and obscure foreground data. Background noise is amplified to the maximum since the brightest and noisiest pixels are selected for final display.

Maximum intensity projection is widely used in publications where punctuate staining or other highly localized structures are of interest. It requires high quality and low noise original data such as data from the cytoskeleton, membrane receptors, or chromosomes.

### **Transparency and Opacity (Alpha) Rendering**

Transparency rendering is similar to the average intensity projection in that all voxel values are involved in producing the final image. But it introduces the important concept of opacity. The normalized value for opacity from 0.0 to 1.0 is called alpha value, hence the term alpha rendering. Transparency rendering can take different forms. In its simplest incarnation, a data set consists exclusively of opacity values. All voxels are assumed to have a uniform color and brightness, which is being modulated by the alpha value. The final projection is calculated by compositing all opacities into the 2-D image. A more sophisticated approach assigns an alpha value to each voxel in addition to the color value. This approach is more flexible and allows transformation of opacities independently of color intensities.

### **Simulated Fluorescent Process**

Simulated fluorescent process (SFP) is a combination of alpha and average intensity projection (13). In this case, the volume rendering integral is calculated in two steps. In the first step it is assumed that voxels absorb light, and that the light source is directional. The result of this operation is called the emission volume. It is rendered with the average intensity projection. A backplane can be displayed to create a shadow. SFP images combine some of the advantages of surface rendering with DVR. The absorption process creates shadows that modulate surface features.

The SFP algorithm, however, found limited application. It has several problems. The inner volume of thick samples becomes too dark because most of the light is absorbed on the surface. This limits it to thin samples. Even low levels of noise create renderings that appear fogged. Noise absorbs light in the first processing step and appears as fluorescent fog in the second step.

Dual processing requirements prevent any significant hardware acceleration and make the algorithm slow. As a result only two software applications implement SFP: FreeSFP by Scientific Volume Imaging BV (Hilversum, Netherlands) and Imaris by Bitplane (Zurich, Switzerland).

## ***Surface Rendering***

Surface rendering is fundamentally different from direct volume rendering, because it relies on artificially calculated surface data. This data is typically computed using the marching cube algorithm (14). This algorithm converts volume data into geometric surfaces, or more precisely: triangle strips. The advantage is that geometric triangle data has lower memory requirements and works well on older systems that do not support large textures. However, since the data is converted from volume to surface, significant artifacts can be introduced. Surfaces often look artificial and cartoonish. The surface patches are amenable to assign material properties. Many programs offer options such as metallic, plastic or painted surface. While these attributes make sense in engineering and product design applications, they are of little use to the live scientist.

Since surfaces delineate a volume, the geometric data are used to calculate morphometric parameters such as volume, surface area and surface roughness. However, morphometric analysis is not a goal in our project.

## **Isosurface**

Isosurfaces are calculated by simple thresholding. The user has to select intensity threshold levels for image data, and surface (patch-) data is generated at any border along the threshold values. Surfaces are opaque, virtual light sources create surface shading, and drop shadows and partial transparency (alpha-blending) can make otherwise obscured structures visible. This method, however, falls short for most biological samples. To generate meaningful surface patches, structures need to be clearly defined and noise free. Severe artifacts are common iso-surface reconstructions as most biological structures are at, or beyond, the resolving power of the light microscope. Partial resolution and small fluorescent signal lead to small signal-to-noise ratios and significant high frequency noise. This makes reliable surface patch generation very difficult.

## ***Perception of Spatial Depth***

Depth perception combines all visual clues that our visual system uses to decode spatial depth (15). It can be grouped into two categories: monocular and binocular depth cues. Monocular cues exist even in a two-dimensional representation of a three-dimensional scene and require the information of the image from one eye only. Binocular cues require input from both eyes. Binocular cues are stereopsis and convergence. However, since we create a visualization application for standard output devices which are generally two-dimensional, we concentrate on monocular cues.

Monocular cues can be divided into two groups: size dependent and size independent cues. Size dependent cues use the fact that objects and patterns appear smaller in the distance. These cues are:

1. Relative size: objects closer to the observer appear larger than object further away.
2. Perspective: a linear geometry such as parallel lines appear to converge in the distance.
3. Texture gradient: patterns appear to compress toward the distance.



Size independent depth cues are based on the optical properties of objects:

1. Shadow: There are two kinds of shadows. Cast shadows are projections of opaque objects onto the surface inside the scene. Reflection of light depends on the angle the surface is at in relation to the light source. Differences in reflectivity create modulated surface shadows. Both types of shadows create important depth cues in complex scenes.
2. Interposition and Occlusion: Close objects occlude distant objects.

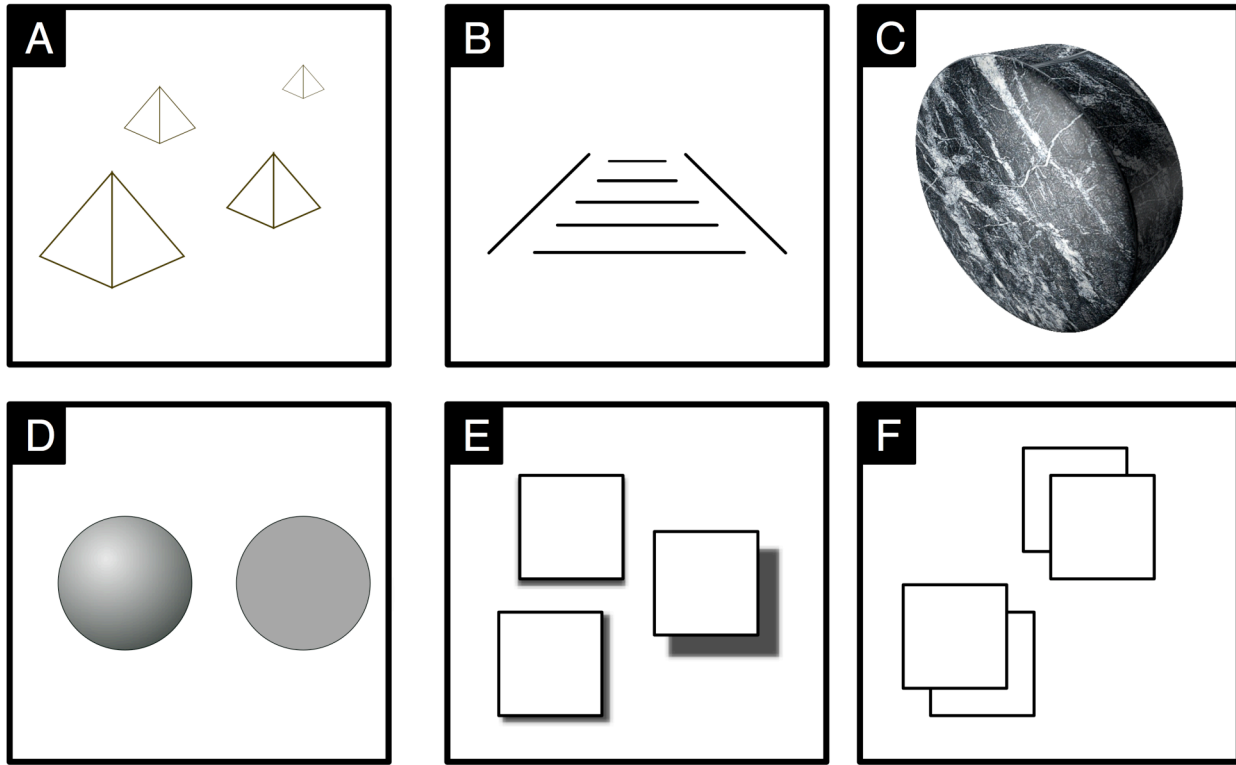


**Figure 1: Monocular Perception of Depth**

*The first row shows size dependent depth cues. A) Distant objects appear smaller than closer ones. The relative size creates perceived depth. B) Perspective foreshortening shows the convergence of parallel lines in the distance. C) Differences in texture gradients let us perceive the shape and orientation of objects. The second row shows size independent depth cues. D) Highlights and shading modulate the surface intensity. We tend to perceive the shape of objects through modulation of intensity. E) A cast shadow and its displacement makes us perceive the relative spatial arrangement. F) Occlusion shows the relative spatial arrangement of overlapping objects. Adapted from (16)*

## **Volume Visualization Software**

A wide variety of volume visualization software is available. Visualization software can be grouped into three categories:

1. Single purpose visualization applications
2. Programmable visualization applications

### 3. Visualization frameworks and libraries

Visualization applications have to balance ease of use with capability and flexibility. The more flexible an application becomes, the steeper the learning curve gets. Complexity of scenes is another differentiating factor. A scene is the collection of all elements that appear in the final rendering. The simplest scenes contain a single element such as a volume cube. More complex scenes consist of hundreds of elements that can be individually manipulated. An example is the computer model of a car where every part can be changed individually. A graph is a data structure that describes and maintains the relationships and position of elements in a scene. The scene graph is an important concept in computer graphics. A processing pipeline is an optional element in visualization applications. The pipeline converts and filters the raw data into a different representation. Digital filter designed for computer vision and image processing can be included in the processing pipeline.

#### Single Purpose Visualization Applications

Because our focus is visualization in confocal microscopy, we will concentrate on applications that support this field. Several commercial and free software packages are available. Rendering and processing capabilities vary significantly among those packages. Software that focuses on visualization in microscopy are Voxx(11) and Imaris (17).

Software	X-Ray	MIP	Alpha	SFP	Isosurface	Slicing	Mixed Mode
Amira					+	+	
Imaris	+	+	+	+	+	+	+
FreeSFP				+			
Volocity	+	+	+			+	
Voxx		+	+				

**Table 1 Visualization Applications and Render Modes**

*The table shows, which render modes are supported for each rendering application. Note that only Imaris supports all modes. All packages support state-of-the-art volume rendering and hardware acceleration, but are limited to three-dimensional datasets and a single imaging modality. A less capable application is Volocity (Improvisation, Coventry, England) that was developed for ease-of-use.*

Other more specialized systems include Amira, a system designed to "implement a complete set of methods and algorithms for the computer based generation and treatment of explicit geometric representations of anatomical structures from three dimensional image data (8). Amira is different from other software packages as it is a versatile morphometry application. It has limited support for direct volume rendering and visualization but creates an excellent framework for quantitative analysis. Table 1 summarizes the rendering capabilities of all popular visualization packages.

## **Programmable Volume Rendering Application**

Application Visual System (AVS) (18) and OpenDX (IBM Research, White Plains, New York) are two examples of visualization software with broad application. Both use a data-flow paradigm in the user interface to create and manipulate processing and visualization steps. Applications span such diverse areas as fluid dynamics, earth sciences, operational analysis, and climate modeling. These packages are very flexible. Users can graphically build custom applications by using pre-defined modules. These modules can be connected to represent the data flow through the network. However, rendering viewers are modules with fixed functionality in these applications. Direct volume rendering is limited and cannot be mixed with geometry. These general-purpose visualization systems are traditionally multi-platform systems and have a steep learning curve for users. The multi-platform requirement leads to severe compromises in design. Only the smallest common denominator of all targeted systems is implemented. A steep learning curve is a result of the very wide application spectrum that these systems endeavor to support.

Leica Microsystems Heidelberg (Mannheim, Germany) used pre-configured AVS modules for earlier versions of the confocal software. Their limitations became clear early on in development. AVS lacked a way to combine multiple monochrome channels into a color picture. A custom extension developed to combine channels lead to artifacts in opacity modes. These problems could not be solved. Furthermore, the time behavior of the AVS renderer could not be controlled, and aborting a lengthy rendering process was impossible. These and other problems prompted Leica Microsystems to abandon the project.

## **Visualization Frameworks and Libraries**

The vast majority of graphics frameworks are intended for development of computer games. These libraries are generally not suitable for scientific software development. A flexible and advanced framework designed for scientific visualization is the visualization toolkit (VTK). It is open source, was developed by a consortium of companies and universities, and is maintained and distributed by Kitware (Clifton Park, New York). The framework includes DVR and surface rendering and extensive image processing capabilities.

Another commercial framework for surface visualization is Open Inventor, which was originally developed by Silicon Graphics Inc. (Mountainview, California). It is an object oriented graphics development framework for the C++ language, and it has a scene database that manages geometry data. It is distributed by Mercury Computer Systems Inc. (San Diego, California). The Amira software is based on Open Inventor.

VTK and Open Inventor are high-level graphics libraries. Low-level libraries are usually bundled with operating systems. An exception is Microsoft Windows where every hardware supplier delivers their own set of dynamically linked libraries (DLLs). Low-level libraries encapsulate hardware capabilities and make it available to the programmer. Two examples are OpenGL and Direct3D. OpenGL is maintained by a consortium and available on many platforms. Direct3D is only available for the Windows operating system.

## **Multimodal Microscopy**

Light microscopy is a very versatile tool for *in vivo* imaging especially on a cellular and tissue level. The versatility of light enables many modalities in live cell imaging. Historically, contrasting methods such as phase contrast(19) and differential interference contrast DIC (20) were used for live cell observation. The advent of fluorescence microscopy in combination with fluorescent dyes (21) and, more recently, GFP fusion proteins (22) revolutionized our ability to observe molecular processes *in vivo*. Molecular probes for physiological imaging such as ion sensitive dyes (23) or engineered fluorescent proteins (24) give new insights into cellular physiology.

Fluorescence lifetimes of probes are known to be sensitive to numerous chemical and physical factors such as pH, oxygen, temperature, ions, polarity, and binding to macromolecules (25). Depth is added as a spatial dimension to *in vivo* imaging by laser scanning confocal microscopy or, even better, two-photon imaging, as both increase axial resolution (26). Fluorescence nanoscopy increases spatial resolution, thus breaking the diffraction limit (27). Three-dimensional time-lapse imaging is becoming routine and adds time as the fourth dimension in combination with confocal imaging (28). Live observation of molecular processes beyond the optical resolution can be achieved by fluorescence resonance energy transfer FRET (29).

Penetration depth of light is limited to a few hundred microns. Optical coherence tomography (OCT) overcomes this limit to some degree (30). It performs high-resolution, cross-sectional tomographic imaging of microstructure in biological systems. OCT can achieve image resolutions of 1-15  $\mu\text{m}$  with a penetration depth of 2 to 3 mm in tissue. Many imaging modalities can be combined to correlate different aspect of physiology and morphology.

## **Imaging Modalities in Light Microscopy**

Contrasting methods have to be selected according to the optical properties of the investigated structures. Preparation of biological samples is crucial to achieve the best conditions possible. Contrast can be generated by optical methods such as phase shift and polarization, or by the application of dyes.

## **Bright field Microscopy**

Bright field microscopy is the most common method to study stained samples. Stains color biological structures by absorbing wavelengths of light differentially. If the stain absorbs all wavelengths equally it appears black. Samples that are either naturally or artificially stained are called amplitude objects, since they decrease the amount of light transmitted (=amplitude).

Another type object that can be visualized in bright field microscopy are light scattering objects. White light scatters depending on the wavelength and the size of the scattering particles. Scattering occurs when light travels through accumulation of objects much smaller than its wavelength and with resonance properties higher than those of visible light. This type of scattering is called Reighleigh scattering. Reighleigh scattering can be caused by structures stained with colloidal gold. Gold particles scatter the blue light nearly

10 times as much as red light. Therefore areas with accumulations of colloidal gold appear reddish.

The maximum resolution in bright field microscopy can be described by assuming the illuminated specimen as a collection of infinitesimally small points. Each point creates a diffraction pattern. The central part of the pattern is called the Airy disk; a bright spot surrounded by alternating circular minima and maxima. Mathematically, the Airy disc can be described by the Fourier transform of a small circular hole. The intensity distribution of the Airy disc pattern is:

$$I = \frac{\pi d \sin(\psi)}{\lambda}$$

An important relationship is that the angular width of the Airy disk is, assuming the maximum extends to the first minimum:

$$\sin(\theta) = \frac{1.22\lambda}{nd}$$

The resolution of two adjacent points is usually determined by the Rayleigh criterion. It states that two Airy discs are resolvable when the central maximum of one point coincides with the first minimum of the other.

## Phase Contrast

Fritz Zernicke developed the classical phase contrast microscope during the 1930s. This setup exploits optical properties of biological objects that cannot be visualized by bright field microscopy, as the human eye is not sensitive to phase changes. The system converts phase differences of light into differences of intensity.

Many biological samples such as cells and sub-cellular components like vesicles or organelles have a different refractive index than the surrounding media. The speed of light is smaller in media with a higher refractive index, and therefore light is retarded in comparison to light waves traveling through media with a lower refractive index.

To visualize these differences, the phase contrast microscope has two elements:

1. The specimen is illuminated through an annulus of light. An annular aperture is located at the aperture stop of the condenser.
2. A matching annular phase plate is mounted at the focal plane of the objective lens.

The phase plate virtually contains an annular groove. The plate itself is a 1/4 wavelength plate. Coating material in the groove reduces the amplitude of light passing the groove by about 75%. At 100% of absorption the microscope would work as a dark field setup. The interference of "direct" light passing through the groove and "deviated" light passing through the rest of the plate produces an interference known as positive phase contrast. Phase objects with a higher refractive index appear dark against a bright background. As part of the deviated light happens to pass the phase plate, each phase object is depicted with a halo around it.

Phase contrast images are excellent for detection of small phase objects in thin preparations. These small objects are dark with a contrasting halo around and lend

themselves to digital image enhancement. Differential digital filtering specifically enhances image contrast of these particles and provides excellent contrast for automated detection methods.

### **Nomarski Contrast**

Nomarski contrast is another type of phase contrast (20). It is also called differential interference contrast (DIC). The microscope has to be fitted with two polarizers and two Wollaston prisms.

The Wollaston prism is at the heart of the DIC microscope. It is made of birefringent material, usually Calcite. Calcite has a different refractive index depending on the polarization angle of light. Cementing two wedges of calcite forms the Wollaston prism. At this internal cemented surface light is split into two diverging beams. One beam is called the specimen beam, the other the reference beam. The reference beam passes the sample at an offset compared to the specimen beam. In the upper stage of the microscope the two beams are reassembled by an exactly matching Wollaston prism, which serves as a beam combiner. If the specimen contains phase differences then reference and specimen beam are shifted against each other. This leads to interference of the two beams. If we use polarized light as a light source, a phase shift leads to an elliptical polarization, or if both waves are shifted by  $1/4$  wavelength to circular polarization. A crossed polarizer extinguishes all beams where the phase shift between the two beams is zero. Beams with phase shift would partially pass through according to the degree of elliptical polarization (= retardation). If the shift is larger than  $1/4$  wavelength the transmission would decrease again until it reaches total extinction at  $1/2$  wavelength.

The differential image produced by the DIC microscope depends on the rate of change of the refractive index in the sample. This contrast is directional since polarization only changes in one direction. It is beneficial to orient the biological specimen properly to observe the wanted structures at the highest possible contrast. Orientation of structures perpendicular to the polarization axis does not generate contrast. Mathematically, the intensity of DIC images is represented as the first derivative of the optical path difference. Taking an amplitude image and calculating the derivative can produce a pseudo DIC image.

### **Reflection Contrast**

Reflection contrast is the simplest setup of all introduced contrasting methods. Light is simply transmitted through the microscope lens, and the light reflected in the specimen forms an image. Unfortunately most microscope lenses exhibit a lot of internal reflections despite multiple layers of antireflex coating. We used the Zeiss ANTIFLEX method to reduce internal reflections and thus to increase contrast. It utilizes the extinction of polarized light with a crossed polarizer analyzer pair to cancel out internal reflection. A  $1/4$  wavelength plate in front of the lens converts the linear polarized light into circular polarized. The reflected light is again converted into linear polarized light, but with a 90 degree shift. It does therefore pass the analyzer.

## **Fluorescence Microscopy**

Organic molecules that absorb light and reemit it at a longer wavelength generate fluorescence. Fluorescent dyes only absorb a minimum of light in comparison to conventional dyes. This makes them the dyes of choice for three-dimensional imaging of cells and tissues, because light can penetrate through the sample with a minimum of absorption. A fluorescent microscope has a set of filters that separate the excitation light from the emitted light. The filters are typically combined into a cube. Multiple cubes can be used to image a number of fluorescent dyes in the same sample.

Recent advances in confocal microscopy include spectrophotometric detection. The spectrophotometer can be programmed to any required wavelength for detection. This obviates the need for separate filters for each dye.

## **Multimodal Confocal Microscopy**

The confocal laser-scanning microscope scans samples with a diffraction limited laser beam. The confocal principle requires an excitation and a detection pinhole that are in the same back focal plane. The excitation pinhole creates a diffraction limited illumination spot. Light returning from the sample by reflection, or fluorescent light passes through the second pinhole that rejects out-of-focus light. Each pinhole corresponds to a narrowly focused spot in the sample. The three-dimensional distribution of light created by the pinhole is described by the point-spread function. The image acquired by the confocal microscope is a convolution of excitation and emission point spread function.

In practice, a scanning mirror moves the beam across the imaging field to acquire a two- or three-dimensional data set. Newer confocal microscopes contain a spectrophotometer to acquire information about the wavelength distribution of the emitted light. Spectral scanning can add an additional dimension to the data. Scanning can also be performed over time to observe changes in the sample.

The light passing through the sample can be collected as well. This data corresponds to the transmitted light image in a conventional microscope. Contrasting techniques such as phase or DIC can be added to the transmitted light channel.

Transmitted light contains limited depth information, because it is not confocal. Thus it is generally unsuitable for three-dimensional reconstructions.

Fluorescent lifetime is another dimension that can be utilized in confocal microscopy. A sub nano second laser pulse excites the fluorescent molecules. The systems measures the time until the fluorescent photons return to the detector. The lifetime gives information about the type of fluorescence and aids in physiological studies. The microscope used for this work did not have lifetime imaging capabilities.

Further dimensions can be added in the future. Fluorescent molecules have to be oriented along the polarization axis of excitation. They store the energy of an absorbed photon for a few nano-seconds before releasing it as fluorescence. The molecule can rotate during that time. If one excites the sample with polarized light depolarization will occur for the emitted light. Thus, the degree of depolarization is a measure for the rotational speed of

the molecule. This effect is called fluorescence anisotropy. However, none of the currently commercially available confocal systems measure anisotropy.

Multidimensional microscopy is a fast moving field. Wide availability of semiconductor lasers will soon enable new applications. Visualization software should be flexible enough to accommodate these future developments.

## **Software Technologies**

The choice of development technologies is crucial for a successful software project. It is essential for performance, maintainability and capability of the application. Other differentiating factors include availability and support of tools for visualization software development.

### **Object Oriented Programming**

A common problem in procedural languages such as C, Pascal and Fortran was increasing complexity and size of programs. A common engineering practice called structured programming solved this problem initially. However, with the introduction of graphical user interfaces and their enormous complexity structured programming was no longer sufficient. Procedural code became very complex and had a lot of cross dependencies commonly referred to as "spaghetti code". This led to a new approach called object-oriented programming (OOP).

OOP is a programming paradigm. The central idea is that computer programs can be seen as a collection of interoperating units called objects in comparison to the traditional view that saw programs as a collection of procedures. OOP is based on the following concepts:

1. **Classes** - A class is a unit that contains data and related methods. The methods usually apply only to the contained data and not to external data. This concept is called encapsulation. Encapsulation is the basis for modularity and structure of object-oriented programs.
2. **Object** - An object as a concrete instance of a class. While the class is the abstraction similar to a template, an object is an instance with concrete data. A concrete example would be an address object and class. The class would contain fields like street, city, name phone number, etc. but no concrete data. The object would be an instance of the class that would contain the name number and other data of a specific person. A class can have many objects as a result. The object is also in contrast to primitive types of data, such as float and integer.
3. **Inheritance** - Inheritance is a mechanism to specialize or sub-type an existing class. The subclass can add data, have special methods or other extensions that either add functionality or limit it. An example for an address database would be a home address. It is special, in that only some addresses are home addresses. It can contain additional information such as other family members that only apply to this special type of address. So it is a specialization and extension to the general address class.



4. Abstraction - Abstraction is the ability to interact with subclasses but treating them as super classes. In our address book example the class address book would not need to know the difference between a home address and a company address and could treat both of them as an object of the more general super class. Abstraction simplifies programming, as the code can be more generalized and be subclass agnostic. The address book class could print all addresses without making any distinction if it is a home or business address.
5. Messages - Messages provide a mechanism for objects to communicate with each other. It is part of the abstraction mechanism, because the message sending class does not need to know the type of class of the receiving class, as long as the receiving class understands the message.

The first object oriented programming language was Smalltalk developed by Alan Keys at Xerox (Xerox PARC, Mountain View, California). The Smalltalk language has been designed from ground up to support all features of object-oriented programming. Smalltalk was designed to be a dynamic system and was based on interpreter technology. This made it easy to adapt to new hardware and operating systems, but performance problems prevented wide spread adoption. Smalltalk is a pure object oriented language which only uses objects and classes and does not have primitive types. This makes it difficult to use lower level libraries such as OpenGL since these libraries only use primitive types.

### **Objective C Language**

Brad Cox originally developed objective-C at Stepstone in the early 1980's. At that time computers had evolved enough so that larger programs could be designed and executed. Objective-C combines the speed of the C-language with the object-oriented features of Smalltalk. It is possible to compile any C program with an Objective-C compiler. Objective C features semantics to build classes and objects. It has a mechanism for message passing among objects. It also supports dynamic typing which allows objects to send messages to other objects even if they do not understand them. Ignored messages can be passed on to other objects. This process is called message forwarding. Flexible messaging simplifies programs further as less type checking is required and object collaborations are more flexible.

Protocols are an additional language mechanism to reduce complexity. Protocols can define a group of related messages. Adoption of a protocol by a class means that this class responds to all messages defined. A protocol serves to make very diverse classes respond to the same messages without the need for subclassing.

We will show how these language features improve the development of our software applications.

### **Integrated Development Environment**

Apple Computer's Macintosh and International Business Machines (IBM) PC based systems are widely available computer platforms. Three popular operating systems run on these hardware platforms: Microsoft Windows and Linux on the PC based platform, and OS X on

the Macintosh. Each platform has its strengths and weaknesses, and we concentrate analysis on the support for development of graphical visualization applications.

Developer tools are available for all three platforms. They are free for Linux and Mac OS, but a commercial for fee license is required for Microsoft Visual Studio. Linux and OS X compiler technology is based on the open source GNU GCC toolset (Free Software Foundation, Boston, MA). Microsoft has a proprietary development tools. The biggest difference between the platforms is in the inclusion of additional tools for debugging and performance analysis. Microsoft Windows has very little in support for performance analysis. Memory debugging tools are only available as expensive third party applications. Linux offers very rudimentary tools only. Apple provides a host of performance analysis tools that work with kernel support and are very accurate. Apple's computer hardware understanding development (CHUD) tools include a performance library that can be compiled into the application to enable native automated performance analysis. This is an essential technology for the programming methodology discussed below.

## **OpenGL**

There are large differences in the support of three-dimensional rendering. The OpenGL rendering library forms the basis for most modern technical and scientific visualization applications. OpenGL is a cross-platform cross-language Application Programming Interface (API) that produces accelerated two- and three-dimensional computer graphics. It consists of over 250 function calls. More recently a shading language was added to make rendering more flexible. OpenGL is widely used in computer aided design (CAD), virtual reality (VR), scientific visualization and video game development.

Implementations of OpenGL are vendor supplied, but a standards group governs specifications. This guaranties compatibility across platforms and hardware implementations. Some popular implementations are for Microsoft Windows (Microsoft Inc., Seattle, Washington), Apple's Mac OS X (Apple Computer, Cupertino, California), Linux and other Unix systems.

OpenGL specifications are overseen by the Architecture Review Board (ARB) which was founded in 1992. OpenGL was initially developed by Silicon Graphics Inc. (SGI, Mountain View, California). This company specialized in creating both powerful graphics hardware and software. SGI developed the Iris Graphics Language (IrisGL) to ease software development and to abstract it from the underlying hardware. SGI used IrisGL as a basis for OpenGL created the initial standard set of routines. These were licensed to other companies. One remarkable feature of OpenGL is a defined set of operations independent of the kind of present hardware. If the hardware does not implement an operation, OpenGL falls back on software routines. This makes OpenGL software compatible with a wide range of hardware implementations. Performance may vary widely depending on the degree of hardware support.

A competing API is Microsoft's Direct3D. It has many of the features of OpenGL but is limited to Windows PCs, and it performs poorly if the hardware implementation is incomplete. This limits its usefulness for visualization and leads to severe restrictions for

hardware requirement, i.e. will only run on a narrow range of computers. Direct3D is currently limited to game development.

## **OS X Operating System**

Apple's OS X operating system is based on the Mach kernel (Carnegie Mellon University, Pittsburgh, PA) and FreeBSD Unix (University of California at Berkeley, Berkeley, CA). BSD has its roots in the original AT&T Unix developed by Bell Labs. The development environment is based on common tools such as GNU compiler. Low level software libraries adhere to all the common UNIX standards. OS X, however, has added many powerful capabilities not found on any other platform. We will briefly review the history of OS X.

OS X has its roots in NextStep, a very innovative operating system. Its development started in 1985, and the first version was released in September of 1989. It was deployed originally on NeXT Computer Inc. computer systems. The company was acquired in 1997 by Apple Computer Inc. NextStep had several revolutionary features:

- display of text and graphics through a postscript interpreter
- introduced the Objective-C language
- offered frameworks and tools for advanced software development

Postscript was originally developed by Chuck Geschke and John Warnock of Adobe (Adobe Systems, San Jose, California) as a device independent way for printing. Instead of sending data to the printer (such as text and bitmaps) Geschke and Warnock invented a way to send executable programs, which described what, should be printed. They called this technology Postscript. It made printing completely independent of the underlying hardware technology. Postscript is actually a programming language for page description and has since been documented and standardized. NeXT Inc. took a subset of the language and called it Display Postscript. Adobe later defined another subset for portable documents called Portable Document Format (PDF). After Apple Computer bought NeXT, it ported the NextStep technology on its PowerPC platform and renamed the operating system OS X. Display postscript was replaced with PDF as the document display technology. This technology enables high quality display of data and user interfaces.

The original NextSTEP introduced a number of user interface enhancements, which have since become commonplace. These included three-dimensional "chiseled" widgets, real-time display updates, window dragging, and property dialogs called inspectors. All of these features can now be found in Apple's OS X. Other important technologies such as the first web browser called "WorldWideWeb" were initially developed on NextStep by Tim Berners-Lee at CERN (Organization Européenne pour la Recherche Nucléaire, Geneva, Switzerland). Other important applications developed on this platform were the illustration application Macromedia Freehand (now part of Adobe Systems), the revolutionary symbolic math software Mathematica (Wolfram Research, Champaign, Illinois) and the game Doom (ID Software, Mesquite, Texas) that spawned a whole generation of immersive 3-D games.

This shows that the NextStep development environment is very powerful for development of novel graphical applications. It has since been renamed Cocoa and became part of OS X.

## **Computing Hardware**

A general review of computer hardware technology is important for the performance and flexibility of application design. A good software design uses the strength of a given hardware architecture and mitigates its weaknesses. It incorporates flexibility to account for variations between different system configurations. A more capable system enables processing of large data sets not feasible on a lesser architectures. Strategies such as data reduction and simplification need to account for these differences.

Another important factor is the diversity of systems. Systems vary greatly in capability regarding available memory and processing capabilities. This makes support and a unified user experience difficult. Some specialized features may exist on one system but are missing on another. A common solution to accommodate this diversity is to limit software features to the lowest common denominator. This in turn limits what the software can do.

An opposite approach is to increase minimum system requirements. Increased requirements limit the number of systems both on which the application will run, and the number of users. It is important to strike a careful balance between minimum requirements and software capabilities.

Scalable software features are a better approach to solve this problem. A scalable application is optimized for the best available hardware technologies and to gracefully reduce capabilities on lesser systems. We took this flexible approach for our project.

Two technologies have shaped the computing landscape for visualization. One is vector processing in general purpose central processing units (CPUs). The other is the development of highly capable and specialized graphics processors (GPUs). They accelerate common rendering tasks. Both technologies overlap and complement each other.

We present a short introduction and examination of the fundamentals and recent developments for both technologies. This will serve as the foundation for our visualization software implementation.

## **Vector Processing**

Vector processing relies on "Single Instruction Multiple Data" (SIMD) operations. As the name implies, a single instruction can process multiple pieces of data simultaneously on a single processing unit. This technology became first available on large-scale supercomputers. The first popular implementations were the SIMD instructions on Cray (Cray Inc., Seattle, Washington) supercomputers in the 1970s. Historically a number processor commonly referred to as Digital Signal Processors (DSP) implemented these instruction sets. Today all widely CPUs for personal computers contain both SIMD instruction sets and processing capabilities. SIMD instructions are commonly used in multimedia applications and games. These applications require large amounts of data

processing but also are ideal for parallel data processing. An example would be image processing where contrast and brightness need to be adjusted. Each pixel would be multiplied by the new contrast value, and the brightness offset added. This would require two instructions for each pixel on a scalar processor. However, a vector processor would be able to load multiple pixels simultaneously (typically 16), and depending on the instruction set performs the two operations in one cycle. Theoretically this would increase the processing speed 32 fold. However, main memory is often not fast enough to support parallel loading and saving of large chunks quickly. As a result, the speed of processing operations is no longer bound by processor speed but by the speed of memory. This is commonly referred to as memory bound processing, in contrast to CPU bound processing.

Apple's G4 and G5 system architecture has many significant advantages over older Intel CPUs. Adoption of SIMD was slower by Apple, but Intel's MultiMedia eXtensions (MMX) instructions were too limited for general use. Many SIMD designs were crippled by commercial considerations. One of the considerations of chip designers is the amount of space that vector units use, as each additional space increases chip production cost. SIMD requires special registers to hold the data. Intel's first implementation of SIMD called MMX used the general floating point registers for processing. As a result the contents of floating point registers had to be written out, and the vector data loaded before a vector instruction could be executed. This was a significant limitation and thus vector processing was often slower than regular scalar processing on Intel CPUs. The MMX instructions saw little use in general computing. Because of these limitations compilers did not support MMX instructions, and programmers had to resort to assembly language.

Apple Computer had more success because it took part in the joint development together with IBM and Motorola (the AIM alliance) for a SIMD instruction set called AltiVec. It was implemented on the PowerPC architecture. Keith Diefendorff, director of microprocessor architecture at Apple Computer, originally developed AltiVec between 1996 and 1998. It was the most powerful instruction set for PCs when it was introduced in the late 1990s. AltiVec offers a rich set of instructions and can be directly programmed in the C programming language. Apple itself included many of these instructions in their own libraries and applications such as iTunes and Quicktime and OpenGL.

However, Intel's recent development of its third and fourth generation SIMD instruction-set called SSE2 and SSE3 has matched, and even exceeded, AltiVec. These were initially available on the Pentium 4. SSE3 is implemented on the Intel Core Duo chip that was introduced to the market in January of 2006.

	<b>AltiVec</b>	<b>Intel SSE, SSE2 &amp; SSE3</b>
	32 separate Registers	8 XMM registers
	max throughput: 8 Flops / cycle	max throughput: 4 Flops / cycle
	32-bit saturated arithmetic	no 32-bit saturated arithmetic
	unsigned compare	no unsigned compares
	IEEE-754 (Java subset) compliant	Fully IEEE-754 compliant

**Table 2 Comparison of AltiVec and SSE vector instructions**

*Both AltiVec and SSE have 128 bit registers that can represent 16 8-bit or 4 32-bit floating point variables. PowerPC chips contain 32 128-bit vector registers in comparison to 8 for SSE2.*

AltiVec is compatible over several generations of G4 and G5 processors. This is in contrast to INTEL / AMD processors on Windows platforms where four different instruction sets (MMX, SSE, SSE2, SSE3) exist. This makes general support for vector instructions very difficult. Apple provides several libraries optimized for vector processing. These include an image processing framework, a signal processing library and many routines in standard libraries (e.g. for memory allocation and transfer).

Thus, the Apple PowerMac platform with OSX is a superior platform in terms of compatibility, capability, and developer support.

## **Graphics Processing**

A graphics-processing unit (GPU) is a chip dedicated to process visual data. It has specialized functions to efficiently accelerate common graphics operations. Earlier computer architectures draw display data directly into video memory, and a video modulator in turn displayed this information. Early two-dimensional graphics accelerators added circuitry for filling parts of the memory very rapidly. The blitter, as the circuit was called, could rapidly draw geometric figures such as circles, triangles and polygons. S3 Graphics introduced the first single chip accelerator in 1991. nVidia introduced the first circuit to support three-dimensional texturing and lighting (T&L) on a single chip in 1999. The first chip to support programmable shading of three-dimensional textures was the nVidia GeForce 3 which appeared in October of 2001. Before the GeForce 3 was introduced, all of these functions required specialized computer systems with multiple processors. All of these developments required fast memory subsystems. The data bandwidth requirement for a three-dimensional accelerated rendering is in the range of several gigabyte per second. Thus, today memory bandwidth is the limiting factor in graphics designs.

Operating systems contain special software libraries to make these hardware-accelerated functions available to programs. Direct X is the most widely used on Windows. Another library that exists for several platforms is OpenGL.

## ***Perceptual Rendering as a New Paradigm***

Volume visualization creates reconstructions that present complex data in a comprehensible ways. Current visualization methods use direct rendering or surface based rendering. Both are based on the laws of optics and reproduce real-world lighting effects in a virtual reality model. The rationale is that if the laws of physics are applied to the visualization model results yield scientifically valid renderings. As long as the underlying model theory is sound, it is guaranteed that rendering artifacts are reduced to a minimum and the final image valid. This paradigm is not sufficient for multi-modal rendering. Visualization for multi-modal microscopy poses two unique challenges:

1. Biological samples have optical properties that typically do not correspond to any objects we encounter in the real world
2. Multiple acquisition modalities such as transmitted light and confocal fluorescence can be combined during imaging

Biological samples have optical properties that typically do not correspond to any objects we encounter in the real world. Multiple acquisition modalities such as transmitted light and confocal fluorescence can be combined during imaging. A typical cell is nearly transparent and colorless, and cannot be seen in detail by the naked eye under the microscope. Internal structures become visible by fluorescence staining or optical contrasting methods such as phase contrast or DIC. However, it is unclear how a translation from raw imaging data into a virtual reality model such as a surface model can enhance our understanding. Data rendered with very sophisticated algorithms is often perceived as “cartoon like”, as reconstructed images bear little resemblance with our visual observation in the microscope. The goals for improvements are:

- Enhanced understanding and comprehension of complex data
- Improved realism and avoidance of artificial look
- Minimized rendering artifacts

The central question is whether adherence to the laws of optics and physics is required. Our experience shows that current models do not necessarily improve the realism and understanding of the final image. The task is even more complex if we combine images acquired with different modalities. For our visual system no physics based model can bridge the gap between different imaging modalities. Thus there is clearly a need for advanced visualization methods for both regular fluorescence microscopy and multi-modal microscopy. Recently published studies concentrate on quantitative analysis and screening, but not on improvements in visualization (31,32).

To solve this problem we need to rethink the visualization process itself. We need to look at the way we perceive visual information, i.e., how we are used to construct our visual world, and to match the rendering process to our perception accordingly. This is in effect a reversal of existing approaches. Rendering methods are developed by designing the visualization algorithms first and testing quality and correctness in a second step. This trial and error approach is quite costly because many models have to be developed and evaluated to get some improvement.

However, if we understand how we perceive images, we can identify the critical visual cues for volume reconstruction. We can design the necessary processing steps to synthesize the required perceptual clues in the rendering. Thus, we construct the imaging pipeline in reverse: instead of taking the data and translating it into a visual model, we look at human perception and ask, what kind of transforms can make us perceive the true shape and morphology of microscopic objects.

We will call this approach perceptual rendering. Perceptual rendering is a deliberate process to synthesize user adjustable visual clues in volume renderings.

### **Compositing Multimodal Images**

Visualization in light microscopy data poses additional challenges. Many structures are at, or even beyond, the limit of resolution. The resulting images often are an insufficient representation of the original structures. Segmentation methods can easily introduce need to be applied cautiously. In some cases, only a combination of images acquired with different modalities yield important scientific insight. A typical example is the combination of transmitted light images of cells overlaid with fluorescent internal structures. The transmitted light image provides a cellular map artifacts and thus, while the fluorescence marks the functional structure of interest. Each modality by itself provides incomplete data, and only the combined rendering reveals relevant data. However, even this simple example shows some inherent problems. How should both images be combined? Should the fluorescent image mask the underlying image, or should they be combined by color blending of both images? Both methods would give very different results. The methods are established, and valid visualization techniques exist. However, the answer to which method is the best can only be found in the context of the original scientific question.

How can we find correct visualizations for even more complex imaging modalities? How can we reconstruct e.g. a three-dimensional confocal stack containing lifetime and spectral information in addition to a DIC transmitted light image?

Again, advanced imaging methods record features that cannot be adequately perceived by the human visual system (15). Our eyes are incapable of detecting properties of light such as polarization or lifetime. Spectral and spatial resolution of our eyes is limited in comparison to modern instruments.



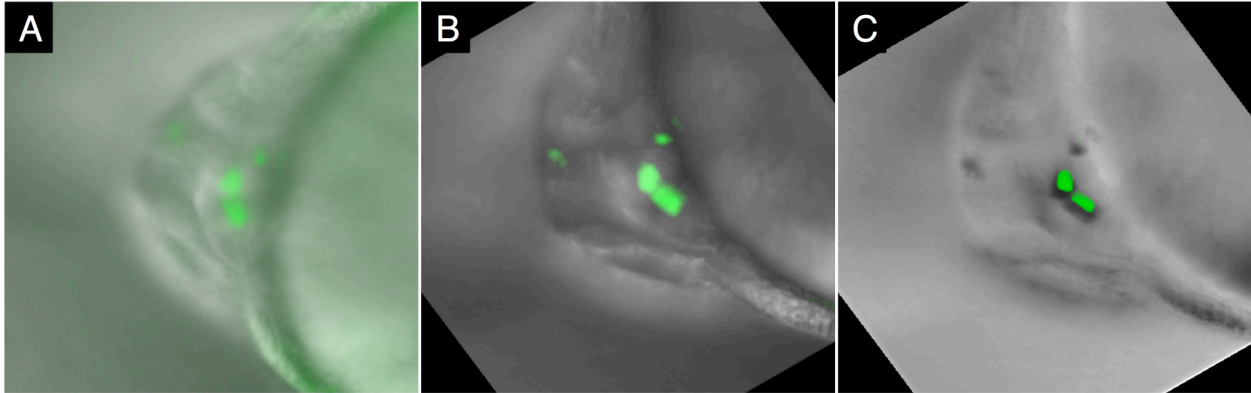


**Figure 2: Blending of transmitted light and confocal images**

*20 h old Zebrafish embryo with GFP expression in the pituitary. Images show a transmitted light stack in black and white blended with a confocal fluorescence stack in green. A) Channels blended with simple alpha blending. B) Channels blended with MIP. C) Alpha projection of confocal stack with shadow backdrop and flat projection of transmitted light channel*

The confocal stack contains three-dimensional information but it cannot be seen with simple volume rendering. Blending does not show clear spatial relationships.

### Synthesizing Depth Cues

Three-dimensional organization is important to understand the function of biological samples, and fluorescence microscopy is the main modality for microscopic observation. Normal fluorescent images, however, contain no depth cues. To demonstrate this phenomenon we simulated the fluorescence imaging process.

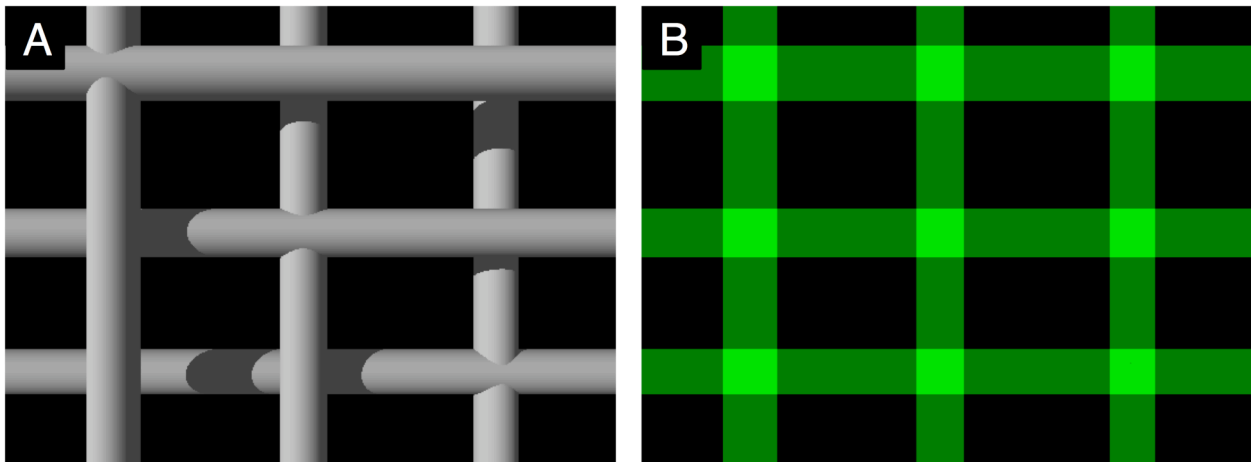


**Figure 3: Simulation of Fluorescence**

*A) A virtual reality model of intersecting tubes. Spatial arrangement is clearly visible. B) The same tubes rendered with optical properties as fluorescent objects. Fluorescence light emission and loss of shadows and opacity prevents depth perception.*

First we created a virtual reality model of intersecting gray tubes virtually illuminated with a directional light source. It was rendered in the Bryce (DAZ, Draper, Utah). The resulting

image lets us perceive both the shape of the tubes and their three-dimensional arrangement.

In a second step we assigned the same physical properties to the tubes that fluorescent objects have: They are transparent and emit light. Transparency prevents the formation of highlights and shadows. There is no occlusion, because the opacity is missing. We can neither perceive the shape nor the three-dimensional organization of the objects. The rendering appears flat. This illustrates the challenges in volume reconstruction of fluorescent objects.

The goal of perceptual rendering is to recreate visual clues so we can perceive spatial information again.

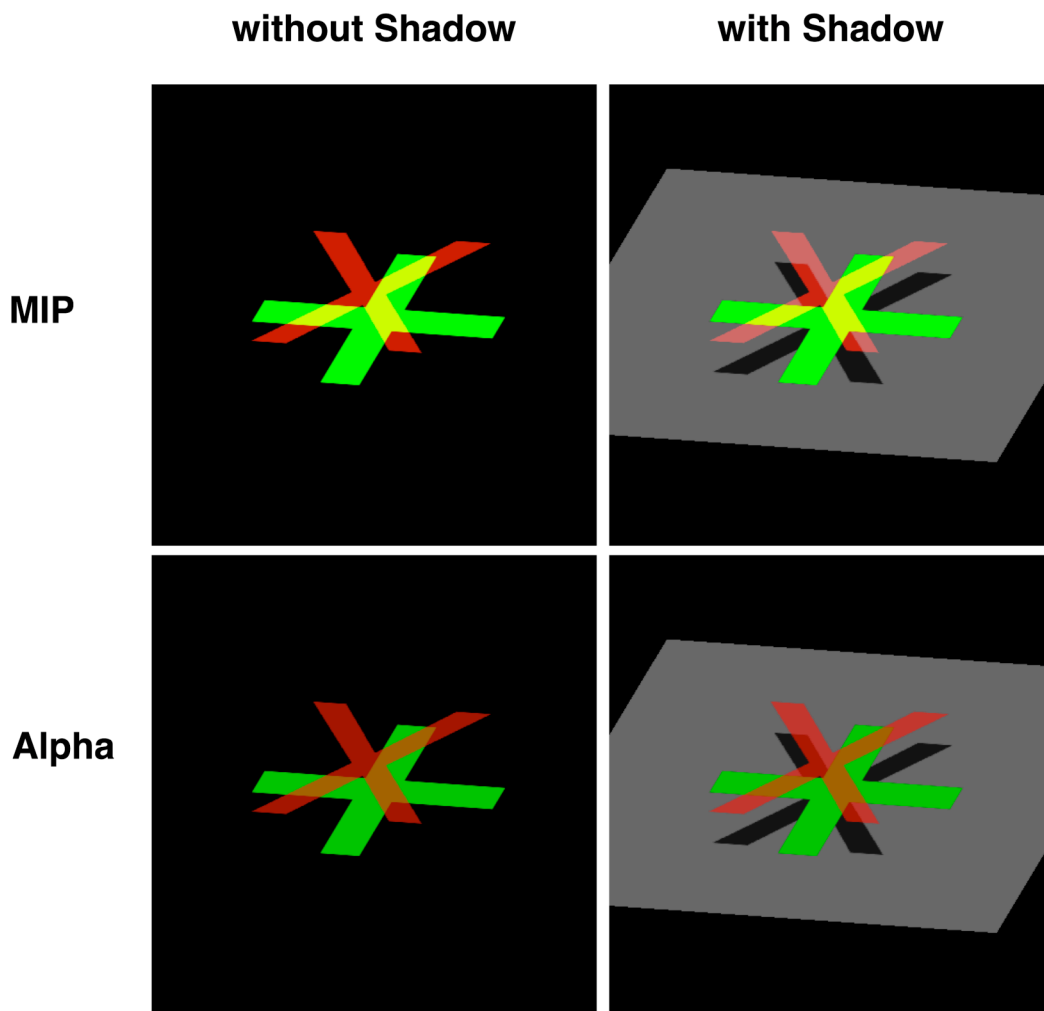


**Figure 4: Simulation of Perceptual Depth Cues**

*The figure shows two crosses with the same physical properties as fluorescent objects. The objects are rendered with and without drop shadow and in MIP and opacity projection mode. Only the combination of opacity and shadow generates a clear depth cue.*

## ***Application Architecture***

The visualization application poses several challenges for a good architecture. We have to consider:

- Rendering of complex multimodal data
- Flexibility and ease of use
- Acceleration by using all available hardware capabilities
- Complexity and maintenance of the application

Distributed processing can accelerate complex processing and visualization tasks. Multiple pieces of data are processed simultaneously and transferred to visualization processors. We implemented a multi step processing pipeline for fast data flow. Original data is held in the main memory of the computer. The Central Processing Unit (CPU) executes the first part of the processing pipeline and stores the results in a second memory location. A graphics processing unit (GPU) based video card takes the processed data and creates a two-dimensional rendering on the screen. Distributing the processing among different processors has several advantages. The first processing step reduces the complexity of data with a higher dimensionality to a maximum of three dimensions. Because multidimensional datasets can be quite large, processing can take a significant amount of time. Distributing the first processing step to several independent and parallel working units accelerates it significantly. General image processing methods that have been established in video processing can take advantage of this architecture.

Video processing offers a virtually unlimited number of methods to improve and manipulate image data. However, only a few of these methods make sense for biomedical applications. To obtain valid and meaningful data we use a logic framework with preselected operations that make sense for a given task and offer the user limited but meaningful choices.

A general problem is the limited amount of storage available. We need to take memory size limits into consideration for the pipeline design. The hard disk is the largest storage device available on modern computers. We can store petabytes of data on the disk by combining several disks into arrays as long as the file system supports large file systems. Disk space is rarely a limiting factor for visualization applications. Computer main memory is restricted to 4 GB for 32 bit systems. Depending on the memory management of the operating systems this amount may in practice be smaller. The amount of video memory on the graphics cards ranges from 8 to 512 megabytes (MB) and thus is the most limiting factor and. To accommodate limited amounts of main or video memory we sub-sample data. Sub-sampling occurs during the transfer either from disk to main memory, or from main memory to video memory.

Swapping and paging are techniques, which temporarily transfers data from a larger memory system to a more restricted one. The drawback of swapping is the latency it introduces. We can use swapping of data from disk to main memory if the data set is very large, but only a small amount is used for the visualization at any one time. A good example is a time series of data where only one three-dimensional hyper-slice out of a

four-dimensional data set is visualized at any one time. Speed of swapping data from main to video memory varies widely with the machine architecture. If the interface is very fast, main memory can replace video memory. Some computer architectures do not have video memory at all, but use a shared memory architecture. An example is Silicon Graphic's O2 Workstation and more recently Intel's GMA 950 architecture. Main memory has slower access times and lower bandwidth compared to video memory. The disadvantage of shared memory is that CPU and GPU share the limited bandwidth of the main memory. The shared memory architecture is found at low-end systems, because it is substantially cheaper to produce.

We optimize our software to reflect the hardware properties and minimize cross-dependencies. Data processing is broken up into three distinct parts:

1. Multidimensional storage and processing framework
2. Visualization framework
3. Application logic

This separation allows us to optimize the application separately for CPU, GPU, and memory architecture. Limited redundancy of processing operations allows us to assign the processing step to the most powerful unit. In extreme cases processing could be exclusive to either CPU or GPU. The CPU is idle if data does not require preprocessing. The GPU is not required if rendering is done in the OpenGL software renderer.

Because the data processing framework operates on multidimensional data and the visualization part only accepts three-dimensional data, operations that reduce dimensionality have to be performed in the processing framework. These operations are limited data reduction and orthogonal projection methods. The visualization framework offers non-orthogonal projections with specialized hardware support.

The task of the application logic is to coordinate and synchronize the processing and visualization steps. The processing framework is designed as flexible and versatile as possible. The user should only be presented with options that are pertinent to the data and visualization tasks. Hiding unnecessary parameters and options makes the program friendly and easy to operate. To achieve this goal we create a separate logic layer independent of the processing layer. The logic layer makes assumptions regarding the context of the data. It synchronizes the processing operations over space, time, spectrum, lifetime, or any other dimension. It limits operations to steps that make sense for a given rendering intent.

The general overview of the application is shown as a class collaboration diagram (Figure 5).

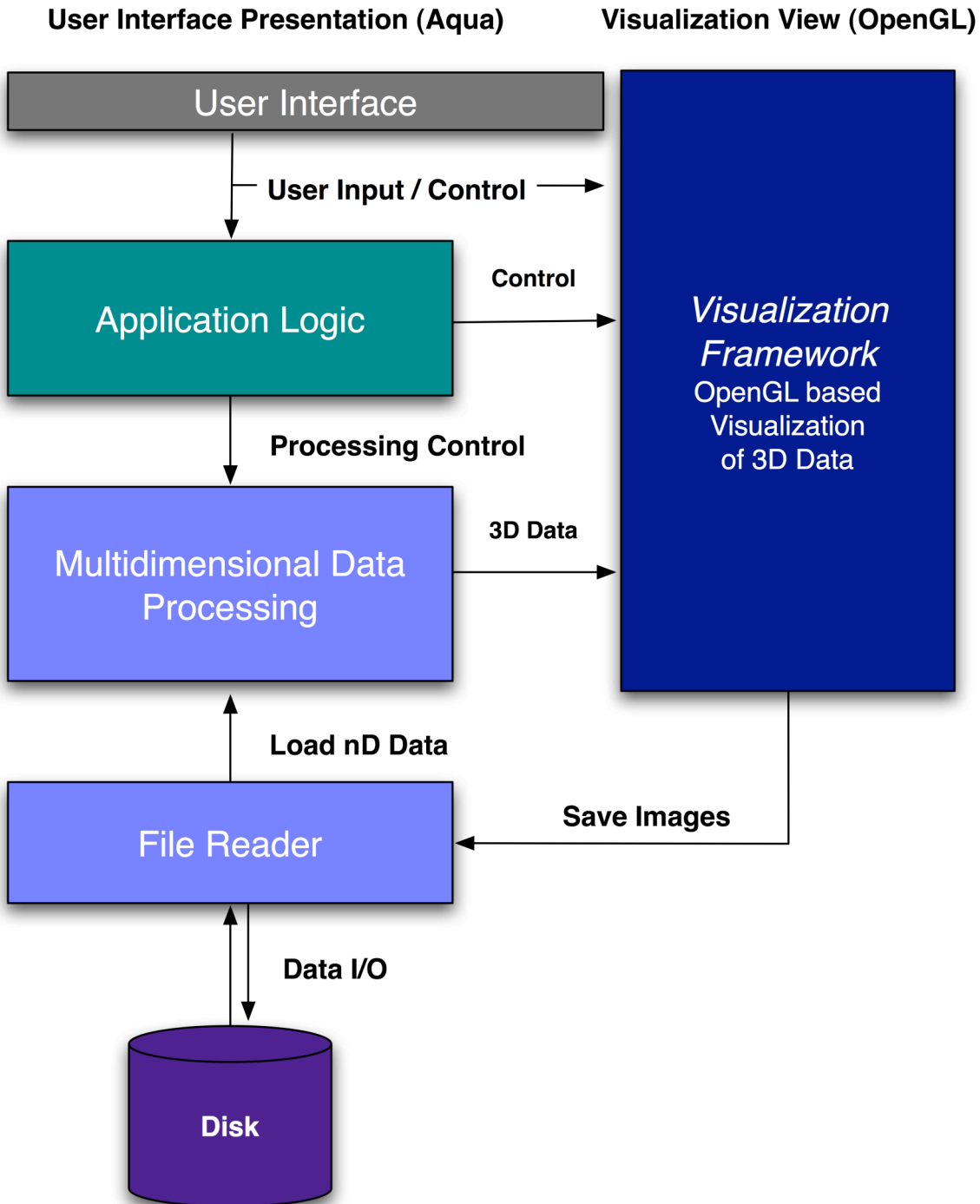


**Figure 5: Basic application architecture**

The diagram shows subsystems and the data flow between them. The multidimensional data is loaded by the file reader into the multidimensional data processing subsystem. A three-dimensional slice is transferred to the visualization part. Data processing and visualization subsystems are controlled by the application logic

## Multidimensional Storage and Processing

The multidimensional storage and processing framework is the hub for all data transfer and data preprocessing ahead of the visualization part. It represents the central processing through which all data must pass. Processing varies in complexity significantly. It ranges from a simple pass-through operation, where data is loaded from the disk and passed on without modification of the visualization framework to very complex processing pipelines with branches. All data handed off to the visualization framework has to be two- or three-dimensional. Thus, the underlying hardware and software limit the visualization framework to two- or three-dimensions.

To achieve acceptable performance for multidimensional processing we took advantage of vector processing. To make use of vector processing we needed to take several considerations into account. First the vector processing hardware implementation has to be efficient enough to yield a significant speed increase. Secondly the instruction set has to be simple and efficient. Complex instructions would require too much time and effort to implement the framework. Thirdly, we want to take advantage of preexisting libraries and routines in the operating system and libraries.

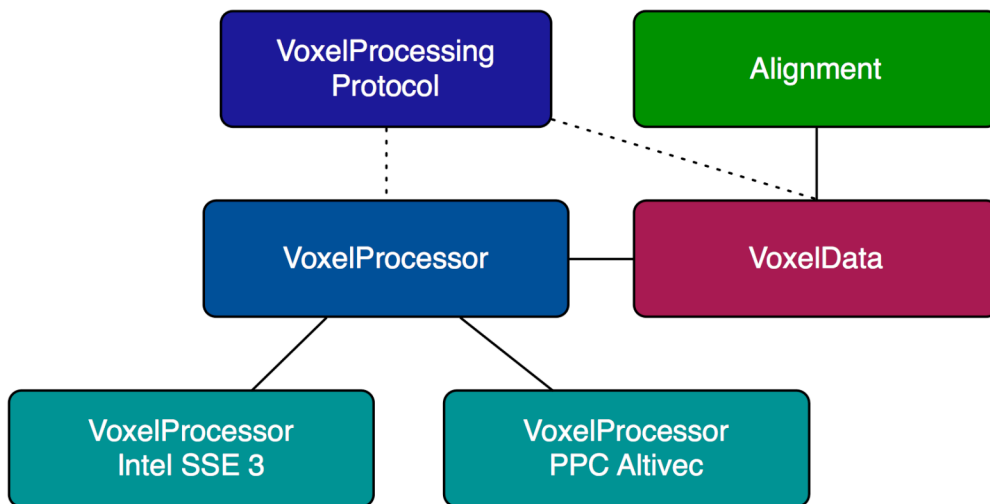


**Figure 6: Processing Architecture**

*The diagram shows collaboration between classes and protocols. The VoxelData class serves as data source and sink. The VoxelProcessor class implements the VoxelProcessing protocol. Specialized classes implement accelerated routines for Intel and AltiVec instructions*

Vector processing instructions are only effective if the source data adheres to three stringent rules:

- The data must be in continuous chunks
- The data chunks must be aligned to certain boundaries in memory
- Two dimensional data is padded so that all elements are aligned

This means that original data loaded from the drive needs to be properly aligned and padded when loaded into main memory. Data for the visualization part cannot be padded, as the padding would become part of the volume rendering. As a result routines that align

data, add and remove padding, and copy data efficiently are essential for good performance.

Different processor architectures use different vector instruction sets and some do not have vector instructions at all. The software has to fall back to scalar instructions if the vector unit is not present. To avoid large decision trees in the application we implemented an inheritance hierarchy that hides the complexity from the applicator. All processing operations are defined in an Objective-C protocol. The `VoxelProcessor` class implements this protocol. The class implements all methods in scalar code. Two subclasses implement specific accelerated routines. The protocol only needs to be implemented partially, because the super class already implements the fallback scalar methods. The basic architecture is shown (Figure 6). The voxel data can be realigned with the aligner class, which is capable to realign the data for any processing or visualization unit.

We decided to limit all multi-dimensional operations to orthogonal processing, meaning the processing operations can only work along the dimensional axes. This excludes processing at angles, or on rotated data. This limitation has little practical consequences, as the visualization framework implements all rotations anyway. This guaranties that data can always be processed as continues chunks. Some intermediate buffering may be required for higher dimensional operations, but the essential improvements of SIMD processing are available.

Separation of volume visualization, which is inherently limited to three dimensions but can freely rotate data from the storage and processing framework, which has dimensional limitations, is crucial for these reasons. This has little limitations for real world applications; only space needs to be represented by a three dimensional vector ( $x, y, z$ ). A one-dimensional vector can represent time, spectrum, and all other dimensions. So limiting processing to non-rotated data is not a real limitation, e.g. it does not make sense to create random slices when one dimension is time, the next spectrum, and the third is space. The resulting data would not be interpretable. If the dimensions are all spatial, we can apply rotations in the visualization framework.

The limitation of orthogonal processing keeps the framework design flexible and separate from the rendering pipeline that is responsible for rotations and other transforms. In essence the task of the multidimensional framework is to reformat and process data and feed it to the three-dimensional real time processing framework.

## **Visualization Framework**

The task of the visualization framework is to render data as a two-dimensional image on the screen or other output devices. It takes the data from the processing framework and composites and renders it onto the output device. We have to decide which hard and software platform is the best as a basis for visualization software development.

We used the OpenGL to implement the visualization framework. OpenGL is the key library that binds the graphics hardware to application software. Microsoft Windows' implementation of OpenGL remains at the 1.1 version level and is frozen at the state of 1995. Microsoft concentrates on the development of the competing proprietary Direct 3D. Graphic hardware developers have extended Windows OpenGL by including updated

dynamic link libraries. But basic support by Microsoft is frozen at the 1.1 level. Compatibility and interoperability problems are unavoidable for the wide variety of drivers and software implementations. That is the reason that many currently available applications will only run correctly on a handful of selected graphics hardware.

On the other hand, Linux has very fragmented OpenGL graphics support. The software library Mesa has support for the latest OpenGL features but does not support graphics hardware. This means OpenGL applications cannot take advantage of the parallel processing capabilities of modern GPUs. Other implementations are vendor specific and require graphics hardware from that specific vendor to function. The fragmented nature and spotty hardware support make Linux a less than ideal platform.

Apple's OS X comes with the latest OpenGL implementation (as of now version 2.0) and supports all available graphics hardware. The software implementation efficiently supplements less capable hardware. The software implementation correctly implements rendering functions for the OpenGL 2.0 specification. The tools for graphics development include a comprehensive OpenGL debugger and profiler. These tools are essential for debugging and performance optimization. However, they are not available for the other platforms.

OS X is the only operating system where OpenGL accelerates the two-dimensional user interface. Because Apple uses OpenGL widely, bugs surface much earlier. This makes the implementation very stable.

OpenGL offers functions for three-dimensional transforms, voxel and geometry based data as well as compositing operations. All modern graphics cards include capable GPUs. Modern GPUs significantly improve processing and rendering performance by accelerating matrix operations and parallel pixel and voxel processing. Separation of these processing capabilities and performance enhancements from the general multi-dimensional processing is important for real-time performance. It also makes maintenance of source code easier. The limiting factor of OpenGL processing is the often small amount of memory on the graphics card. To be able to take advantage of fast processing capabilities, the data needs to completely reside in video memory. This limits the maximum size of the three-dimensional data set. Two solutions for this problem are down sampling, and partial processing. Down sampling reduces the number of pixels by replacing the original data set with a lower resolution copy. The amount of down sampling depends on the amount of available memory on the graphics card. Another strategy is to process data in smaller chunks such as two-dimensional planes. Each plane is loaded into the video memory, processed and added to the final rendering. Because the data is only accessed and loaded once into video memory, rendering is still reasonably fast and even real-time for smaller data sets.

## **Application Logic**

The logic framework implements what is commonly referred to as application domain. It captures the knowledge and experience of visualization research as well as user preferences. Interpretation of end results still resides with the user, but processing operations that do not make sense in a given context are disallowed. To implement this



framework, we have to walk a fine line. On one hand we do not want to restrict choices, otherwise we prevent innovative uses of the visualization application. On the other hand we do not want the user to encounter a bewildering array of options and parameters where only a few select combinations make sense.

By separating logic from processing we decrease complexity and interdependency of processing framework significantly. We only develop one universal set of processing operations regardless of context. Future collaborative enhancement of the application by a group of diverse specialists is simplified, because it only requires local changes in logic and processing. Specialists in signal processing can implement new ways of multidimensional data processing without having anything to know about the biological applications. Graphics developers can implement hardware shaders in the GPU without having to have an understanding of the biological application or the origin of the multidimensional data. And each specialist can work in parallel with others, because there are very few dependencies.

### **Processing Pipeline**

These studies will show the feasibility of this project in two areas:

1. We undertake a performance analysis for the use of SIMD processing. The goal is to determine if parallel processing can significantly accelerate common operations. We use the Motorola Power PC AltiVec instructions for the analysis.
2. We develop a fully functional volumetric viewer based on three-dimensional texture processing under OpenGL. The viewer demonstrates the feasibility of fast volumetric rendering on mainstream hardware.

### **Acceleration by Motorola AltiVec Vector Unit**

Our preliminary results support the hypothesis that significant computational gains can be realized on PC architectures by using vector units. The register is 128 bits wide and can process 16 bytes in parallel. However, data has to follow strict rules. It has to be aligned at a 16-byte boundary and has to have a size of a multiple of 16 bytes. Correct data alignment in memory is required. Consequently, it is necessary to pad each line in an image to a multiple of 16 bytes in size. This results in extra overhead in processing and additional memory requirements. Therefore, performance gains would have to be substantial to justify the overhead.

### **Acceleration of Copy Operation**

The vector unit of the CPU provides essential support for fast image processing. We estimate how much acceleration we can achieve in comparison to scalar code. The most basic processing operation is to copy data from one memory location to another. The data is not modified in any way, so parallel execution does not offer any advantages. It is a worst-case scenario for SIMD instructions, in that operations are truly memory bound and not compute bound.

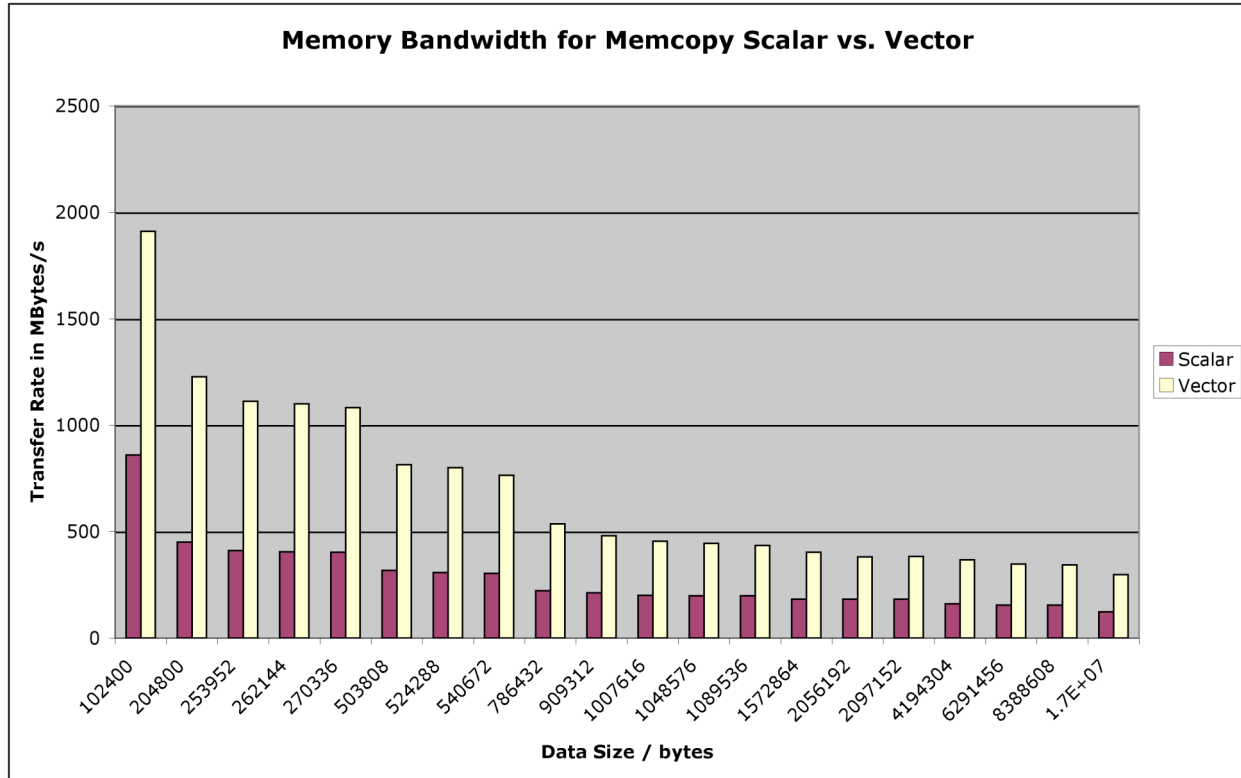


**Figure 7: Acceleration of Memory Copy with AltiVec vector instructions**

Beige colored bars represent vector copy operations. Purple bars represent normal scalar copy operations. Acceleration of copy operations is independent of the data size. Longer bars indicate better performance.

Surprisingly, we see a more than two-fold acceleration when vector registers are used. The performance was measured on a 1GHz G4 Apple Powerbook with 133 MHz memory (see figure 7). Block size of the data influences the result very little. The CPU of the test system has a significantly higher clock rate than the memory. The advantage of vector registers increases when memory becomes faster relative to the CPU. Memory bandwidth is 6 times higher on more recent PowerPC systems, while the processor clock-speed only doubled. The performance gain of SIMD over scalar instructions would be much higher in such a system.

### Acceleration of Color Interleaving

The next example is the application of vector processing to a simple image processing operation. A common processing operation is the merging of planar intensity data into interleaved RGBA values. A typical application example is the merging of the red, green, and blue channel of a fluorescent confocal dataset. The alpha (transparency) value is calculated in this example as by either OR-ing the RGB values, or calculating the maximum of the RGB values. Acceleration in processing was benchmarked by using the G4 AltiVec unit on an Apple 500MHz G4 PowerMac and Apples profiling tools.

The scalar code was written so that alpha value is calculated by OR-ing the bits of red green and blue. This was done to avoid the overhead of two function calls in each loop for

this benchmark. The vector code calculates the more desirable maximum value for each RGB value. Please note that the vector loop is longer because it processes 16 RGBA values simultaneously. The test results of running both loops to process a 22.5 MByte dataset were 0.8s for the scalar loop and 0.157s for the vector loop (table 3). The increase in processing efficiency was about five fold. The example does not include additional gains that might be achieved by optimizing the G4 caches.

```
for (i=0; i<size; i++) {
  rgbabuffer[i].red = pred[i];
  rgbabuffer[i].green = pgreen[i];
  rgbabuffer[i].blue = pblue[i];
  rgbabuffer[i].alpha = (pred[i]|pgreen[i]|pblue[i]);
}
```

**Figure 8: Scalar code merges planar RGB data into interleaved RGBA**

```
for (i=0; i<size; i++) {
  alpha = vec_max(*pred,*pgreen);
  redbluebuffer = vec_mergeh(*pred,*pblue);
  redalphabuffer = vec_mergeh(*pgreen,alpha);
  *rgbabuffer = vec_mergeh(redbluebuffer,redalphabuffer);
  rgbabuffer++;
  *rgbabuffer = vec_mergel(redbluebuffer,redalphabuffer);
  rgbabuffer++;
  redbluebuffer = vec_mergel(*pred,*pblue);
  redalphabuffer = vec_mergel(*pgreen,alpha);
  *rgbabuffer = vec_mergeh(redbluebuffer,redalphabuffer);
  rgbabuffer++;
  *rgbabuffer = vec_mergel(redbluebuffer,redalphabuffer);
  rgbabuffer++;
  pred++;pgreen++;pblue++;
}
```

**Figure 9: Vector code merges planar RGB data into interleaved RGBA**

	<i>Scalar code</i>	<i>Vector code</i>	<i>Acceleration</i>
<b>Program Runtime</b>	0.80 s	0.157 s	5 fold

**Table 3: Results of Vector Acceleration**

### Benchmark Results for SIMD Processing

The use of vector registers can greatly improve processing performance in even the simplest operations. Parallel processing of data is limited by the speed of main memory (i.e., memory bound), and not by the speed of the processor (processor bound). So for very simple processing like copying data from one memory location to another one could assume that parallel processing does not have advantages over scalar instructions. Our experiment, however, clearly shows that that is not the case. Even the most basic operations are already twice as fast. The more complex processing operations become, the

higher performance gain will be realized. This makes SIMD a valuable technology for multidimensional data processing.

### A Basic Volume Renderer

A basic volume renderer using OpenGL was developed to assess the feasibility on a PowerPC platform. The prototype implemented a complete OpenGL pipeline with three-dimensional textures in 8-bit alpha or 8-bit RGBA format, alpha attenuation and thresholding. User interactions such as translation and rotation of the volume sample were achieved in real time with a data set 10 MB in size on an Apple 500 MHz G4 PowerPC with an ATI Radeon graphics card with 32 MB of video memory.

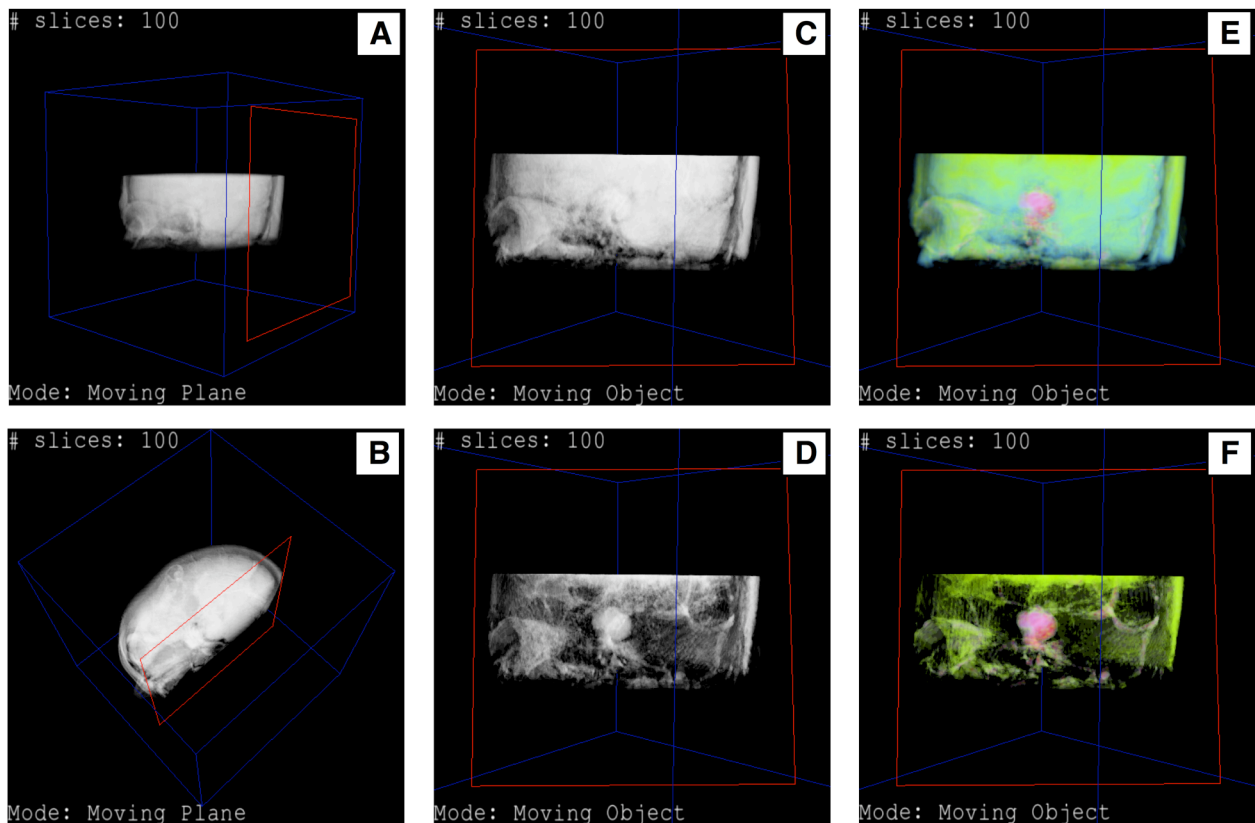


**Figure 10: Medical Volume Renderer**

*All images show alpha rendered MRI data of a human skull, with blue bounding box and red clip plane. A) rotated dataset without clipping B) rotated with clipping C) clip plane oriented to reveal pituitary D) thresholded to increase transparency E) & F) like C & D but with color table*

This hardware was state-of-the-art for PC workstations around 2001. The prototype demonstrates that real-time volume rendering is possible on older and basic computing platforms. It shows that this project does not require expensive computing hardware. It can be employed on a wide variety of existing and future platforms. More memory and faster processors will support bigger and even more complex data sets.

The graphics-processing unit (GPU) was programmed to calculate the alpha rendering (Figure 10). The bounding box is displayed in blue and the cutting plane in red. The user can freely rotate the volume data. A clipping plane removes tissue obscuring inside detail. The plane is moved along one axis. In this example the clipping plane is positioned near the median of the skull to reveal a pituitary tumor. To improve visibility and emphasize internal detail, pseudo-coloring can be applied to make the pituitary tumor stand out. Decreasing the general opacity and setting a threshold removes background data and enhances the visibility of the tumor in the monochrome rendering. Improvements in visibility between the original monochrome rendering and the pseudo-colored image are easily visible.

The MRI data was obtained from ATI Technologies Inc. (Markham, Ontario, Canada) and consisted of a single raw data file of fixed dimension. The three-dimensional data cube with 12 bit precision was converted into a three-dimensional 8 bit texture and loaded into OpenGL texture memory of an ATI Radeon graphics card.

### **Volume Transforms**

The prototype volume renderer allows complete rotation of the object in three axes. A zoom function lets users scale the image to any value. The rendering engine has tri-linear interpolation. Pixelation at higher zoom values depends on the hardware implementation of the tri-linear filter. The most commonly used box filter produces small cross-like artifacts at high magnifications.

A translation function offers panning, as the rendering might fill the viewer completely at higher zoom values. Unlimited zooming is supported. The renderer implements the general volume rendering algorithms. It is opacity based. Opacity can be attenuated by pre-multiplying alpha values with a constant between zero and one, with zero being completely transparent and one retaining the original transparency. So the user can set the multiplier and make the volume more or less transparent. A threshold can be set such that values below that threshold become completely transparent and hence invisible. Thresholding removes noise and background signal and makes the sample more transparent. Both opacity and threshold manipulations enhance parts of the volume, remove unwanted structures from the rendering, and highlight objects of interest.

### **Intensity Transfer Function**

A color look-up table function transforms black-and-white intensities into a pseudo-colored RGB image. The coloring highlights objects of interest and improves perception of dynamic range. A clipping plane enables slices through the volume data to reveal internal structures, which might otherwise be obscured. The user can position the plane in arbitrary positions and angles within the volume.

### **Realtime Volume Compositing**

This section shows the application of multi-dimensional processing and compositing. It enhances biological detail, improves display and print quality, and increases perception of spatial depth. The method relies on the combination of two-dimensional convolutions in the processing framework and OpenGL alpha compositing operations. The problem of

visualizing many biological samples is the huge dynamic range of biological samples. Relevant detail is often in the dimmest parts of the data set. One task is to bridge the dynamic range of the sample. The processing framework offers many ways to enhance renderings and solve this problem. Examples include intensity equalization, contrast stretching, and filtering. We picked a novel approach as an example of the power and flexibility of the application. The method relies on a combination of an absorption and emission model for the voxel data.

This strategy solves the problem of high dynamic range and retention of detail by creating partial intensity inversion and dynamic spread. The method composites four elements: the original image data, a black and white luminance image series (derived from the original data) as alpha map, an orthogonal shadow map, and a white background.

The result is superior to any of the regular single method renderings. Fine structures appear visible as small dark lines against the white background. Bright structures are partially muted but still clearly visible. These two effects limit the dynamic range and create a rendering that has high detail in shadows and highlights. The processing steps for creating this image are calculated in parallel and composited with intensity-encoded alpha. This results in an efficient parallel processing pipeline. Luminance is calculated from original planar RGB data in several programmable ways by using the CPU vector unit. The unit loads the planar data and converts it into an interleaved format. This additional calculation can be added without requiring any additional processor time, because the operation is memory and not compute bound. So the additional processing steps of encoding the luminance as alpha require additional processing time, but the time to load and store the data is much larger. By parallelizing load and store operations and processing steps we get processing without any time overhead.

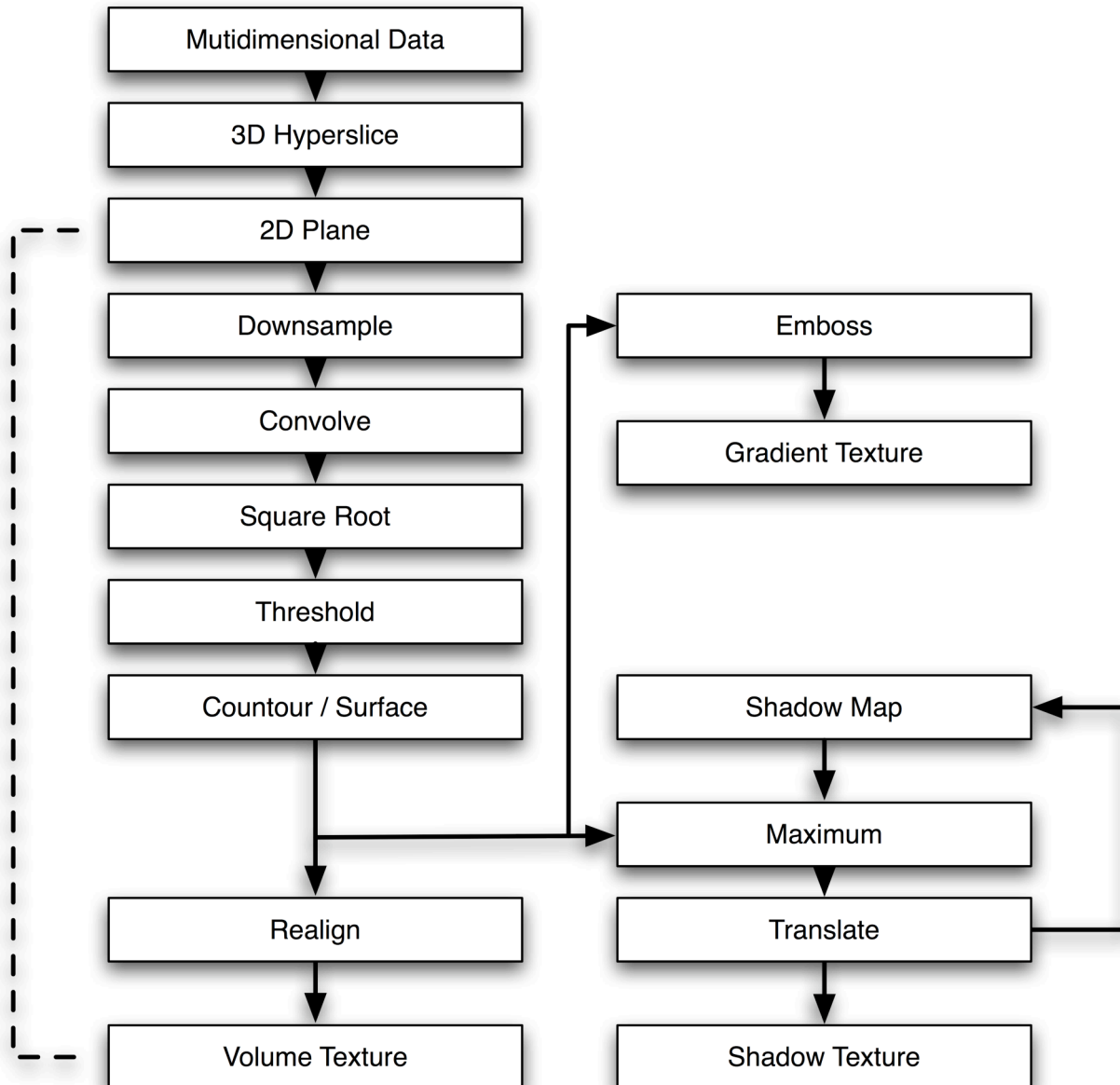


**Figure 11: Processing pipeline**

All renderings start with the multidimensional data. The first step extracts a three-dimensional hyperslice. The three-dimensional data is processed by breaking the data into two-dimensional slices (planes). The following process steps generate three textures: volume texture, shadow texture, add gradient texture. These textures are passed on to the OpenGL renderer.

The processed volume data is written out in RGBA data format to main memory and then directly transferred over the Advanced Graphics Port (AGP) via direct memory access (DMA) to video memory without additional copy operations. Many OpenGL implementations require that texture data is copied into an intermediate main memory buffer. An Apple specific extension allows the program to avoid this overhead and take the responsibility to manage texture buffer. DMA enables the OpenGL pipeline to use the GPU as processor parallel to the main CPU. Client texture management creates the alpha rendering visualizations without additional main system resources or CPU cycles.

## ***Visualization of Cytoskeletons***

We applied the described system to analyze the three major cytoskeletons in the cell. Actin is the smallest fiber with a diameter of 5 nm, intermediate filaments are 10 nm and microtubules are hollow rods with 25 nm diameter.

All of these fibers are beyond the resolution of conventional light and confocal microscopes and can be imaged only by immunofluorescence technique. The fibers can be of considerable length, and they are often bundled in the cell. Longer fibers and fiber bundles can be observed in the microscope, although visualization of these structures is very challenging. Fibers form thick bundles in part of the cell while staying independent in other parts. This leads to a huge dynamic range, as bundles are orders of magnitude brighter than single fibers. The range thus is at the limit of the available dynamic range of imaging equipment. Careful setting of black level and gain on camera systems or adjustments of offset and voltage on confocal systems are essential. But note that the 12 bit resolution of the original imager covering the dynamic range is reduced to 8 bit on the computer screen, and that the human eye is at best capable of detecting fewer than 50 gray levels which is equivalent to a dynamic range of 6 bits.

However, changes in the single fiber organization are valuable indicators of pharmacological effects, as they occur earlier and at lower dose than in bundles. Single fibers are more dynamic and have higher turnover than thicker bundles. These subtle changes are hardly visible on conventional image processing and visualization systems due to the overwhelming dynamic range required for that task.



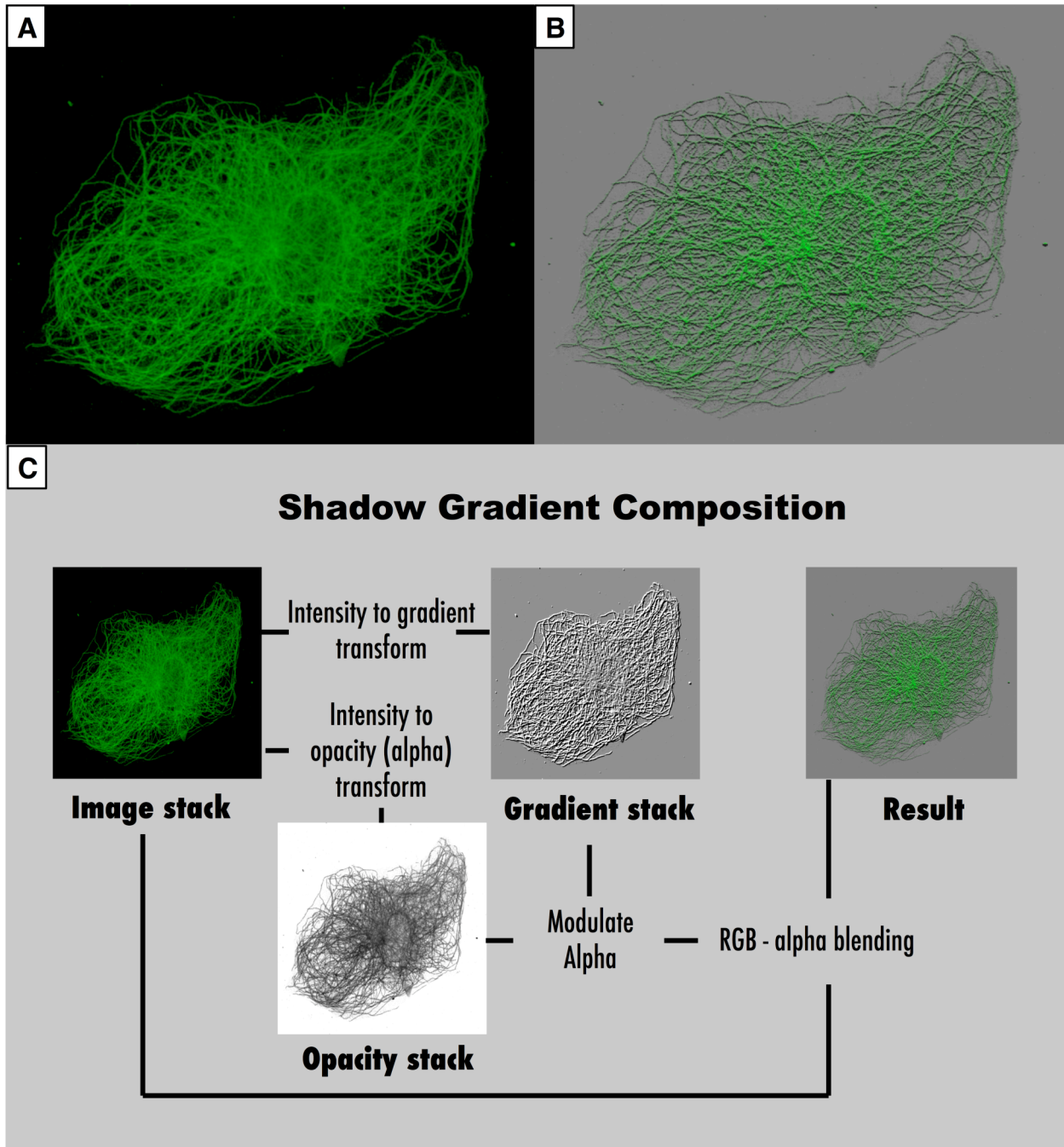


**Figure 12: Shadow generation**

A) Microtubules of a fibroblast in MIP. The fibers are resolved, but spatial information is missing. B) a gray backdrop with a cast shadow gives the fibers spatial appearance. C) The image stack is converted into an opacity and gradient stack. Both are composited against a gray backdrop. The gradient stack creates the appearance of a cast shadow.

### Improved Detail

This preliminary study shows improvements of rendering actin, microtubule and vimentin cytoskeletons in fibroblasts. Original confocal data was recorded on a Leica TCS/SP confocal scanner. Microtubules were stained with FITC conjugated mouse monoclonal

anti-tubulin antibody, actin with rhodamin labeled phalloidin, and vimentin filaments with goat-anti-vimentin primary and Cy5 conjugated rabbit-anti-goat secondary antibody. Confocal data was recorded sequentially for each dye. Both projections display microtubules as green, actin as red and vimentin as blue.

The maximum intensity projection clearly shows the organization of the major fiber bundles. Cell borders as well as smaller fibers and fiber bundles are difficult to see against the dark background, as they are comparatively dim. Linear contrast and brightness manipulation cannot help, as increases in brightness increase noise and limit dynamic range further. Gamma correction can help but increases the background noise substantially, thereby obscuring the very detail that was to be enhanced in the first place.

This is where innovative compositing leads to greatly improved rendering. The method requires two steps. First, a fourth image stack is calculated that holds transparency (alpha) data for each pixel. This alpha value is calculated by taking the maximum of each pixel value of the three separate stacks. Secondly, the RGBA stack is rendered against a white rectangle behind the image volume serving as a bright backdrop (Figure 13). Opacity rendering against a white background partially inverts the intensities, thus making fluorescent structures darker than their surroundings. As a result, fine actin fibers are much clearer and cell boundaries are clearly delineated against the background, and the image reproduces much better on a wide variety of printers and screens.

Three steps were taken to improve the rendering. First, an alpha map was created which was an exact copy of the original intensity values. Secondly, a differential image was created for each slice in the three-dimensional stack. In a third step, alpha values were modulated with values from differential images. This made one side of a structure slightly more transparent and the opposite side slightly less transparent. In effect, we create a shadow map encoded in the alpha channel. This shadow map is only effective when the background was not zero (meaning not black), as otherwise the shadow effect would be invisible. The result of image processing is obtained by rendering the RGBA stack against a medium gray background (Figure 13). The flat shape of the cell is immediately evident as are the single fibers at the periphery. The rendering has improved depth perception, level of detail and reproducibility.

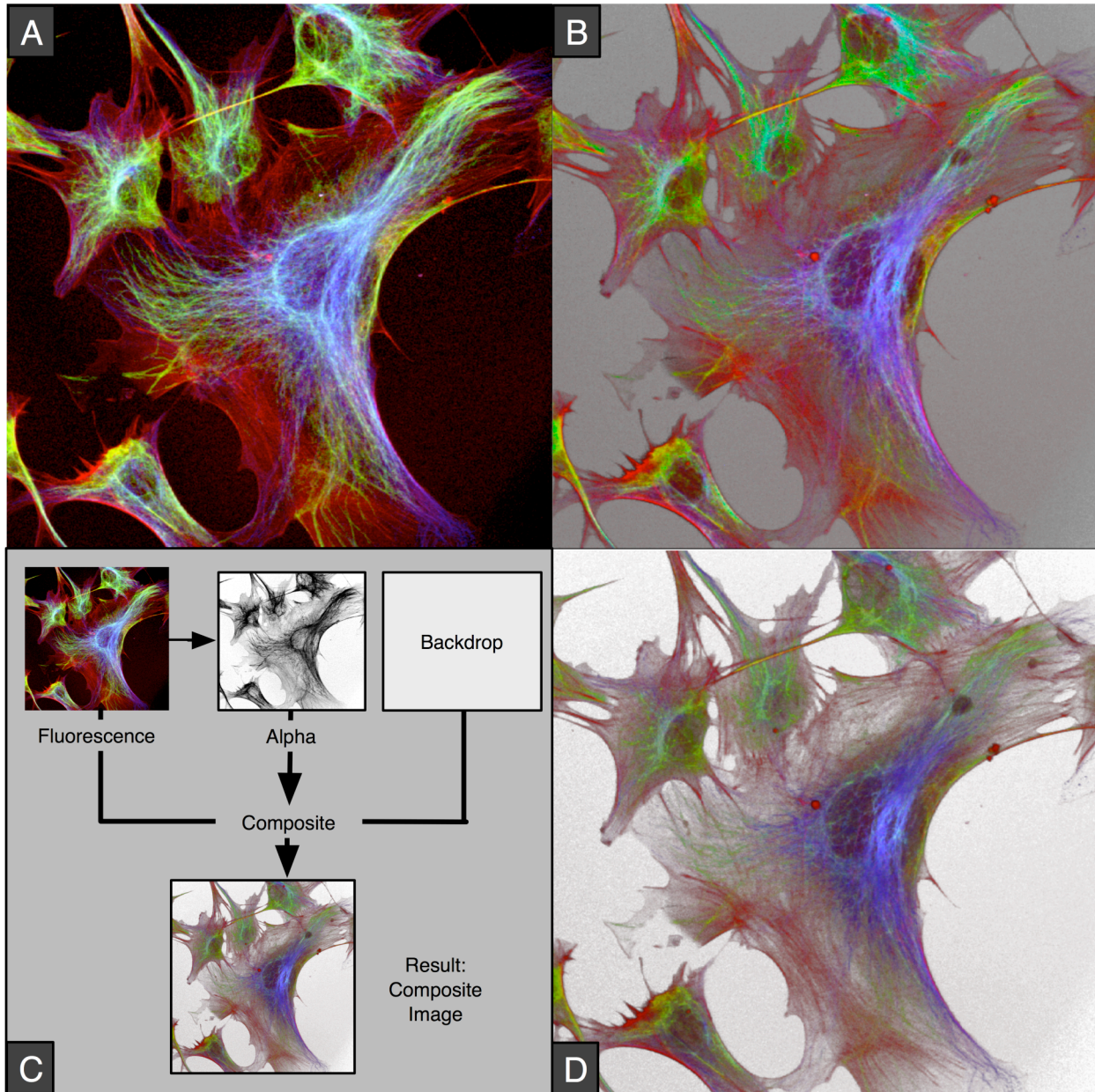


**Figure 13: Intensity inversion**

*Cytoskeletons in fibroblasts: actin (red) tubulin (green) and vimentin (blue) A) MIP of the three cytoskeletons. B & D) Alpha rendering of the cytoskeletons against a gray and white backdrop. The transparency (alpha) value leads to absorption. Fibers appear dark against a light backdrop. C) Diagram of the compositing operation of fluorescence opacity and backdrop. Data set courtesy of Leica Microsystems.*

### Shadow Maps and Modulated Alpha

The first example shows the effects of improved level of detail by applying a single calculated alpha to a three-color image. The second example demonstrates the improvements obtained by compositing a gradient shadow onto a single color rendering. This example shows the benefits of a combination of both methods.

The sample was a fibroblast with fluorescently labeled ER and actin fibers. The projection

of unprocessed data shows actin fibers in green and endoplasmic reticulum (ER) in red (Figure 14). But spatial organization is obscured. It is unclear if the actin fibers surround the ER or the ER “rests” on the fiber network. Furthermore, cell boundaries are not clear, and level of detail is lacking.

To improve the rendering we calculated the opacity (alpha) values from the two channels first. Differencing the alpha data creates a shadow map similar to the operation in example two. Alpha data is modulated with the differential data. In comparison to example 3, the differential data needed to be attenuated by pre-multiplication to reduce artifacts. The resulting shadow was very subtle and nearly invisible, but still aided in visual depth perception (Figure 14). The ER is now perceived as a volumetric structure and is clearly positioned above the actin fibers, except for some small areas where actin fibers lead to a slightly yellowish color of the ER, i.e., where ER and actin almost co-localize. The cell boundaries are clear, and the fine structure is generally enhanced.

Thus, image processing operations in conjunction with alpha blending can significantly enhance perception and quality of volumetric visualization, and the resulting images reproduce much better on a wide variety of media including print.



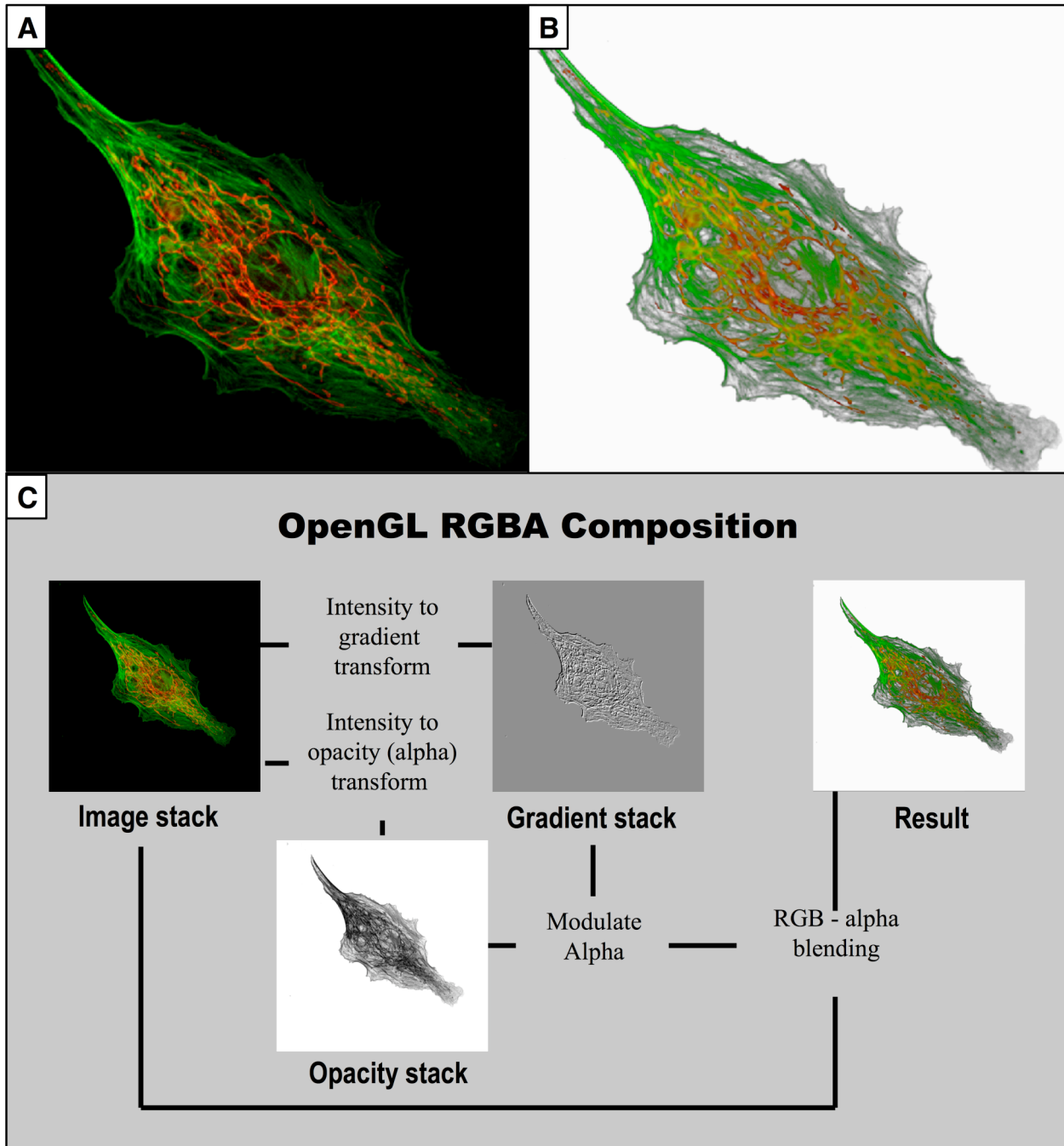


**Figure 14: Combination of Intensity Inversion and Artificial Shading**

*Fibroblast with endoplasmic reticulum (red) and actin (green) A) MIP of both channels B) Alpha rendering against a white backdrop with gradient shadow. C) Composition of fluorescence, gradient, and opacity stack against a white backdrop. Results of Volume Investigation*

**Embryonic Zebrafish Lactotrophs**

Zebrafish regulate salt and water homeostasis through peripheral osmoregulatory organs. These organs are under pituitary control through the hormone prolactin. For our experiment we generated germline transgenic zebrafish. Red fluorescent protein (RFP) is

expressed under the Prolactin regulatory elements (PRL-RFP), and green fluorescent protein (GFP) is controlled by Proopiomelanocortin promoter (POMC-GFP). These constructs enable the *in vivo* analysis of the role of these molecules in osmotic homeostasis.

Zebrafish embryos are almost transparent and therefore ideal for confocal analysis. The fluorescent proteins serve as targeted fluorescent markers for two pituitary lineages involved in teleost osmotic adaptation. We showed that dynamics of pituitary ontogeny can be traced *in vivo*. Changes in response to altered salinity could be recorded.

The developing zebra fish embryos were placed in a heated incubation chamber mounted on the confocal microscope. The head region was scanned as a 3-D image stack that covered the complete volume of the developing pituitary. The two fluorescent channels were optimized for high sensitivity by opening the spectrophotometer. The sample was scanned in sequential mode to prevent spectral overlap. A third channel recorded the conventional transmitted light image.

The results show that physiological osmotic changes selectively regulate lactotroph, but not corticotroph, proliferation during early ontogenesis. These changes are not suppressed pharmacologically by dopamine receptor blockade. PRL receptor signaling exerts robust effects on lactotroph development and plays a permissive role in lactotroph osmo-responsiveness, reflecting the dual peripheral and central interactions required for early pituitary development and embryonic homeostasis (33).

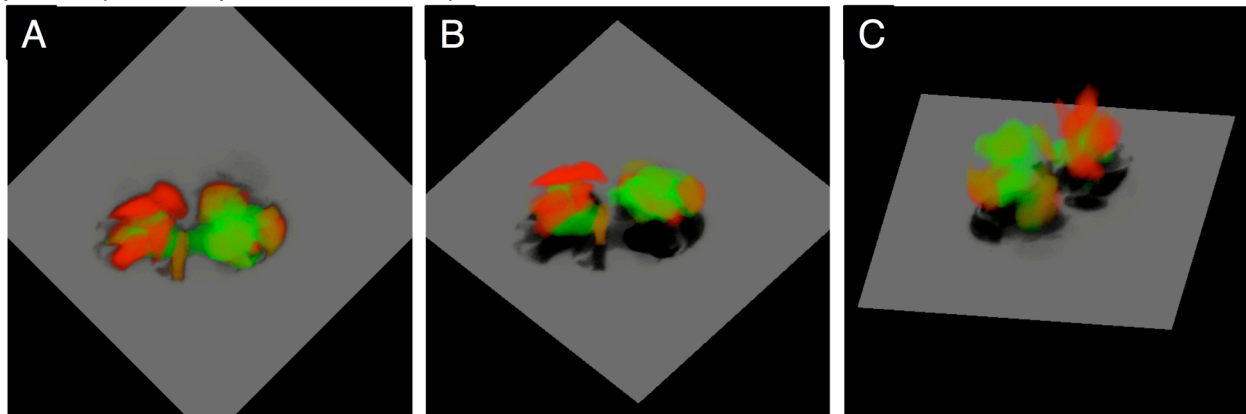


**Figure 15: Zebrafish Pituitary 3-D Reconstruction**

*In vivo* time-lapse imaging of PRL-RFP (red) and POMC-GFP (green) Alpha blending with drop shadow shows three-dimensional architecture.

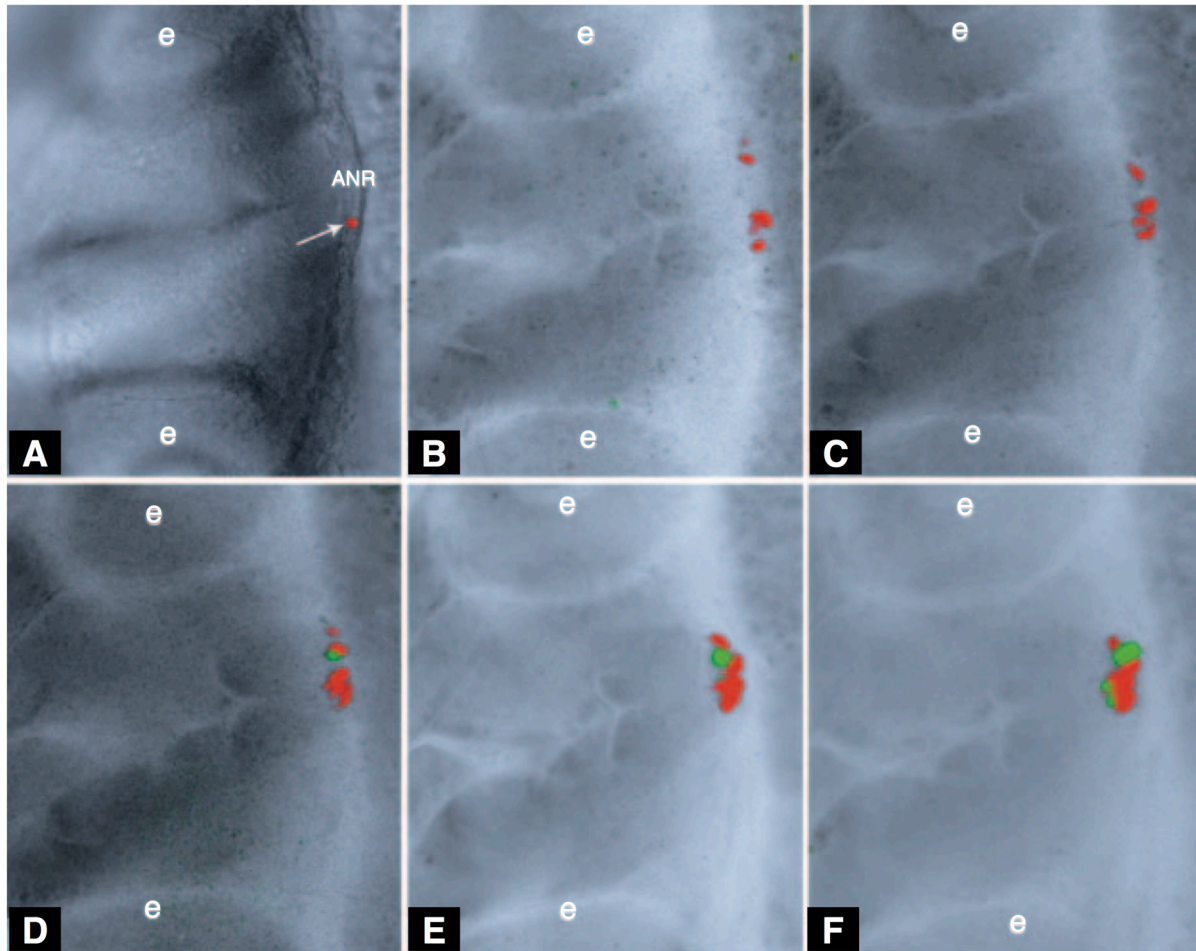


**Figure 16: Embryonic Pituitary Lactotroph and Corticotroph Ontogeny in Germline POMC-GFP/PRL-RFP Transgenic Zebrafish**

*A–F, In vivo time-lapse imaging of PRL-RFP and POMC-GFP expressing-cell ontogeny in zebrafish pituitary anlage visualized from 18–26 hpf (hours post fertilization). The first PRL-RFP expressing cell (arrow) appears on the right lateral side of the anterior neural ridge at 18-somite stage, 18 hpf (A), which is then followed by bilateral lactotroph differentiation and medial migration (B–C; B: 19.5 hpf, C: 20 hpf). After four hours, POMC-GFP-positive cells appear on the left side of the anterior neural ridge and continue to differentiate thereafter (D–F: D, 22 hpf, E: 23 hpf, F: 26 hpf). The eyes are indicated by (e) as reference points. ANR, Anterior neural ridge.*

*Figure adapted from (34).*

**PTTG1 is not Neuroprotective**

Invasive physical injury to the nervous system was shown to trigger degeneration of axons and neuroglia (35). This process is called Wallerian degeneration. To examine factors involved in that process in rodents, neurons in the extremities of mice were injured. As a consequence, distal axons, sensory and motor terminals degenerate within 18-36 hours (36). However, in Wld mutant mice the degenerative process is markedly slower (37). The

Wld gene has a nuclear localization *in vivo* (38). Therefore it *cannot* directly influence the distal degenerative processes. It is rather most likely that neuroprotective action is mediated through altering intracellular signaling pathways.

We tested the hypothesis that the securin Pttg is involved in the downstream signaling process. Wld downregulates Pttg significantly. Pttg is an oncogene and has a function in chromosome separation during mitosis. RNA microarray analysis shows a 7-8 fold down-regulation of Pttg (35).

To test our hypothesis we investigated neurodegenerative processes in Pttg null mutant mice. These mice do not have any Pttg. The degeneration was analyzed with confocal microscopy. Neurons were stained with FM-143, and terminals with fluorescently labeled Bungarotoxin (from Molecular Probes, Eugene, OR). FM lipophilic styryl compound was used to stain plasma membranes.

The plasma membranes of neurons degenerate quickly and are a good marker for neuronal injury. Motor endplates, however, are not affected by those degenerative processes and remain intact. Bungarotoxin binds highly selective to motor endplates. To measure the degree of degeneration we counted the numbers of motor endplates with and without FM 143 staining. Their ratio is a good measure for the progression of the process. Confocal microscopy provided optical sectioning and background rejection of autofluorescence. Surgically removed nerves were incubated with the staining solution according to the manufacturer's protocol. The samples was suspended in PBS on a coverslip and imaged directly.

The morphology of motor endplates and neuron fibers was reconstructed with transparency projection. That projection allows following the neurons for an extended length, because several focal planes are merged into one image. The morphology and composition of motor endplates are shown for wild-type (Figure 17) and Pttg *-/-* transgenic mice.

The experimental outcome did not show any retardation of neuronal degeneration between WT and Pttg *-/-* mice. This indicates that the Pttg downregulation is an upstream event and not mediated by Wds (35).



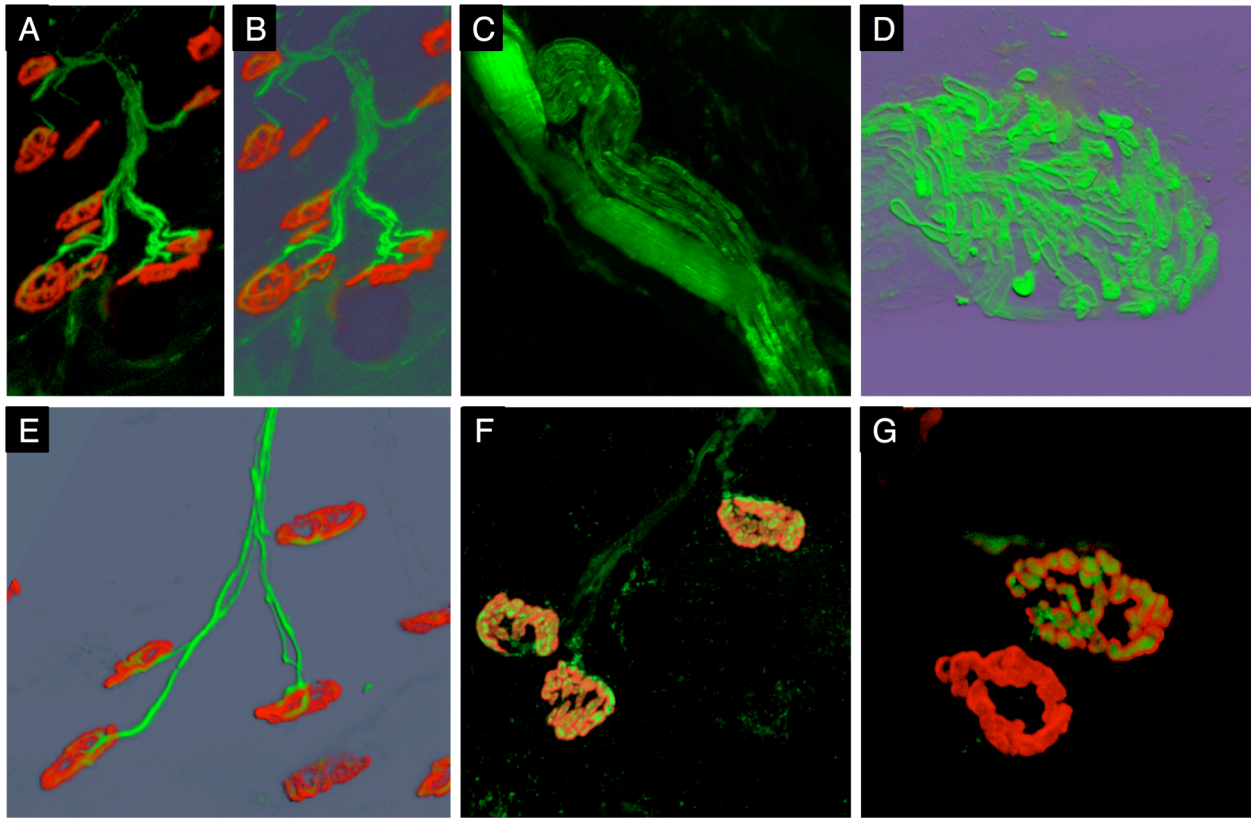


**Figure 17: Reconstruction of neurons and motor endplates**

*The neurons are stained with FM 143 (green) and motor endplates with TRITC conjugated Bungarotoxin (red). A) MIP of normal motor endplates (red) and neuron bundles (green). B) same as A but as alpha projection against a gray background. The projection enhances dimmer detail. C) An intact neuron bundle without endplates. D) Cross-section through a bundle. Each neuron appears as a hollow tube, since FM only stains the membrane. E) Neurons start to degenerate. Some endplates do no longer show FM staining. F) Neurons degenerate first while endplates still show FM staining. G) Detail of degeneration of endplates. One of them shows no FM staining.*

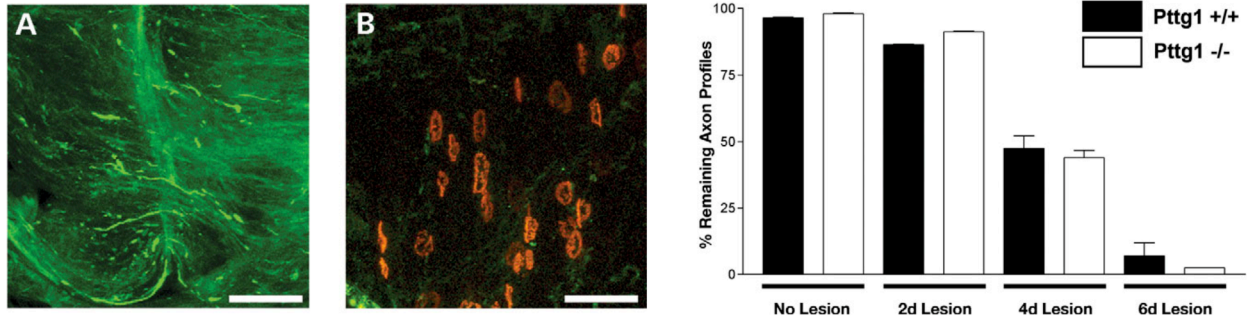


**Figure 18: Pttg1 mutant mice show no neuroprotective phenotype *in vivo***

(A) *pttg12/2* mouse tibial nerve immunostained for 165 – kDa neurofilaments, showing fragmentation of axon profiles 3 days after sciatic nerve lesion. (B) *pttg12/2* mouse deep lumbrical muscle 2 days after sciatic nerve lesion stained with FM1-43 (green) and TRITC-conjugated alpha-bungarotoxin (red). No FM1-43-positive motor nerve terminals were found in any of the muscles examined (N 6). All terminals in contralateral unoperated muscles stained with FM1-43 (data not shown). (C) Quantification of axon profile preservation in the tibial nerve of *pttg12/2* (ko) and *pttg1* (wt) mice at 2, 3 and 6 days post-sciatic nerve lesion (mean + SD; N 2 for *pttg1 2/2* and 1 for *pttg1* per time-point). There was no difference in the onset or rate of degeneration between the two experimental groups. Scale bars: 50  $\mu$ m  
 Figure reprinted from (35)

## Calcium Flux

Ions move across cell and organelle membranes through special channels and pumps created by proteins. This leads to concentration gradients between exterior and interior compartments as well as the cell and its environment. Ion channels participate in, and regulate, cellular processes as diverse as the generation and timing of action potentials, energy production, synaptic transmission, secretion of hormones and the contraction of muscles. In fact, many drugs exert their specific effects via modulation of ion channels. Examples include antiepileptic compounds like phenytoin and lamotrigine, which block voltage-dependent sodium channels in the brain, antihypertensive drugs like nifedipine and diltiazem, which block voltage-dependent calcium channels in smooth muscle cells, and stimulators of insulin release like glibenclamide and tolbutamide, which block ATP-regulated potassium channels in the pancreas (39).

There are many types of ion channels including, for example, ligand-gated channels, which open or close in response to the binding of signaling molecules. Channels respond to a wide variety of external and internal factors (40-42):

- Cyclic nucleotide-gated channels open in response to and mediate cellular responses to second messengers.
- Stretch-activated channels open or close in response to mechanical forces that arise from local stretching or compression of a membrane.
- G-protein-gated channels open in response to G protein-activation via receptor.
- Voltage-gated channels open or close in response to changes in the charge across the plasma membrane.

Finding new drugs which have specific modulatory effects on ion channels requires methods for measuring and manipulating the membrane potential and/or concentration gradient of cells with the ion channels present in their membrane. A number of methods exist to measure cell transmembrane potentials, concentration gradients, and the activities of specific ion channels. For example, patch-clamp recording was the first technique capable of monitoring the function of single biological molecules. Patch clamping can measure single-channel currents (43,44). Using the patch-clamp technique, the properties of ion channels can be studied by means of a very fine pipette (with an opening of about 0.5  $\mu\text{m}$ ). The pipette is pressed against the plasma membrane of either an intact cell or is used to pull away the plasma membrane from the cell. The sample is subjected to a test solution of desired composition. In so doing, current flow through a single ion channel can then be measured (43,44).

Several techniques are known for performing patch-clamp recordings that are suitable for drug discovery:

- Whole-cell patch clamp technique
- Concentration clamp technique
- Pressure clamp method
- Perfusion of patch clamp electrodes,
- Loose patch-clamp technique with single-channel recording
- Perforated patch-clamp technique.

Despite the wide variety of approaches, a major limitation of the patch clamp technique as a general method in pharmacological screening is its low throughput. Typically, a single, highly trained operator can test fewer than ten compounds per day using the patch clamp technique. Furthermore, the technique is not easily amenable to automation, and produces complex results that require extensive analysis by skilled electrophysiologists.

### **Optical Calcium Recording**

The use of optical detection systems provides for significantly greater throughput. Screening applications and advances in optical techniques have allowed direct visualization of calcium signaling at the cellular and subcellular level (45-47) Advances in the development of video imaging and confocal microscopy have led to the discovery of polarized subcellular calcium signals in various cell types. The shape of intracellular calcium signals (i.e., their amplitude and frequency) is determined by the distribution of calcium-releasing channels and mechanisms that limit calcium elevation (48). In addition, development of new cell permeable fluorescent reporters, such as luminescent photoproteins, fluorescent proteins, and fluorescent dyes, has opened the way for dynamic cellular assays by allowing activity at drug targets to be determined in living cells (49).

Drug discovery is a long and multi-step process involving identification of specific disease targets. Discovery typically comprises the following steps:

- Development of an assay based on a specific target
- Validation of the assay
- Optimization and automation of the assay to produce a screen
- High throughput screening of compound libraries using the assay to identify “hits”
- Hit validation and hit compound optimization

The output of this process is a lead compound that goes into pre-clinical validation. If validated it will eventually go into clinical trials. In this process, the screening phase is distinct from the assay development phases, and involves testing compound efficacy in living biological systems.

## **Pharmacological Analysis**

We present a novel method to study dose-dependent modulation of calcium oscillations in live cells. Confocal ion imaging is able to record single cell responses to increasing drug doses over up to 8 orders in magnitude. Dose response curves and other pharmacological parameters were obtained by offline image and data analysis.

We used AtT-20 corticotroph pituitary cells, which exhibit naturally occurring calcium oscillations. We compared attenuation of oscillations by the L-type calcium channel blocker nimodipine to somatostatin signaling. Somatostatin and nimodipine modulate the amplitude but do not change patterns of oscillations (50).

Analyzing single cell amplitude modulation in a dose dependent manner allows identification of non-viable cells and their exclusion based on objective criteria. We described statistically significant pharmacological data over cell populations and exclude toxic effects from the analysis (50). This method for single cell quantification of drug effects on oscillations will lead to screening for development of novel drugs.

## **Screening Methods**

Bioinformatics, genomics, proteomics and high throughput screening have become indispensable in identifying potential new drug targets. They predict drug interactions and increase capacity and efficiency in the areas of target identification. However, even with these developing technologies, there is a need to measure multi-dimensional information from cells. These aspects of drug discovery make the observation of ion fluctuation particularly suitable to a simultaneous measurement of multiple parameters of cell response to compound administration. Optical imaging methods are the method of choice to screen large numbers of compounds.

The conventional measurement in early drug discovery assays was radioactivity. However, the need for easier handling, higher throughput and miniaturization has caused a shift towards using fluorescence detection. Fluorescence-based reagents can yield more powerful, multi-parameter assays. These are higher in throughput and information content, and they require lower volumes of reagents and test compounds. Fluorescence technique is safer and less expensive than radioactivity-based methods.

## **Automated Ion Imaging**

Conventional means of imaging fluorescent samples provide calculations of total fluorescence average over a cell sample. For example, Science Applications International Corporation (SAIC, Seattle, WA) describes an imaging plate reader that uses a CCD camera to image the whole area of a 96 well plate. The image is analyzed to calculate the total fluorescence per well for all the material present in the well. Similarly, Molecular Devices, Inc. (Sunnyvale, CA) describes a system (FLIPR) which uses low angle laser scanning illumination and a mask to selectively excite fluorescence within approximately 200 microns of the bottoms of the wells in standard 96 well plates in order to reduce background when imaging cell monolayers. This system uses a CCD camera to image the whole area of the plate bottom. Although this system measures signals originating from a cell monolayer at the bottom of the well, the signal measured is averaged over the whole

area of the well and is therefore still considered a measurement of the average response of a population of cells. The image is analyzed to calculate the total fluorescence per well for cell-based assays. Fluid delivery devices have also been incorporated into cell based screening systems, such as the FLIPR system, in order to inject a compound. Responses are observed as a whole well population average response using a macro-imaging system.

Biological cell populations generally are heterogeneous. Thus the high spatial and temporal frequency of chemical and molecular information present within cells makes it impossible to extract high-content information from populations of cells when using conventional techniques. Conventional techniques for monitoring and analyzing, for example ion oscillations using fluorescence, have substantial drawbacks. Photo-bleaching and lack of specific information concerning individual cells limits the amount of information that can be obtained. Some techniques also are not fast enough, or not cost-efficient. Dose-dependent experiments using the patch-clamp technique typically require two days to be completed.

In contrast to high throughput screens, high-content screens have also been developed to address the need for more detailed information about spatial-temporal dynamics of cell constituents and processes. High-content screens automate the recording and analysis of multicolor fluorescence information derived from specific fluorescence-based reagents incorporated into cells. Cells are analyzed using optical systems that can measure spatial, spectral and temporal parameters (51). With high-content screening, the concept is to treat each cell as a "well" that may give spatial and temporal information on the activities of its labeled constituents.

High-content screens can be performed on fixed cells using fluorescently labeled antibodies, biological ligands, and/or nucleic acid hybridization probes. Live cells can be analyzed with multicolor fluorescent indicators and biosensors such as visible fluorescent proteins and vital dyes. The choice of fixed or live cell screens depends on the specific cell-based assay required. Fixed cell assays provide an array of initially living cells in a microtiter plate format, which can be treated with various compounds and doses being tested. Thereafter cells are fixed, labeled with specific reagents, and imaged. No environmental control of the cells is required after fixation.

The drawback of fixed cells is that spatial information is limited to a single time point. Live cell assays provide a view of living cells containing the desired reagents, which can be screened over time and space screening. Care should be taken that the screening method does not introduce measurement artifacts. Environmental control of the cells (temperature, humidity, and carbon dioxide) is required during measurement, since the physiological health of the cells must be maintained over time. Fluorescent physiological indicators and biosensors can report changes in biochemical and molecular activities within cells.

### **Live Cell Imaging**

Scanning confocal microscope imaging is a well-established method for acquiring high-resolution images of microscopic samples. These optical systems provide for shallow depth of focus, which allows to depict features of limited axial extent to be resolved against the background. For example, it is possible to resolve internal cytoplasmic features of adherent

cells from the features on the cell surface. However, these imaging methods are limited by the efficiency, photo stability and toxicity of the fluorescent dye in the chosen system, and the illumination itself. Thus, there remains a need for instrumentation and for methods to directly measure ion oscillations of individual cells in a sample as a result of dose-dependent administration of a compound.

### **Calcium Channel Agonists**

One example of ion oscillation occurs in calcium ( $\text{Ca}^{2+}$ ) channels, which are generally found in living cells where, among other functions, they play important roles in signal transduction. In excitable cells, intracellular calcium supplies a maintained inward current for long depolarizing responses and serves as the link between depolarization and other intracellular signal transduction mechanisms. Like voltage-gated sodium channels, voltage-gated calcium channels have multiple resting, activated, and inactivated states.

Calcium channel antagonists are potent vasodilators and are widely used in the treatment of hypertension, and angina pectoris. Clinically approved compounds in the United States include, for example, dihydropyridines (e.g., amlodipine, felodipine, nifedipine, nicardipine, isradipine, nimodipine); benzothiazepines (e.g., diltiazem), phenylalkylamines (e.g., verapamil); and diarylaminopropylamine ether (e.g., bepridil) (52).

### **Calcium in Endocrine Cells**

Endocrine cells, including gonadotroph, somatotroph, and corticotroph cells, exhibit baseline spontaneous calcium oscillations (BSCOs) *in vitro* as well as in their native environment (53-55). Minor differences in baseline and stimulated calcium oscillation patterns have been noted between normal corticotroph and AtT-20 cells (56). Baseline spontaneous calcium oscillations may represent the sum of cellular calcium channels mediating replenishment and maintenance of calcium concentrations required for intact calcium dependent signaling pathways and cellular homeostasis (57). Their importance for regulation of ACTH secretion has also been described (58). Understanding these oscillations and their underlying mechanisms is important for cellular physiology as well as screening for novel drug treatments (59).

Calcium oscillations are caused by repetitive periodic release of calcium from internal stores, followed by subsequent recharging. Generally, calcium release-activated calcium channels (CRAC) as well as arachidonate-regulated calcium channels (ARC) contribute to oscillations (60). However, at low agonist concentrations, ARC channels dominate calcium oscillations. In contrast, at higher concentrations, depletion of calcium stores becomes more profound, and activation of CRAC channels leads to constantly elevated levels (60).

### **Calcium Channel Types**

The different types of calcium channels have been broadly categorized into four classes, L-, T-, N-, and P-type, distinguished by current kinetics, holding potential sensitivity and sensitivity to calcium channel agonists and antagonists. L-type calcium channel antagonists such as nimodipine block spontaneous oscillations in AtT-20 clonal pituitary cells (61). In contrast, voltage-gated sodium channels are not involved in spontaneous calcium oscillations. Moreover, while AtT-20 cells have been shown to have T-type and L-

type channels, only L-type channel antagonists reversibly block oscillations. Indeed, activation of L-type channels produces large, transient and sustained calcium oscillations (61). Changes in oscillation patterns have also been studied in AtT-20 cells in response to norepinephrine and somatostatin (62).

Calcium channels mediate the influx of  $\text{Ca}^{2+}$  into cells in response to changes in membrane potential and/or concentration gradient, and because of their central roles in ion homeostasis and in cell signaling events, these channels are involved in a wide variety of physiological activities; for example, muscle contraction, cardiovascular function, hormone and neurotransmitter secretion, and tissue growth and remodeling processes. Multiple types of calcium channels have been identified in mammalian cells from various tissues, including skeletal muscle, cardiac muscle, lung, smooth muscle and brain. Not surprisingly, calcium channels are recognized as important targets for drug therapy. They are implicated in a variety of pathologic conditions, including, for example, essential hypertension, angina, congestive heart failure, arrhythmias, migraine and pain.

### **Calcium in AtT20 Pituitary Tumor Cells**

Endocrine cells exhibit spontaneous  $\text{Ca}^{++}$  oscillations *in vitro* as well as in their native environment (53). Understanding these oscillations and their underlying mechanisms is important for cellular physiology as well as screening for novel drug treatments (59).

Calcium release-activated calcium channels (CRAC) as well as arachidonate-regulated calcium channels (ARC) contribute to oscillations (60). At low agonist concentrations ARC channels dominate calcium oscillations. At higher concentrations depletion of calcium stores becomes more profound, and activation of CRAC channels leads to constantly elevated levels.

L-type calcium channel antagonists such as nimodipine block spontaneous oscillations in AtT-20 clonal pituitary cells (61). Voltage-gated sodium channels were not involved in spontaneous calcium oscillations. While AtT-20 cells were shown to have t- and l-type channels, only l-type channel antagonists reversibly blocked oscillations. Activation of l-type channels produced large, transient and sustained oscillations.

Changes in oscillation patterns have been studied in AtT-20 cells in response to norepinephrine as well as somatostatin (62). Somatostatin did not depress depolarization dependent calcium stimulation. However, all prior experiments observed the effect of large (2  $\mu\text{M}$ ) doses of l-type channel antagonists on artificially stimulated cells. Responses at lower doses on spontaneous oscillations were not reported.

Our goal was to obtain detailed dose dependent data of calcium modulation responses on spontaneous oscillations. We recorded how l-type channel activity modulated calcium oscillations by applying channel antagonists with increasing doses while simultaneously observing single live cell calcium oscillations. This allowed us to compare multiple cells in the same experiment and acquire statistical data over larger cell populations. We fit sigmoidal dose response curves to each individual cell and calculated the average response over the total population.

To enable these studies we optimized confocal microscopy to image calcium oscillations with a temporal resolution of 3 frames per second (fps) for up to 45 min total recording



time. To limit photo-damage we resorted to an asymmetric imaging method. The illumination was diffraction limited, but the detection almost wide-field by opening the confocal detection pinhole completely. This allowed superior detection efficiency, while still suppressing background fluorescence. During the recording time we increased drug concentrations over 8 orders of magnitude and recorded intensity fluctuation of fluorescent calcium indicator dye.

We also compared the attenuation of oscillations by nimodipine with the attenuation effects of the somatostatin agonist SRIF 28. We were therefore able to derive data about signaling pathway modulation of calcium signals. In principle calcium fluxes can be modulated in the amplitude (AM) or frequency (FM) domain (48), as was shown in prolactin releasing GH3 cells (63). We now show that oscillation amplitude is modulated in a dose dependent manner by both nimodipine and somatostatin.

## **Materials and Methods**

### **Cell Culture**

AtT-20/D16-F2 mouse ACTH-secreting pituitary cells (CRL-1795; American Type Culture Collection; 2003) were grown in serum-containing low glucose DMEM (Invitrogen, Carlsbad, CA) supplemented with 10% fetal bovine serum (Omega Scientifics, Tarzana, CA), with addition of 2 mM glutamine and 1% antibiotic/antimycotic [100 U/mL penicillin G sodium, 100 µg/mL streptomycin sulfate, 250 ng/mL amphotericin B (Fungisone in 0.85% saline)] (Invitrogen, Carlsbad, CA), in 6% CO<sub>2</sub>, 37°C humidified incubator.

For confocal imaging, cells were grown in 6 well plates on 25 mm cover slips coated with 10 µg/ml poly L-lysine (Sigma Aldrich, St. Louis, MO) to 70% confluence in low glucose DMEM with 0.3% BSA 12 hour prior to analysis.

For ion imaging, cells were stained with Calcium Green-1 AM 488 dye (Molecular Probes, Eugene OR) according to the instruction of the manufacturer. Briefly, cells were suspended in 1 µM solution of Calcium Green dye aided by the nonionic detergent Pluronic F-127 (10% solution in water) for 30 min. 25 mm cover slips were transferred to an Attofluor cell culture chamber (Molecular Probes, Eugene, OR) and filled with 1 ml serum free culture medium.

### **Confocal Cytosolic Calcium Imaging**

The Attofluor cell culture chamber was placed inside a PenCon temperature controlled incubator at 37°C mounted on a DM IRBE inverted microscope (Leica Microsystems, Wetzlar, Germany). Cells were imaged with a TCS/SP confocal scanner (Leica Microsystems Heidelberg, Mannheim, Germany) using a temperature controlled 63x/1.2 N.A. W PlanApo water immersion objective. We checked the digital temperature readout of the incubator with a calibrated mercury thermometer to confirm the values within 0.2°C.

For excitation we used the 488nm Argon laser line with laser power set to minimum and 488 nm AOTF line to 9% transmission.

Time lapse sequences were acquired by setting the scanner to medium scan speed, and bidirectional scan mode at 128 by 128 pixel resolution, resulting in a scan rate of about 3 fps (350 ms / frame). For time resolution test we increased the scan rate to 10 fps by changing to fast bidirectional scan mode. The pinhole was opened to 3.5 Airy units for maximum collection efficiency.

### **Dose Response Acquisition**

Cells were imaged over a 5 min time interval for each dose. Baseline values were acquired with a 5 min pre-treatment interval. Consecutively, we added the drug of choice at increasing doses at one order of magnitude increments for each 5 min interval. In each experiment total recording time was 45 min. Each 5 min interval was stored as a separate time series of TIFF files within duration of the 45 min experiment.

### **Measurement and Analysis**

Time sequences of images were manually analyzed in ImageJ software (National Institutes of Health, Bethesda, MD) by importing TIFF files from one 5 min recording interval (corresponding to a single dose) into a stack. Intensities were measured manually by drawing a region of interest (ROI) around each cell and using the stack profile measurement function. This function measures the average brightness of each ROI over time. The resulting numerical values were transferred to the Excel software (Microsoft Corporation, Redmond, WA) spreadsheets.

We calculated the ratio

$$R = \frac{f_{\min} - f_{\max}}{f_{\text{median}}}$$

over a 6s sliding time frame, and we averaged the calculated ratios over each 5 min interval for final analysis. The resulting table contains the average ratio for each cell and dose at one data point.

These values were transferred to Prism software (Graphpad Software, San Diego, CA) for curve fitting and statistical analysis. For the final results the amplitude values were normalized and a sigmoidal dose-response curve was fitted with variable slope to either each cell or an average over the population.

## **Results**

### **Confocal Imaging**

The challenge was to image cells over extended time periods at sufficiently high frame rates. Toxic effects could be triggered directly by excitation light, or indirectly by toxic products of photo converted (photo bleached) dye molecules, or the molecules themselves. To solve the problem to decide between these possibilities we decreased the resolution to an absolute minimum by scanning with 128 to 128 pixels over a 150 by 150  $\mu\text{m}$  imaging area. Large area per pixel result in high collection sensitivity similar to pixel binning in digital cameras. In addition, we improved the sensitivity by opening the pinhole to a maximum of 3.5 Airy units and used a large spectral window for the

spectrophotometer. The excitation path still provided diffraction-limited illumination. This reduced the out-of-focus background fluorescence and kept light exposure to a minimum. In short, the illumination path was still diffraction limited (similar to regular confocal microscopy), and the detection path was wide field for maximum sensitivity.

For ion imaging we used Calcium Green calcium sensitive dye. The advantage over dual excitation ratiometric dyes was two-fold. Single wavelength excitation reduces exposure to light since only one wavelength is required. Single wavelength emission maximizes detection sensitivity since one detector captures all available photons emitted. Secondly the lower excitation wavelength of Calcium Green, as compared to UV excitation of dual wavelength dyes, is less damaging to cells.

To acquire images at sufficient temporal resolution and to prevent aliasing artifacts, we imaged oscillations with the maximum scan frequency available (10 fps) and derived the lowest acceptable scan frequency from the recorded data.

### **Validating Sampling Frequency**

We recorded spontaneous calcium oscillations with 10 fps and plotted the resulting data (Figure 19). The graph shows that oscillations are clearly resolved at 10 fps. To verify that sampling at 3 fps is still sufficient we derived 3 curves from the original data by sampling every 3rd data point, and we obtained 3 curves by offsetting the subsampling by 1 and 2 values, respectively. Resulting plots are shown in Fig 1b. The 3 derived curves show that subsampling at 3 frames per second does not introduce significant sampling error, and thus oscillations are still well resolved.

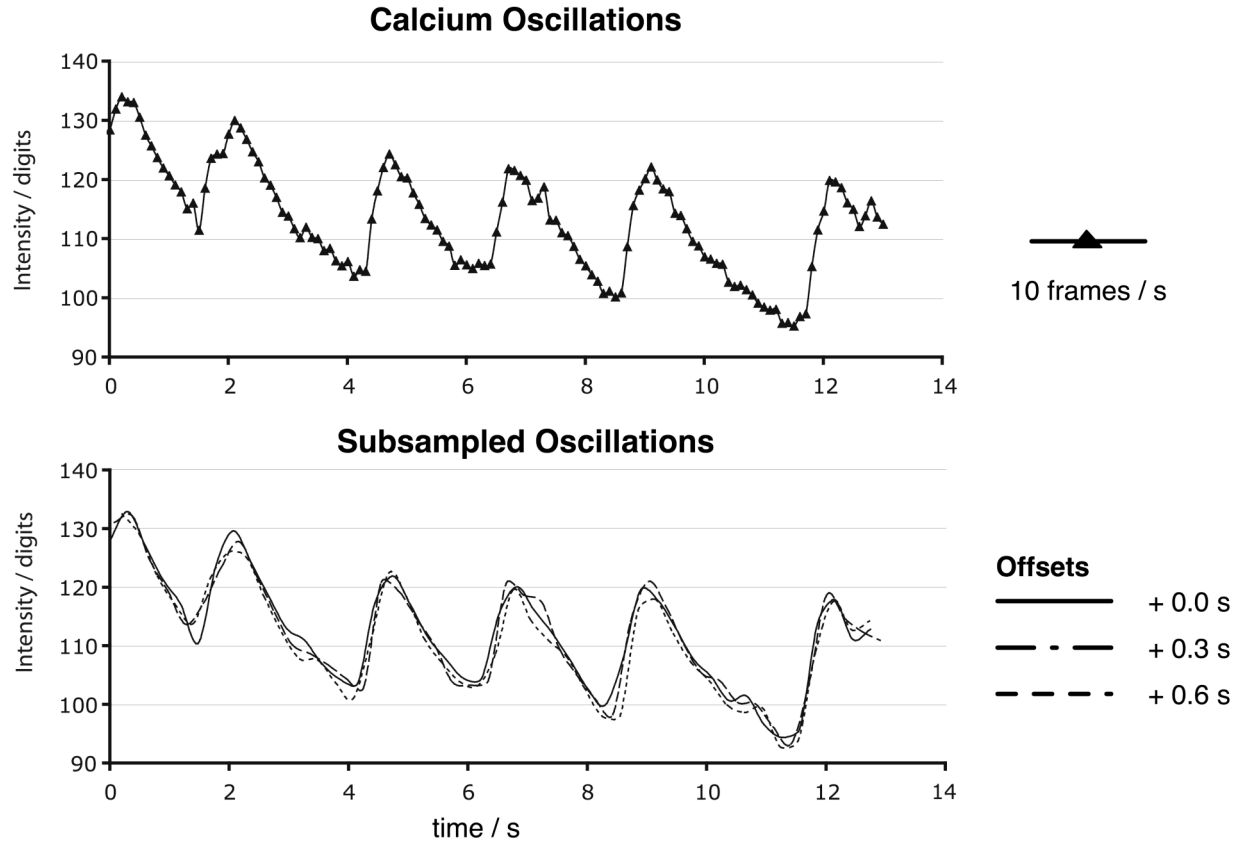


**Figure 19: Sampling of calcium oscillations**

The upper graph shows a representative sample of calcium oscillations scanned with 10 frames per second. The lower graph shows oscillations down-sampled to 3 frames per second. Curves have an offset of 0, 1, and 2 frame offset.

### Recording Calcium Oscillations

Calcium Green is a single wavelength calcium indicator and changes intensity significantly with local changes in free calcium. However, any change in dye concentration, excitation intensity and detection parameters also create changes in the recorded intensity. To confirm that the imaging system and dye concentration remained stable we verified the quality and validity of the recordings by using two different approaches. First we verified that our imaging system and experimental setup did not produce significant statistic errors as the results could be successfully reproduced. Secondly, we calculated ratios similar to the method described by Bonnefont (53), as ratios are inherently robust against fluctuation in illumination intensity and photo bleaching.

In general we divided each experiment in 5 min recording intervals for each drug dose. We quantified calcium oscillations for each 5 min interval separately and repeated these intervals for up to 45 min total recording time. We validated the methodology by control experiments for both 5 min intervals and 45 min intervals. 5 min control experiments verified the quality of imaging, thus excluding artifacts from laser fluctuations, focus drifts and other imaging related problems.

45 min controls for long-term changes include detection of changes in cell behavior as well as long term stability of the imaging system.

### Controls for 5 min interval

A maximum dose of l-channel blocker was found to suppress all oscillations in AtT-20 cells. If we imaged these non-oscillating cells, any remaining fluctuation in intensity had to be caused by the imaging system itself. For a perfect system there would be no fluctuations in intensity, as changes would induce measurement artifacts. However, for all practical intents and purposes it is sufficient if these fluctuations remain significantly below the noise level.

### Bleaching and Dye Leakage

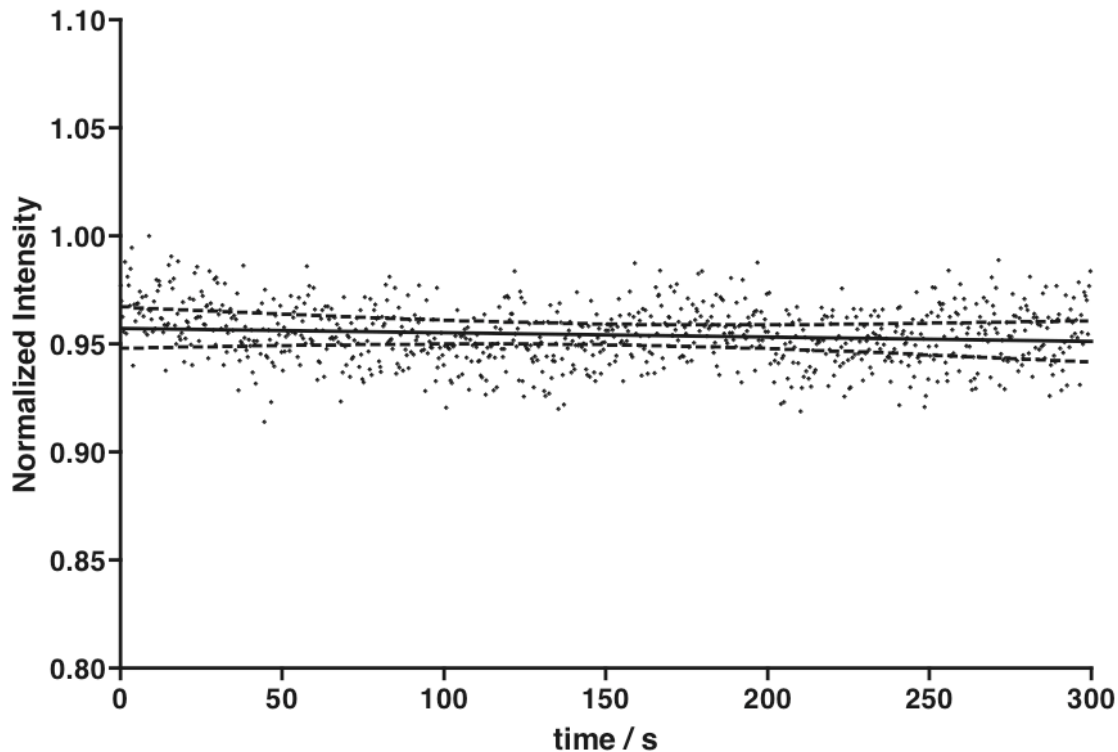


**Figure 20: Signal stability**

*The graph shows fluorescent signal during a 5 min interval. There is a small decrease due to bleaching and dye leakage. The solid line shows a linear correlation, and dotted lines 95% confidence intervals.*

We imaged 14 AtT20 cells for a 5 min interval with 3 frames a minute. Cells were first treated with nimodipine to suppress oscillations. The intensity for each cell was measured for each frame and the data transferred into the Prism software. Initially we plotted the raw data points. Because the rate of bleaching was very low we fitted a linear correlation curve to the data. The rate of bleaching is significantly smaller than 1% for the 5 min interval. Figure 20 shows the graphed intensity data for these cells.

To check for residual errors and deviations we plotted the residual values after subtracting a linear curve fit for each data point. The resulting graph (Figure 21) shows an error that is smaller than 1%, but no systematic aberration.

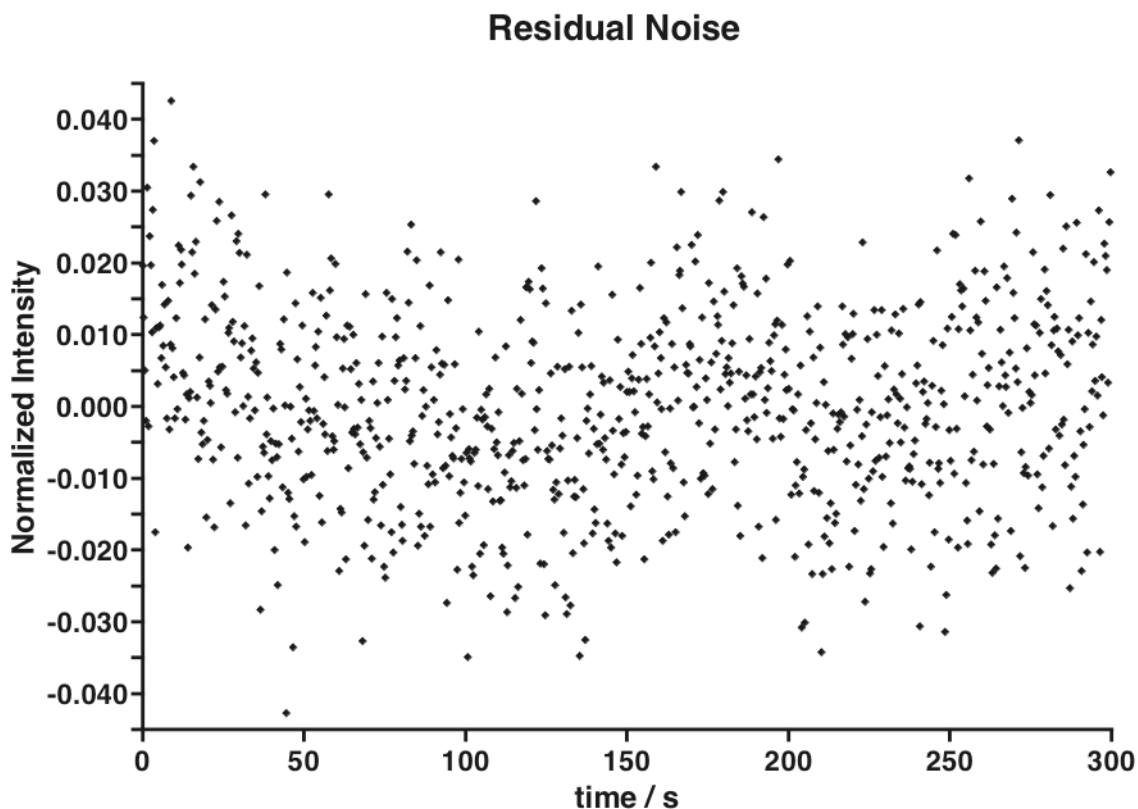


**Figure 21: Signal to Noise**

*These data points show the fluorescence signal after subtracting linear correlation of the signal for each cell. The residual noise is under 1%.*

As a result of these tests we conclude that the instrumental setup did not induce significant measurement artifacts, and that the dye concentration was stable for at least each 5 min interval.

### **Controls for 45 min Interval**

For our complete experiment cells had to be stained with Calcium Green, imaged and exposed to increasing drug doses for 45 min. We designed a series of control experiments to show that these prolonged exposures had no significant toxic effects.

In our first control we imaged untreated cells over a 45 min time span with continuous recording of 3 fps. We measured the amplitudes of calcium oscillations and plotted them over time. The results show that cellular oscillations increase slightly in amplitude over time, but oscillation patterns remained constant and cells did not exhibit any temporary or transitory changes. Oscillation amplitudes increase over the first 45 min and drop at 50 min. As the drop could indicate the onset of toxic effects, we did not record experiments longer than 45 min.

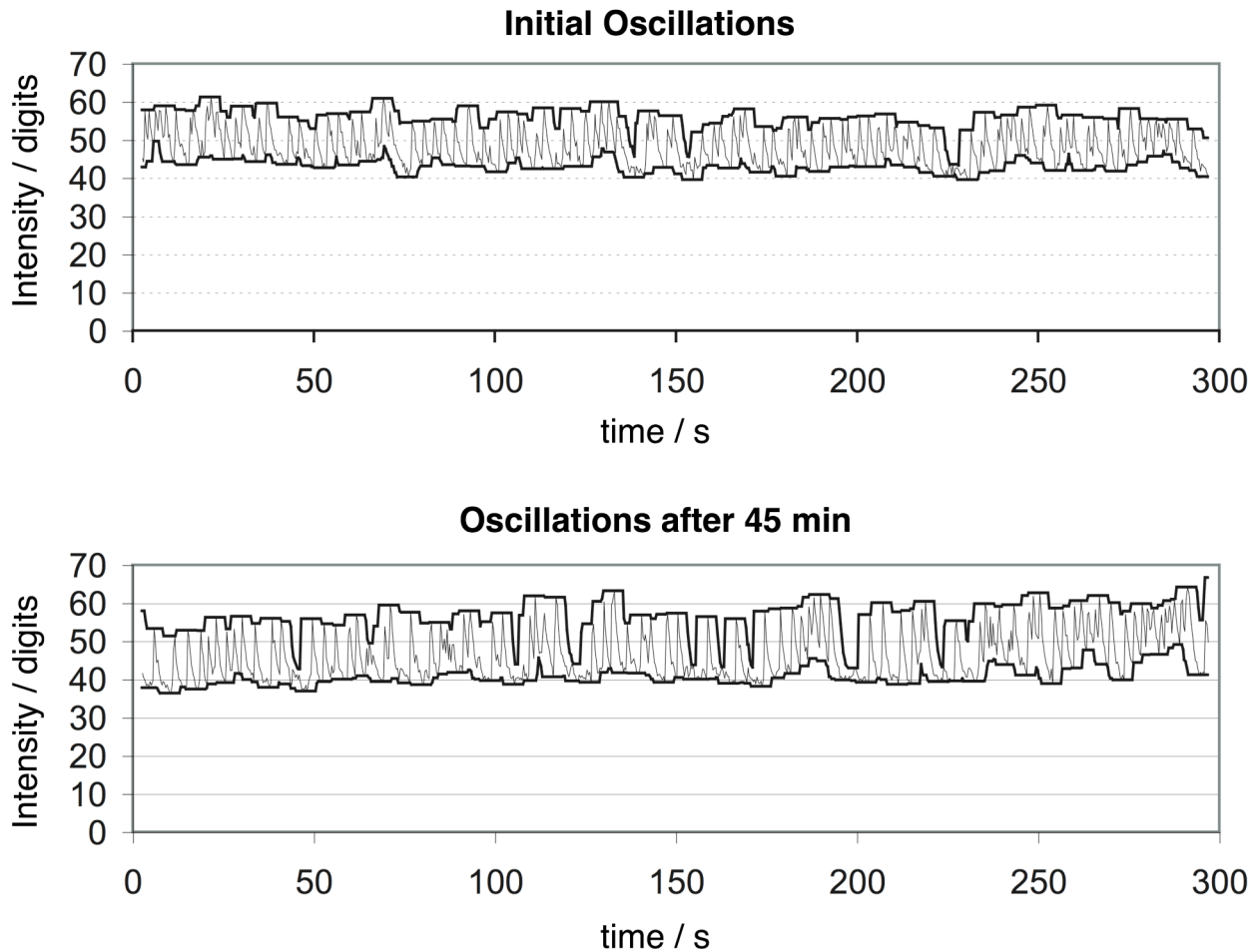


**Figure 22: Calcium oscillations over 45 min**

The graph shows the intensity of fluorescence for one representative cell for two intervals: 0 to 5 min, and 40 to 45 min. The thin line represents the recorded intensity, and the lower and upper darker lines are the calculated minimum and maximum of the signal. Oscillation amplitude of the untreated cell increases slightly over 45 min.

In a second control experiment we showed that prolonged exposure to nimodipine is not toxic to cells. Figure 23 shows the oscillations before and after treatment of one representative cell. Oscillations are significantly depressed, and the amplitude is visibly smaller.

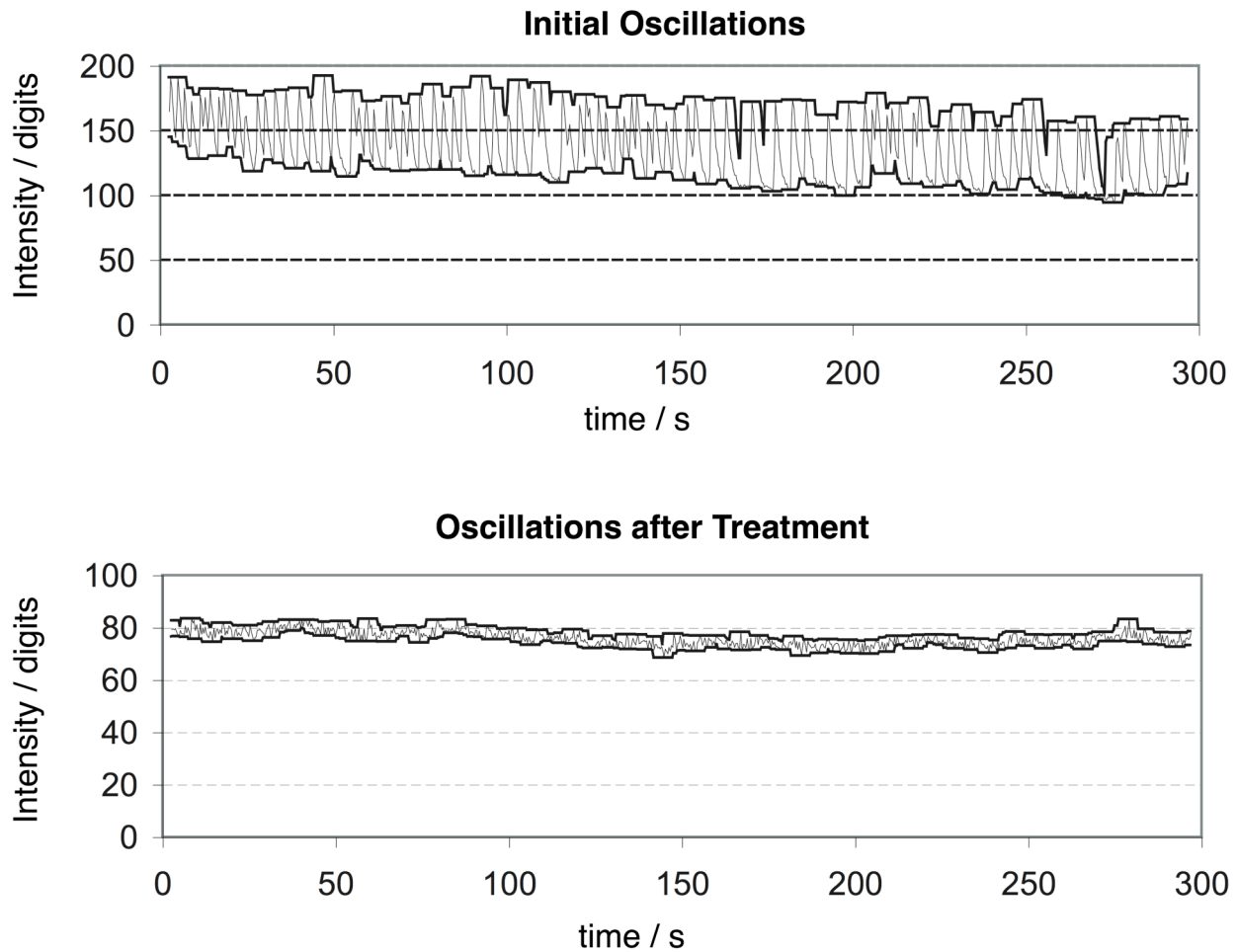


**Figure 23: Oscillations after Nimodipine Treatment**

*The graphs show the intensity fluctuations of one representative cell. Upper graph shows oscillations of the cell before treatment. Lower graph after treatment with Nimodipine. The decrease in oscillation amplitude in the second graph is due to l-channel blockage.*

To demonstrate that cells still respond even when oscillations are completely suppressed we depolarized the membrane with high  $K^+$  and recorded the resulting calcium response (Figure 24). Healthy cells respond with a transitory increase in intracellular free calcium. Damaged or dead cell do not show this response, because the membrane permeability is compromised, and calcium channels and pumps are inactive. All cells responded with an immediate, but temporary, spike in free calcium. This experiment demonstrates that cells exposed to 45 min of imaging and nimodipine treatment maintained the capacity to respond and to keep a physiological balance of free calcium.



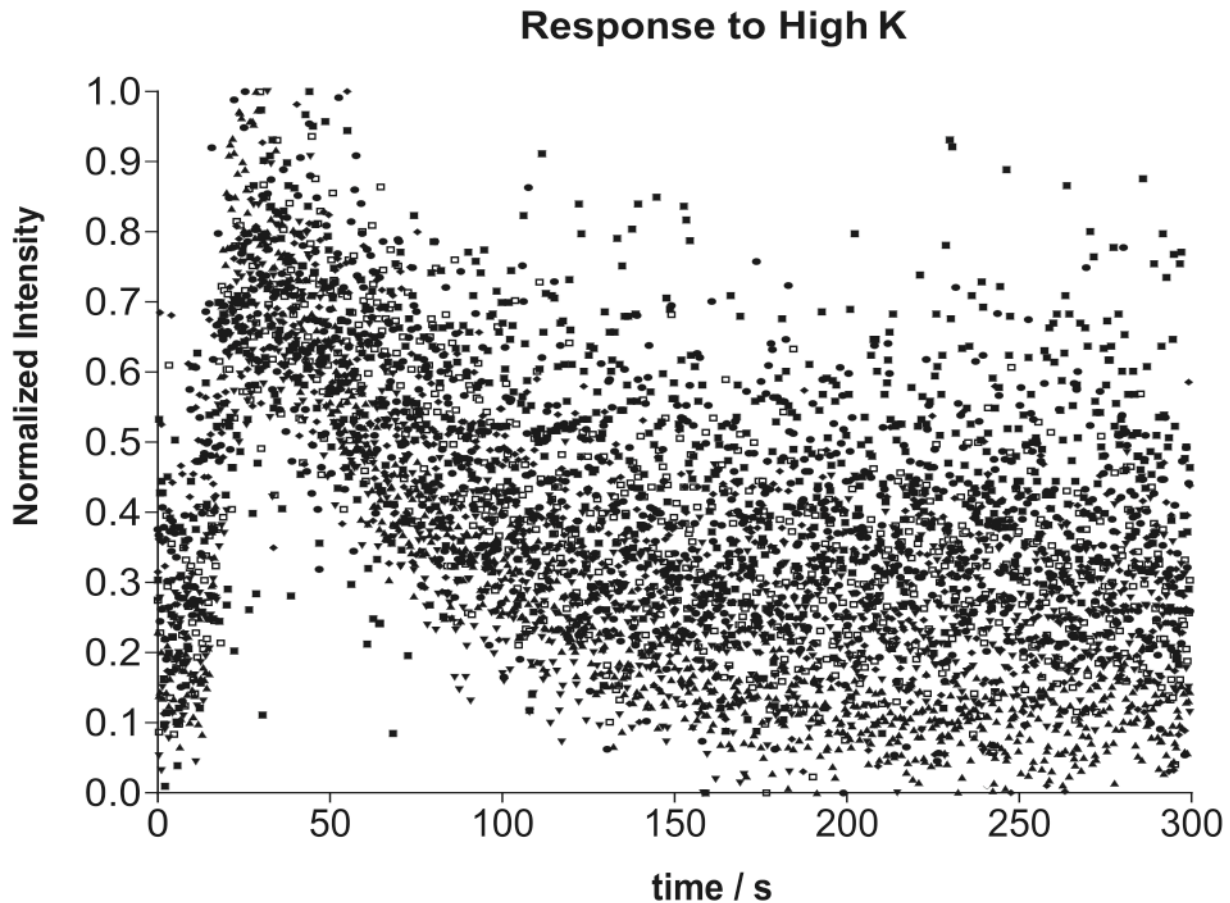


**Figure 24: Response to Potassium**

*14 cells were treated with nimodipine and scanned for 45 min. We recorded response to high K treatment to verify that cells were still physiologically responsive. The increase in intracellular calcium can be seen as an increase in fluorescence intensity. All 14 cells responded.*

### **Dose Response**

We performed dose response experiments for nimodipine and the somatostatin agonist SRIF 28. Results for three independent experiments for nimodipine are shown (Figure 25 A). The responses vary significantly between different experiments, but create a continuum. 15 cells responded evenly by reducing oscillations over a large range of doses. 7 cells responded like a threshold switch by shutting down oscillations over only two doses. 3 cells reduce oscillations only at very high doses.

The dose response to SRIF 28 is similar (Figure 25 B). However, there is a larger variation of cellular responses over the dose range, resulting in a larger measurement error.

The results demonstrate that we can use oscillation amplitude analysis of calcium ions as a measure for cellular responses to drugs. This includes drugs working directly on the calcium channels, or indirectly through signaling pathways.

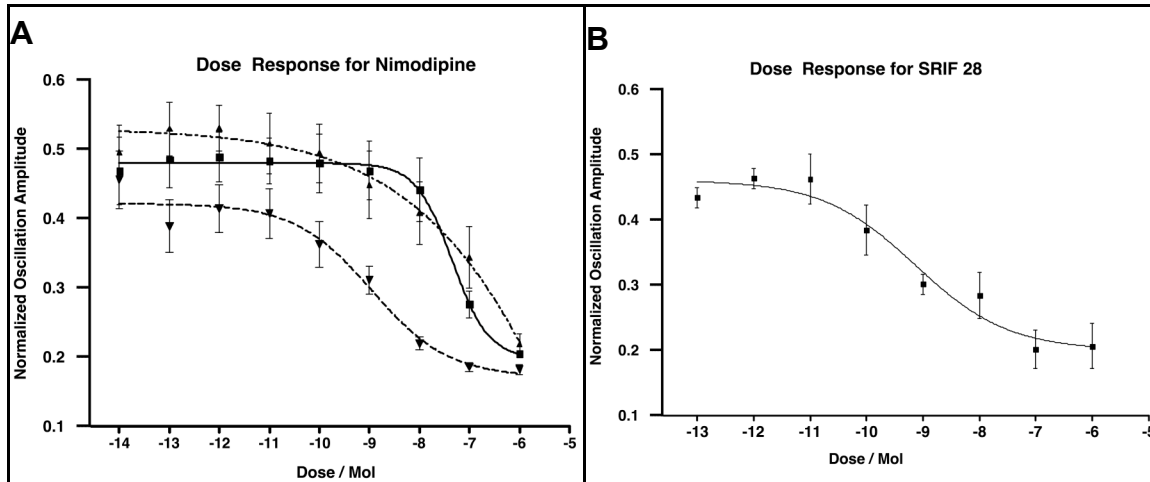


**Figure 25: Oscillation Dose Response for Nimodipine and SRIF 28**

A) Dose response curves from three different experiments. The oscillatory dose response can vary significantly. It is very important to grow cell under exactly defined conditions. B) a dose response curve for SRIF 28. The response occurs over a wide range of doses.

## Discussion

Our results show that oscillatory responses to nimodipine and SRIF 28 are amplitude modulated, but the characteristic irregular oscillation pattern does not change. However, the relative amplitude of oscillations over free base calcium level was attenuated significantly. This is not surprising for an l-type channel antagonist, since blocking of l-type channels causes a general decrease in calcium flux resulting in decreased amplitude of oscillations. It does not interfere with the pace maker mechanism responsible for the frequency of oscillations.

However, dose response curves of each individual cell and key parameters such as slope and  $IC_{50}$  vary significantly from cell to cell under the same experimental conditions. This is surprising, since these cells are clonal and are all grown in the same environment.

Consequently the average dose response over all tumor cells depends more on the statistical distribution of cells than on a genetically predetermined response function. The individual response characteristics set the boundaries, such as minimum and maximum dose of the response, but the average slope and  $IC_{50}$  values must derive from the sum of very disparate individual responses.

This result may have pathophysiological and therapeutic implications. A statistical shift in cell populations to cells with different regulatory characteristics could explain gradual changes in drug responses or progressive changes in degenerative disease. It has also implications for possible use of stem cells, as newly regenerated cell populations must match compatible regulatory characteristics of the original cells.

The result emphasizes the importance of examining cells individually. Deviations in statistical distribution cannot be detected with methodologies that average over the complete population. These methods are not facile to detect and characterize drugs that work only on cell subpopulations.

The oscillatory response to SRIF 28 treatment is almost identical to that of nimodipine. SRIF does not act directly on L-type channels but attenuation is indirect and part of the signaling pathway. Our experiments reveal that  $Ca^{++}$  signaling through SRIF in AtT-20 cells uses amplitude modulation entirely and does not alter overall oscillatory patterns. Frequency modulation was observed in pituitary slices as bursts. The results show that responses to somatostatin in corticotrophs is encoded in amplitude of oscillations and does not induce bursting.

Automated drug screening such as plate readers methods do not measure oscillatory modulation, but only general changes in  $Ca^{++}$  levels. The method presented here, however, measures the dynamics of oscillations and has the potential for full automation. This could enhance and support existing drug screening techniques.

## **Modeling Microtubule Organization**

Microtubules have many important functions in the cell. Dynamics and morphology were studied on various levels of detail and resolution (64,65). It describes the correlation between dynamics, function and organization.

Our model is based on these findings. It is a new attempt to develop a comprehensive model and new understanding of dynamics and morphology/geometry of microtubules.

The task was achieved by introducing three novel methods: New techniques for microtubule motion analysis, a newly developed automated particle tracking system and the application of I-system language to describe microtubule organization. The studies were compounded by immunocytochemical investigations of microtubular organization in different stages of the cell cycle.

We used *Haemaphysalis katherinae* (Baker) endosperm cells because of excellent optical properties and large microtubule arrays (up to 100  $\mu\text{m}$ ). Microtubules were studied with immunogold method on fixed preparations. Additional studies were undertaken with injected colloidal gold probes and under influence of two mitotic drugs: the phosphoric amide herbicide amiprofos-methyl (APM) and Taxol.

## **Introduction to Microtubule Cytoskeleton**

The cytoskeleton has many important functions in the cell. It provides mechanical stability, transports material and is essential for equal segregation of genetic material during cell division.

All cytoskeletal elements of the cell belong to one of three systems: microtubules (MTs), actin, or intermediate filaments. The most prominent and best studied is the microtubular system. Its elements are larger than those of the other two. Microtubule organization undergoes prominent changes during cell cycle. Biochemical properties are determined by a complex system of polymerization and depolymerization reactions and the influence of microtubule associated proteins (MAPs). Organization is determined by a wide variety of factors like MT organizing centers and other cellular components. Synergetic effects of microtubule dynamics and dynamics of other proteins such as transport with motor proteins form complex functional networks.

All MT organizing factors are interconnected and influence each other. Therefore any aspects of microtubule activity and organization depend on synergy of different processes. Motor proteins bundle microtubules, microtubules transport themselves by (sliding,) and biochemical reactions create imbalances of concentration within the cell.

It is therefore very difficult to develop model systems to consistently describe the dynamics and morphology of MT arrays.

We will apply a fractal model to describe the influence of lateral interactions to the organization of microtubules throughout the cell cycle. This approach explores the contribution of bundling to the organization of complex microtubule arrays.

A new model system has to have three very important features:

3. It should explain more phenomena than already existing models.
4. It should integrate as many observations as possible.
5. It should be as simple as possible.

The development of a comprehensive microtubular model based on fractal theory requires the combination of well-established scientific observations, which are often contradictory. Observations of morphology and dynamics of an *in vivo* system are necessary to evaluate and clarify these results.

Microtubule dynamics and organization can be studied at different levels of resolution and complexity. Resolution level spans from ultra-structural analysis in electron microscopy (EM) to studies on low magnifications in light microscopic. The complexity of dynamics reaches from interactions between single tubulin dimer molecules to interactions of large tubulin-polymers associated with MT associated proteins (MAPs) arrays with other parts of the cell. These interactions, the biochemical properties and other cellular components determine function and morphology of the microtubular system.

We selected the endosperm of *Haemanthus katherinae* (Baker) for our observations, as the cells form very large microtubule arrays. Furthermore, they are optically clear and do not have cell walls as many other plant cells.

The primary focus of this work is to develop a fractal model of MT organization and dynamics in *Haemanthus* endosperm on the level of resolution of light microscopy, but to use other levels of resolution as corroborating evidence.

### **Multidimensional Analysis**

We undertook a spatio-temporal analysis of the microtubule arrays as a first step. These observations will serve as a basis for the model input. We try to match observations to biochemical and morphological findings in other biological systems. Since most work on microtubules is based on observations of animal cells, some findings may not be directly comparable to plant microtubules. Moreover, basic mechanisms in the animal mitotic spindle and array dynamics are still unclear. Many studies were undertaken to understand isolated and limited aspects, resulting in many contradicting results. Our model should explain all general observations such as the following:

- Organization and direction of MT arrays in cells in various stages of the cell cycle and in cell fragments.
- Dynamics with which one array configuration is transformed into an other.
- Chromosome movements and non-kinetochore transport during mitosis.
- Other transport phenomena in various stages of the cell cycle.
- Observations were made both on fixed and stained cells, and *in situ* and *in vivo* without contrast agents or dyes.

A review of findings in lower than light microscopy ( = ultrastructural ) levels is essential in order to develop a unified model fitting for different systems.

## **Basic Facts about Microtubules and the Cytoskeleton**

This chapter will only describe the most basic facts about the biochemistry and dynamics of microtubules. Microtubules are very dynamic structures, which undergo constant transitions ultrastructurally as well as morphologically. These dynamics are governed by simple chemical reactions, as covalent- (i.e. polymerization) or hydrogen-bond formation. All these reactions are influenced by classical factors for reaction as temperature, pressure, osmotic values, and pH. They may also depend on the presence of elements as magnesium or calcium. Furthermore, energy driven reactions depend on ATP or GTP.

This chapter can only give a very simple view of MT properties, since they will be looked upon as separate unconnected factors. While all these factors may seem to be independent from one another, in fact they are not in the living cell. Regulative cellular processes may control the amount of ions present. Feed-back loops may create quite unexpected experimental results. Temperature may be regulated for the whole organism, or not. In turn cells adaptable to different temperature ranges may display totally different results in not temperature-controlled experiments than others.

ATP levels are maintained by energy driven processes as respiration. For these reactions apply Michaelis-Menten kinetics.

### **Biochemistry of Tubulin**

Tubulin is present in virtually all eukaryotic cells. In the brain tissue 10 to 20% of all soluble protein is tubulin. Three isoforms of tubulin are known. These are designated alpha, beta, and gamma tubulin. Alpha and beta tubulin polymerize into dimers. Different forms are generally similar enough to copolymerize, even across species boundaries.

The dimers can polymerize into polymers forming long chains of alternating alpha and beta tubulin oligomers. Tubulin turnover and polymerization properties were examined in cultured fibroblasts. The lifetime of two molecules between synthesis and degradation is about 20 hours. The tubulin dimer bond exists on average only 10 minutes. Tubulin oligomers form long chains called proto-filaments. These chains attach laterally to form sheets, or, in most cases, cylinders. The cylinder is called a microtubule. A MT composed of rings with 13 proto-filaments is most commonly found *in vivo*. Since the proto-filaments are formed from dimers with two different subunits they are polar. Each end has either an alpha or beta molecule at the end. All protofilaments form parallel lateral attachments.

The microtubules exhibit therefore polarity. This polarity has a profound influence on the dynamic properties of both ends. One end is a slow growing (minus) end, the other a faster growing (plus) end (66-68).

The polarity of existing microtubules can be determined in two ways. One is the hook decoration method (69). Tubulin in high concentrations copolymerizes into tubes along existing microtubules forming curved sheets. In a cross section they appear as hooks under the electron microscope. All hooks curve clockwise, and therefore the MT polarity can be determined. The alternative method simply measures the polymerization / depolymerization velocities of both ends to determine polarity.

## **Tubulin Polymerization**

The polymerization kinetics are influenced by factors as concentration, pressure, and temperature. *In vitro* experiments show that purified tubulin will polymerize at 37° C in the presence of Mg<sup>++</sup> and GTP. Experiments with light scattering measurements under the microscope show an initial lag phase before MTs start to polymerize, until a plateau is reached (70,71).

This is interpreted as the result of two different processes. Initially the MT has to be formed *de novo* in a process called nucleation. Addition of subunits to existing microtubules is called elongation. The kinetic barrier to nucleation in comparison to growth is much higher. Since no elongation can be performed without nucleation, there has to be a delay in polymerization, which is represented by the lag phase.

## **Treadmilling**

The ratio between unpolymerized and polymerized tubulin is constant when the plateau phase is reached. Further experiments, however, proved that microtubules are still highly dynamic. They undergo rapid disassembly and slower assembly at the same time. Their average length is constant because for every disassembling MT there is a growing one. This state is called steady state. The concentration of tubulin in this stage is called the critical concentration(67,72).

At steady state the critical concentration is linked to the average MT length. Since both ends of the MT are kinetically different it often occurs that one end is growing while the other is disassembling. This can be seen under the microscope as an apparent movement of a MT. The process is called treadmilling. Length of the MT during treadmilling changes if the assembly / disassembly processes are of different velocity(73).

## **Dynamic Instability**

When microtubules are measured in length over extended periods of time *in vivo* or in cell extracts and compared to microtubules resulting from purified tubulin their dynamics show large differences. The frequency of the transition of the MT ends between assembly / disassembly is much lower *in vivo*. Individual microtubules can grow for extended periods of time and over long distances (several  $\mu\text{m}$ ). The ratio of critical concentration to MT length is also much lower. That means microtubules are longer than expected for the same concentration at steady state. This modified kinetics is called dynamic instability (68).

Dynamic instability requires the presence of GTP. Alpha and beta tubulin molecules are able to bind GTP. But only beta tubulin is able to hydrolyze it. Experiments with non-hydrolysable analogs of GTP showed that the energy stored in GTP is not required for enhancement of polymerization. The binding of any GTP form will enhance polymerization, but hydrolysis of GTP is required for the disassembly process. Rapidly growing microtubules have a cap of GTP, which protects them against disassembly. As soon as that cap is lost and the GTP is hydrolyzed, microtubules start to disassemble (74,75).

EM analysis of the ends revealed a different morphology for growing and shrinking ends. Growing ends have a sharp edge at the end of the hollow tube, whereas at the shrinking end proto-filaments fan out to form small hooks (76).

### **Microtubule Associated Proteins**

Microtubule associated proteins (MAPs) modify the biochemical and mechanical properties and add new functionality to microtubules. There are many kinds of MAPs, and still new MAPs are being discovered. MAPs are being divided into two major classes:

1. High molecular weight proteins (HMW) have a molecular weight of 200 to 300 kDa and more, and they include MAP-1 and MAP-2.
2. Tau-proteins have a molecular weight of 55 - 62 kDa. Functionally, these MAPs have been divided into several classes as well.

### **Motor Proteins**

Motor proteins generate force along cytoskeletal fibers which is used to transport vesicles and other cellular structures. It enables otherwise static cytoskeletal elements to slide along each other. The addition of motor proteins *in vitro* adds the ability of microtubules to slide on the glass surface of microscopic slides, if they were coated with cellular extracts.

A second important and often overlooked function is that of bundling. Motorproteins have been shown to interconnect microtubules in a permanent fashion. All these functions require the hydrolysis of ATP. Two classes of MT dependent motors were identified, kinesin and cytoplasmic dynein (77-79).

Dyneins are involved both in mitosis and organelle transport. They are responsible for the motility of cilia and flagella. Dyneins are a minus end directed motor, which means that they translocate in the minus end direction of the MT. They consist of two light and two heavy chains with two heads attached (80).

Kinesins are more diverse than dyneins. They are involved in motility of organelles, mitosis, meiosis, and the transport of synaptic vesicles in axons. Kinesins are composed of several light chains and two heavy chains with two heads. They are MT plus end directed motors (81,82).

### **Terminology of Microtubule Arrays**

Microtubules form very different arrays during the cell cycle. These arrays are also used to determine the stage of cell cycle.

In interphase microtubules radiate from the microtubule organizing center (MTOC), which is close to the nucleus, towards the periphery. We distinguish nuclear microtubules, which are bound to the nucleus, from free microtubules, which are not bound anywhere (83,84).

Before mitosis starts, a narrow bundle of microtubules is being formed. It is situated just beneath the plasma membrane. This array is called preprophase band, and it disappears during mitosis.

The mitotic spindle is being formed during mitosis. This is first a bipolar array with two polar regions. The polar regions are formed by centrioles in animal cells. Spindle



microtubules radiate from the centriole to the middle of the spindle where they meet microtubules from the other pole. Other microtubules form the aster. This is an array of microtubules radiating from the polar region to the cell periphery. This array exists in this pronounced form in animal cells only (85).

During mitosis each half of the spindle containing one spindle pole is called the half spindle. When chromosomes move to the pole, microtubules between the two groups of chromosomes start to form the interzonal region (interzone) during anaphase. A microtubule bundling mechanism later forms a ring like structure in the middle of the cell. This is called midbody in animal cells, and phragmoplast in plant cells.

MT arrays are so complex, because they are formed by different types of microtubules. The definitions and distinction is based on morphology and / or functionality. The mitotic spindle has three types of microtubule fibers:

1. Astral fibers originate at the pole and radiate out of the spindle into the periphery. Their peripheric end may be connected to a membrane (86,87).
2. Polar fibers originate at the pole and run to the metaphase plate or cell plate / mid body. They often interdigitate with polar fiber originating on the opposite pole. Interdigitating fibers are sometimes called interdigitating MTs (66).
3. Kinetochore fibers originate at the poles as well, but terminate at the kinetochores. Each kinetochore is attached to exactly one fiber. Kinetochore fibers shorten during anaphase (87).

### **Differences of Animal vs. Plant Tubulin**

There are some profound differences in the biochemical as well as organizational properties of plant and animal microtubules:

- MAPs have different binding sites.
- Plant MAPs do not attach to animal MAPs, and animal MAPs do not bind to plant MAPs .
- The binding site of plant MAPs is not yet known.

It is possible to polymerize and depolymerize animal tubulin in many cycles with the help of Taxol and colchicine, or colcemid. This is not possible with plant tubulin. As soon as plant tubulin is polymerized *ex vivo*, it proved to be impossible to depolymerize it. As a result there are some pharmacological differences as well. Colchicine works only on animal microtubules. Some herbicides and APM in contrast are only effective on plant tubulins.

During mitosis there are some major differences in spindle organization. Animal spindles generally have asters. Asters are microtubule arrays where microtubules radiate from the centrosome, or a MTOC, away from the spindle towards the cell membrane.

Plant cells do not have well defined centrosomes. Therefore they generally do not contain astral arrays.

However, all basic processes such as assembly / disassembly kinetics, interaction with MAPs and motor proteins are very similar.

### **Microtubule Dynamics**

A classic analysis on microtubules was performed by Hotani (73). Dynamics of individual microtubules *in vitro* were observed by darkfield microscopy. Tubulin was purified from calf brain and used in polymerization experiments. Microtubules were shown to alternate frequently between growing and shortening states. With the addition of MAPs this dynamic instability could be completely suppressed. These stabilized microtubules exhibited treadmilling instead. In steady state microtubules showed treadmilling with a rate of 0.9  $\mu\text{m}/\text{min}$ . MAPs were an essential prerequisite for treadmilling experiments. These results are evidence for the important influence of MAPs on MT dynamics. By binding to specific sites MAPs stabilize inter-tubulin bindings.

Dynamic instability *in vivo* was observed at cellular edges of newt epithelial lung cells (88). Individual microtubules were observed with video-enhanced Nomarski contrast (VDIC). Series of micrographs showed the concurrent rapid shortening and slower growth of individual microtubules. MT elongation reached  $7.2 \pm 0.3 \mu\text{m}/\text{min}$  and a disassembly of  $17.3 \pm 0.7 \mu\text{m}/\text{min}$ . About 70% of all rapidly shortening microtubules were rescued. A portion of microtubules was observed to be stable over 10-15 min.

Microtubule dynamics are difficult to study, because they depend on a variety of factors. These variations were studied by Belmont (89). Changes of microtubule dynamics during the cell cycle were studied on *Xenopus laevis* eggs with rhodamin-labeled tubulin and video microscopy. Unfertilized eggs were released from meiotic arrest by electrical activation. Extracts were made from these cells, and cycloheximide was added to prevent cyclin synthesis. To study the effects of cyclin, *E. coli* expressed cyclin D 90 protein was added. Microtubules were nucleated by addition of centrosomes. Quantitative analysis revealed that rates of polymerization of microtubules are similar in interphase and mitosis, but rates of transition from growing to shrinking increased during mitosis.

MT assembly requires GTP. The question where the binding energy is stored was partly answered by Caplow (90). Standard free energy for hydrolysis of the GTP analog GMPCPP was found to be only -0.9 kcal in tubulin subunits in microtubules, as compared to -5.18 kcal in solution and -3.79 kcal in tubulin dimers. The energy is stored in the MT lattice. MT dynamics were analyzed with video microscopy. Microtubules assembled in this assay showed lateral association as well as curvatures and loops, indicating that both are intrinsic properties of microtubules.

Hyperflexible regions are an additional dynamic property of MTs (91). MTs were grown *in vitro*, and their fragile ends were stabilized by axonemal structures. End stabilized microtubules were stable over several hours. Disassembly conditions induced hyperflexible regions in microtubules visualized with VDIC. Hyperflexible regions exhibit a characteristic sinusoidal pattern. Microtubules frequently broke into two at the area where hyperflexible regions formed, and the fragments disassembled rapidly. The ends of disassembling microtubules often exhibited hooks. The average disassembly rate was found to be 1400 subunits/s, corresponding to 46  $\mu\text{m}/\text{min}$ . If buffer containing 0.5 mg/ml

tubulin and 1 mM GTP was added, hyperflexible regions could be stabilized, thereby restoring their linear geometry. GTP alone was not sufficient to stabilize these regions. In EM studies stabilized regions showed ribbon like structures.

The morphology of dynamic microtubule ends was analyzed for ultrastructural differences (74) in a timed cryoelectron microscopic study. Growing microtubules under standard assembly conditions were found to have blunt ends. Others showed short protrusions comparable to a skew cut end. These protrusions were up to 50 nm long. Microtubules shrinking under different conditions showed coiled protofilament ends. Single protofilaments were found to form spirals with addition of  $Mg^{2+}$ .

There are not only differences of MT ends, but microtubules change properties during their lifetime, as a study of McBeath showed (84). Newly formed non-steady state microtubules had different kinetic properties than older microtubules formed under steady state. These observations were made on LT-cells from goldfish. MTs detaching from MTOCs under different assembly conditions. Newly polymerized MTs were found to detach faster from MTOCs than older ones when the cells were rapidly chilled to  $-3^{\circ}C$ . When the temperature was quickly raised to room temperature the number of new microtubules nucleated at the MTOC was higher than ion steady state would predict. The overall number, however, was reduced by microtubules detaching from the MTOC. Microtubule dynamics of PtK epithelial cells and CHO fibroblasts were compared. MTs in lamellae of epithelial cells underwent characteristic short episodes of shortening and elongation with no overall change in length. Microtubule transitions in fibroblasts in contrast are longer lasting and resulted in changes in MT organization. These measurements were the first to directly demonstrate dynamic differences in microtubules *in vivo* in different cell types.

Unusual properties of MTs were analyzed by Sammak (92). Dynamics of single microtubules *in vitro* and *in vivo* were observed with x-rhodamin labeled tubulin, a SIT camera, and digital image processing. Experiments showed that one and the same microtubule could undergo several rounds of elongation and shrinking in the tampered mode. In addition, some microtubules were observed to undergo substantial lateral movements.

Microtubule dynamics were studied in cytoplasmic extracts obtained from *Xenopus* egg extracts without the addition of tubulin or buffers (93). Visualization was performed with video enhanced DIC. Eggs were cleared through high speed centrifugation to remove all refractile particles. In these non-diluted egg extracts MTs were found to be very stable. Addition of cyclin B / p34cdc2 kinase as well as mitogen-activated protein (MAP) did not disrupt microtubules. In this study MTs were observed to grow with  $17 \mu m/min$  in interphase and  $10 \mu m/min$  during metaphase. In addition microtubules assembled in interphase were less sensitive to dilution. Ocadaic acid had no effect on microtubule catastrophe events in either interphase or metaphase.

BY-2 protoplasts from *Nicotiana tabaccum* were used to study reorientation of cortical microtubule arrays in cellular development (94). These cells have characteristically organized cortical MT arrays. Enzymatic cell wall removal disorganizes these arrays, as does cooling. Reculturing cell walls causes the microtubules to reorganize again. Rewarming has a similar effect. To further test for possible mechanisms for reorganization,

respiratory inhibitors were added upon onset of the reorganization process (1 mM sodium acide / sodium cyanide). While not reducing the number of regrowing microtubules they had a profound effect on microtubules organization. This effect was reversible, as removal of the inhibitors allowed MT reorganization. Results showed no influence of 50 to 100 mM cytoschalasin D, excluding involvement of actin and actin related transport. Taxol stabilized microtubules were still capable of rapid reorientation, indicating that dynamic instability has no influence on MT reorganization.

Cells contain populations of microtubules with different dynamic properties (95). Microtubules were analyzed for dynamics *in vivo* in African green monkey kidney BSC-1 cells. Most MTs (85%) were found to have a half-life of 10 min. These MTs showed all characteristics expected from microtubules such as dynamic instability, and tempered dynamics. A second population (15%) of MTs was detected that were stable for more than 1h and had a characteristic pericentrosomal spatial arrangement.

Calcium plays an important role in the regulation and messaging of cells. Calcium influences dynamics and organization of microtubules (96). The influence of calcium on microtubule depolymerization was studied on purified tubulin prepared from fresh porcine brains. MTs were nucleated from sea urchin sperm axonemal fragments. They were assembled onto the axoneme fragments for 5 to 10 min after placement on a heated microscopy stage. MTs grew between 2 to 10  $\mu\text{m}$  in length during that time. At  $\text{Ca}^{++}$  concentrations below 2.4 mg/ml microtubule growth only occurred when axoneme fragments were attached to the inner coverslip. At concentrations of 1.2 to 1.4 mM/ml  $\text{Ca}^{++}$  microtubules appeared within 1 to 3 min with a growth rate of 1-2  $\mu\text{m}/\text{min}$ . Lowering calcium to 0.5 mM caused a rapid start of disassembly of all MTs (within 10s - 15 s). Number of microtubules was counted in 1 min intervals. The mean time to catastrophe was about 90s as calculated from a Poisson distribution fit. Dynamics were observed on MT growing (or shrinking) from axonemes by DIC video microscopy. The addition of GTP did not change the dynamics of disassembly. The rate of shortening was observed to be 180  $\mu\text{m}/\text{min}$ .

The addition of MAPs at a pH of 6.9 caused microtubules to show an important pattern for growth:

1. Steady elongation with few catastrophes for 5 to 10 min.
2. High rate of catastrophe with rescue after a defined and consistent distance.
3. After 20 to 30 min a stable state with no visible dynamics was reached.

These microtubules were no longer susceptible to low calcium concentrations. MAPs attached to microtubules at pH 7.1 gave a 50% lower yield, but with much larger length (>20 $\mu\text{m}$ ). These microtubules remained sensitive to lower calcium concentrations. In general, MAP decorated microtubules were more resistant to disassembly.

Nucleation is a key event for understanding MT dynamics. Microtubules were shown to nucleate new microtubules (97). Stable and dynamic microtubules can be distinguished by measuring the tyrosinated alpha-tubulin content in axons. Immunoelectron microscopy shows labile polymers to be densely stained, while stable polymers do not stain with anti-tyrosinated- $\alpha$ -tubulin (YL 1/2) antibody. Cells were treated for 6 hours with nocodazole to

disassemble all labile microtubules and shorten stable ones. Removal of the drug caused immediate repolymerization followed by fixation after different periods of time. Serial sections were analyzed with immunoelectron microscopy. Additional studies were done with rat sympathetic neurons grown as a dissociated neuron culture for immunofluorescence analysis. Anti beta tubulin antibody was used to stain total polymer and YL 1/2 to stain tyrosinated alpha tubulin. Nocodazole treated cells did not stain for the tyrosinated tubulin. During recovery, assembly of tubulin was observed in discrete segments.

Microtubules also undergo very fast movements (98). Bundles of native microtubules were isolated from hemipteran insect ovarioles. These arrays exhibit shimmering in darkfield microscopy. This MT movement can even blur images taken at longer exposures. High concentration of detergent, however, stopped shimmering, but it could be restored with addition of ATP. MAPs generated shimmering.

### **Microtubule Organizing Centers**

In many situations MTs emanate from morphologically distinct domains. These domains have the property to nucleate new microtubules and stabilize ends of attached ones. A major component of these centers is gamma tubulin. It was first discovered genetically in *Aspergillus nidulans* (99). Gamma tubulin genes are much more highly conserved than those of other tubulins.

Gamma tubulin is localized in MTOCs in many different organisms, but specifically concentrated at the pericentriolar material. Direct interactions with other tubulin dimers were found, especially in the nucleation pathway. Injection of anti gamma tubulin antibodies did not depolymerize existing microtubules, but prevented nucleation of new ones.

Other proteins like DMAP 60 and chaperonin were shown to interact with gamma tubulin (100). These proteins may play a role in MT regulation / nucleation activities. Spindle pole bodies in *Saccharomyces pombe* permanently contain gamma tubulin, but nucleation activity is only present during mitosis.

Another important protein for the centrosomal complex is pericentrin (101). It is recognized by autoantibodies staining chromosomes. A genetic analysis predicts a 218 kDa protein with extensive alpha-helical coil-coil domains. The flanking termini, however, are non-helical. Anti-pericentrin injected into mouse oocytes prevents normal spindle function and the formation of normal acentriolar polar bodies. In *Xenopus* eggs interphase MT arrays are disrupted as well.

The function and structure of the centromere has been reviewed by Schueler (102). Centromeres are highly specialized regions on the chromosome. Pericentrin over-expression disorganizes spindles and thus mispositions chromosomes.. The centromere has a double function. It serves as a scaffold for assembly for kinetochore components and delineates the DNA region for the attachment of the segregation apparatus. The kinetochore contains motor proteins, which are responsible for transport and microtubule attachment. Especially dynein was found to concentrate around the constriction. The DNA regions identified as being part of the constriction are called CEN fragments, and they are characterized by repeat sequences.

## **Structure and Function of the Kinetochore**

*In vitro* properties of kinetochores were observed under the microscope (75,103). Interactions of kinetochores from CHO cells with microtubules *in vitro* were analyzed in this experiment. Kinetochores were capable of nucleating new microtubules of both polarities. Vincristine treated kinetochores were found to be unable to nucleate new microtubules, while colcemid treated kinetochores retained that property, and unpolymerized tubulin could be located at these kinetochores. Preformed MTs became tightly bound to the kinetochore. This property is called MT capture. Polymerization at the kinetochore side onto already existing microtubules could be shown, too. The kinetochore was also able to translocate microtubules *in vitro*. Kinetochore microtubule bundles are often disconnected from centrosomes during formation of the metaphase spindle (77).

## **Microtubule Motors as Organizing Factors**

Hirokawa's studies revealed the influence of MAPs on MT organization. Transfection of MAP cDNA into fibroblasts and subsequent analysis with caged fluorescein-labeled tubulin and photoactivation allowed to study the effects of MAPs on MTs (104). MAP2 formed long crossbridges of about 40 nm size between microtubules. Tau protein created shorter crossbridges about 20 nm wide. MAP1B, and particularly its phosphorylated form, was found in the center of growth cones in neurons. Anti-sense MAP2 protein, however, inhibited MT outgrowth in neurons.

Similar observations were reported by Chang-Jie (105). A 65 kDa plant MAP isolated from BY-2 cells showed very diverse staining patterns. No traces of the protein could be found in the preprophase band. It colocalized strongly with spindle microtubules during metaphase, but later it localized nearly exclusively in the phragmoplast. In EM ultrastructural analysis, extended cross bridging of microtubules was found, and MTs also appeared to be wavy. Furthermore, the protein caused microtubules to organize into highly parallel arrays.

The *Drosophila ncd*-gene known for its role in chromosome segregation was found to be a MT minus end directed motor (81). The motor protein also had MT bundling capability: It showed as regular spaced projections in EM micrographs of MT bundles.

Another MT bundling study was performed by Umeyama (106). A cDNA cloned MAP2C protein was used to study MT bundling properties. Although the protein decorated microtubules evenly, it formed bundles with a pointed tip. Photobleaching studies indicated that MT turnover in these bundles was strongly suppressed. But injected tubulin provided evidence for a rapid turnover of tubulin, which could not be explained by dynamic instability. Newly formed microtubules were observed to attach to already existing bundles.

Microtubules were even shown to change shape under the influence of motor proteins (107). Microtubules were subjected to a motility assay under video enhanced microscopy and analysis. The study describes that 22S and 14S dyneins have distinct differences in the motile properties of MTs. 14S dyneins caused microtubules to bend during translocation, which was caused by the torque generating properties of dyneins.

## Transport Function of Motor Proteins

Motor proteins have diverse functions and properties, but since they are well below the resolution of the normal light microscope, dynamics are difficult to study.

A different view of MT motors in meiosis and mitosis was expressed by Sawin (108). In their view the spindle is not a cellular organelle, but rather a transient dynamic state of the cytoplasm. Motor proteins are the key components to provide transport with kinesins involved in chromosomal transport. They may also play a crucial role in MT poleward flux, which is exhibited as a polarized movement of microtubules and vesicles.

Different motor proteins are able to organize microtubules. Different modes of MT minus end organization were found: (A) The motor proteins travel along the MTs and accumulate at the minus end. Multivalent binding properties cross-connect microtubules at this end, forming an astral MT array. (B) Motor proteins cross bridge MT throughout the spindle. (C) Plus end directed motors are at the spindle pole. Motors are cross linked to a filament network which in turn connects to the centrosomal material. MTs released from the nucleation site are captured by this network and form an astral array.

The first to observe single kinesin molecules at work was Howard (109). Single kinesin molecules were shown to dislocate microtubules *in vitro* over distances of several micrometers. Single MTs were visualized with darkfield microscopy and a SIT video camera. Distances traveled were measured by means of video analysis.

As the kinetochore is the primary attachment site for microtubules during mitosis, it was always suspected that motor proteins would play a role in chromosome translocation. In fact, assays for MT motors revealed two motor proteins of opposite polarity on kinetochores (110). The minus end directed motor moved with a velocity of  $28 \pm 0.4 \mu\text{m}/\text{min}$ . The plus end directed motor moved only with  $2.9 \pm 15 \mu\text{m}/\text{min}$ .

## Chromosome movement during mitosis

Two main hypotheses exist how chromosomes separate during spindle formation and anaphase B (111). Either they are pushed apart by microtubules growing at the spindle poles that interact with the microtubules from the opposite pole by sliding apart. The other hypothesis is that poles are pulled apart by astral fibers. In contrast to these findings, laser microbeam irradiation experiments in the fungus *Fusarium solani* show evidence that a pulling force acts on the poles. When the interzonal region is irradiated with the cutting beam, poles move apart rapidly.

Newer findings question these findings, since not all experiments can be explained by the above mechanisms. Adames and Forer discovered a new force moving chromosomes during anaphase (112). They studied the movement of chromosomes and their arms in crane-fly spermatocytes *Nephrotoma suturalis* (Loew) after UV irradiation of spindle fibers. Spermatocytes were mounted on quartz coverslips. Kinetochore fibers were irradiated with UV of either 290 or 295 nm wavelength. Doses of 0.187 to 3.4 ergs/mm<sup>2</sup> were applied to the cells. A rotational movement of the chromosome arms was observed after the treatment, and angular velocities of chromosome arms were measured. Irradiation caused partner half-bivalents to stop their movement between 2 to 12 min. Chromosome arms, however, were observed to continue poleward movement independently during that time.

In one experiment 6 chromosomes stopped moving, and all associated arms continued with their poleward movement. This independent movement was even observed in chromosome arms of the half-bivalents not connected to the irradiated spindle fiber, i.e. both partner half-bivalents behaved the same, although only one half spindle was irradiated. In rare cases this poleward arm movement could be observed without irradiation. No effect could be observed, however, when the irradiation site was outside the spindle (e.g. in the cytoplasm). Irradiation of the interzone also caused poleward arm movement in some cases. The arm movement started immediately after irradiation without any delay.

Several authors found oscillatory chromosome movements. Bajer and Molè-Bajer describe these movements in detail (113). Oscillations of chromosomes in mono- and bipolar mitotic spindles were observed in primary cultures of lung epithelia cells from the Oregon newt *Taricha granulosa*. Chromosomes oscillated along the spindle axis throughout all stages of mitosis. These oscillations were even observed in monopolar spindles, and kinetochore paths could be recorded for a period of 10 min. Chromosomes migrated mainly along the long axis of microtubules. The movement did not seem to be coordinated, i.e. chromosomes moved independently of each other. Besides this movement, small clock- and counter-clockwise rotations of chromosomes could be observed.

### **Morphology and Function of the Centrosome**

The centrosome plays a central role in mitosis. It is the point where chromosomes congress during anaphase and it is the site of MT attachment. The function of the centrosome was studied by Thompson-Coffe (114). 4D2, a monoclonal antibody raised against a centrosomal isolate, was used to study the effects of centrosomal material on MTs and the mitotic spindle. The distribution of 4D2 varies throughout the cell cycle in sea urchin eggs. In unfertilized eggs the antigen shows a scattered pattern. Immediately after fertilization most antigen was found near the male pronucleus. 15 min after insemination most antigen located at the centrosome and remained there during the cell cycle.

Recovery experiments after cold treatment demonstrated the dynamics of centrosome recovery. 16 to 20 h cold treatment causes a collapse of the polar centrosome into a single mass. However, a faint microtubule stain remains which is associated with the centrosomal particle. Within one minute of rewarming, microtubules start to form a centrosome-associated monaster, while the chromatin remains condensed. Thirty minutes after rewarming a complete barrel-shaped mitotic spindle was reformed which was capable to separate chromosomes. Centrosomes were separated and formed flattened polar plates. MTs were also shown to be disordered immediately after renucleation, in contrast to fully functional monasters. Video microscopy analysis documented the loss of a mitotic spindle after prolonged cold treatment. The number of centrosomal particles found in that stage influenced the spindle reorganization after recovery. Cells forming a single particle later divided normally, while multipolar spindles were formed by those cells which contained more than one centrosomal mass.



## **Microtubule Self-Nucleation**

MT self-nucleation establishes an isotropy of MT polarities in neurons, since the nucleation process only works on either plus or minus end (115). Establishment of MT polarity was studied by observation of axonal growth of rat sympathetic neurons in the presence of vinblastine. 16 nM vinblastine was observed to act as kinetic stabilizers, while 50 nM acted as MT disassembling drug. MT polarity analysis showed that microtubules within vinblastine treated axons did not differ from untreated cells in respect to uniform plus-end-distal distribution. Morphology of axons treated with 0, 16, 50, and 100 nM vinblastine were compared with video microscopy. In control cultures outgrowth was observed to be extensive and to form dense networks. In vinblastine controls outgrowth was observed as well, but far less dense, and less elaborate. Also the volume of the cell body decreased with rising levels of vinblastine. Electron microscopy analysis revealed that microtubules progressively get denser in axons while a corresponding decrease in density could be observed in the cell body. Additional experiments showed that these microtubules were translocated with leading plus end, thus establishing polarity.

## **Structure and Dynamics of the Mitotic Spindle**

Two different types of spindle fibers were found in the meiotic spindle of *Drosophila melanogaster* (116). One type connects the kinetochores to the centrosomes. The other fiber type runs from the spindle poles to the equator and was described to form cup shaped hemispheres. These fibers remain part of the spindle until cytokinesis. Antigens otherwise associated with centrosomes were found as dispersed particles surrounding the nuclei at cytokinesis.

A quantitative analysis of spindle microtubules was performed by Jensen (117). EM micrographs and serial reconstructions allowed him to quantify the number of MTs in the spindle of *Haemaphysalis katherinae*. Kinetochores as well as non-kinetochore fibers were found to intermingle. Prometaphase chromosomes had large numbers of non-kinetochore microtubules attached to the chromosome. The number of kinetochore MTs ranged from 79 to 109 at metaphase. This was the largest number of k-fiber microtubules ever found to attach to a kinetochore. Throughout anaphase and telophase these numbers decreased progressively. The divergence of angles of microtubules from the spindle axis also increased during the course of mitosis represented by increasing numbers of oblique microtubules. The average divergence angle rose from  $13.5^\circ$  to  $56^\circ$  in telophase. The divergence angle was dependent of their distance from the polar region and independent from the stage of cell division, as evident on chromosomes that were delayed in their poleward movement. The number of MTs on delayed kinetochores was found to be higher. C-shaped proximal terminations of MTs were highest at early prometaphase and disappeared during midanaphase.

The relation of k-fiber microtubules vs. non-k-fiber microtubules was analyzed by McDonald (81). Metaphase microtubules in EM serial sections of PtK cells were digitized and a 3-D reconstruction was made. The kinetochore fibers were shown to consist of a network of interconnected kinetochore and non-kinetochore MTs. Many fibers ran oblique to the spindle or fiber axis. A vector analysis showed that kinetochore MTs run mostly

parallel to each other, with little deviation from the fiber axis. Non-kinetochore fibers, however, showed a random deviation with no preference of any direction.

Other MT dynamics were observed by Bastmeyer (83). The fine structure analysis of crane fly spermatocytes with Allen Video Enhanced Contrast DIC (AVEC-DIC) showed that the spindle was formed by a number of fibrils, each consisting of several microtubules. These fibrils were oriented parallel to the long axis of the spindle between the poles. Slight tilting of microtubule arrowhead-like-structures could be observed. These structures turned out to be points of intersections of microtubule bundles. An overall lattice like formation of MT was shown, and the fibrils displayed flickering during mitosis, thus indicating rapid turnover and reorganization.

### **Microtubule Self-Organization**

Cell fragments of *Haemaphysalis katherinae* endosperm were extensively used to observe the formation of MT arrays (113). First, MT converging centers were formed which then transformed into mitotic spindles and phragmoplast like structures. These arrays formed spontaneously, without the influence of any additional drugs. This self-organizing process was observed in many different fragments free from nuclei (118,119). Irregular meshes were formed in large cytoplasts few minutes after preparation. 20 min after preparation MT converging centers could be observed. MTs were found to form pointed arrays with a pointed tip and diverging microtubules on the other end. These arrays were often curved and formed spiral-like-structures (Figure 33).

MT motor proteins and MAPs have an influence on organization as demonstrated with tau (120). Randomly oriented microtubules were bundled even with a fragment of the tau-protein. This type of bundling increased microtubule growth about 30%, stabilized microtubules against cold and dilution induced disassembly, and increased nucleation rate. The binding site is different from the normal MT binding domain as was evident with this truncated protein which contained mainly the repeat domain of tau, but lacked amino- and carboxyl-terminal sequences.

Other mechanisms in MT self-organization seem to be involved (121). MT arrays were formed by hexylene glycol or taxol in unfertilized eggs of sea urchin *Lytechinus pictus*. The organization of microtubule arrays was dependent on acidity. Cells at pH 8.5 formed multipolar spindles and even completed multipolar divisions. Temperatures slightly above 22°C induced the formation of MT bundles within 30 min. In subsequent stages these transformed into fan-shaped structures and spirals. EM micrographs showed a number of dense spheres in the center of MT congression.

Many proteins were found to be involved in spontaneous MT organization. Motor proteins, for instance, bundle microtubules. Another non motor protein was found to interact with microtubules (122): A protein reacting with human autoantibody SP-H, which immunostained mitotic poles, was analyzed for its role in mitosis. The polypeptide had a mass of 200 to 230 kDa depending on the line of cultured cells. After nuclear envelope breakdown the protein was found to locate at the proximal end of MT bundles with microtubule minus ends pointing toward the cell periphery. These bundles were further evolved into fan like shapes. SP-H always located at the MT minus ends. The protein was

insensitive for ATP extraction, but sensitive for NaCl.

Disruption of the light chain of cytoplasmic dynein disrupts the organization of MTs in metaphase (123). A mechanism that involves contributions from both centrosomes and structural and microtubule motor proteins focuses microtubule minus ends into spindle poles.

Sarcomeric actin and myosin participate directly in the organization of thick and thin filaments into sarcomeres as observed by time-lapse confocal microscopy (124). Protein gradients can arise over distances of tens of microns around supramolecular structures from mixtures of soluble molecules. Furthermore, mitotic spindle morphogenesis is influenced by protein gradients around chromatin (125).

### **Dynamics of the Kinetochore Fiber**

Experiments to elucidate the dynamics of the kinetochore fiber usually involve either mechanical or biochemical interaction with MTs, or their attachment points on chromosomes or centrosomes. Kinetochore fiber dynamics of crane fly spermatocytes and newt epithelial spindles were analyzed with UV microbeam irradiation (126). UV microbeam irradiation creates areas of reduced birefringence (ARBs). Actually, the fiber is cut into two stubs by the microbeam with one stub being attached to the kinetochore and the other to the spindle pole. The spindle pole stub was observed to disassemble rapidly, while the kinetochore stub remained visible for extended periods of time. It changed orientation, sub fibers diverged and started to elongate. The divergence angle reached up to 30 degrees. MTs at the elongating end were observed to wobble, i.e. change their orientation rapidly. Individual fibers also showed bending when encountering mechanical obstacles. Vesicles moved along the fibers to the tip and remained there. In total, three types of response were observed after irradiation during metaphase.

Mechanical influence was studied by Ault (127). Arrangements and tension of MTs during mitosis was examined in grasshopper spermatocytes of *Melanoplus differentialis* (Thomas) and *Melanoplus sanguinipes* (Fabricius). Chromosomes and associated MTs were put under tension by micromanipulation with a glass micro-needle. Cells were chemically fixed while displaced bivalents were held under tension. As a result, most kinetochore fiber MTs were shown to run parallel from the chromosome to the pole. Other chromosomes were released after fixation for several minutes. These started to move immediately toward the poles.

In other experiments chromosomes were rotated so that kinetochores did not face the pole anymore. The kinetochore then reattaches by turning away from the facing pole and actively moves towards the opposite pole. This reorientation was achieved by microtubules forming a connection to the opposite pole. Unstably oriented kinetochores were observed to rotate until finally a stable orientation was reached. This coincides with MTs running to both poles during reorientation. Properly oriented kinetochores showed only mono-oriented kinetochore fiber MTs. Mono-orientation clearly stabilized the kinetochore rotation to one pole.

The organization of the kinetochore fiber during prometaphase was directly observed with video microscopy (128). After breakdown of the nuclear envelope, formation of k-fiber

MTs was observed for each of the four subunits of the kinetochore. The fibers were found to form asynchronously for each of the subunits. Each subunit on the chromosome first formed its own separate fiber, which later fused into one continuous k-fiber. These observations were confirmed by low temperature experiments (6 to 7°C). Small but thick MT bundles were observed to emanate from each kinetochore subunit.

Ptk1 cells were used for fluorescence redistribution after photobleaching (FRAP) experiments (88). Cells were microinjected with fluorescently labeled tubulin and cooled to disassemble non-kinetochore fibers. FRAP showed that 72% of tubulin is exchanged with the cellular tubulin pool within a half time of 77s. Poleward flux of subunits could not be observed under low temperature condition. In a second study high-resolution polarization microscopy was used to observe MT dynamics in newt epithelial lung cells. 150 nm thick optical sections showed microtubules organizing into small bundles called rods. These associations were found to be transient. The rods caused clustering of non-kinetochore and kinetochore fibers to form the chromosomal fiber.

A combined pharmacological and labeling study pointed to the kinetochore as a site of MT subunit loss (129). Nocodazole caused MT subunit dissociation during prometaphase, and disassembly was pinpointed at the kinetochore. 17 mM nocodazole stopped MT assembly in newt epithelial lung cells. Spindle poles started to move towards the metaphase plate at a rate of  $3.6 \pm 0.4 \mu\text{m}/\text{min}$ . Nonkinetochore MTs disassembled rapidly after 60 to 90 s of nocodazole treatment. 5-(4,6-dichlorotriazin-2-yl)amino fluorescein (DTAF) labeled tubulin was microinjected and used for FRAP experiments. There was no visible decrease of distance between the bleached area and the poles, only the distance between kinetochores and the bleached region shortened.

*Haemaphysalis* k-fiber dynamics were observed by Czaban (130). In endosperm cells UV microbeam irradiation with polarizing microscopy was used to investigate the dynamics of k-fiber MTs. Kinetochore MTs located poleward of the irradiated area were found to be unstable and to shorten at a rate of  $40 \mu\text{m}/\text{min}$  or more. Chromosome attached MTs, however, were stable and started to grow after about 80s at a rate of  $0.7 \mu\text{m}/\text{min}$ .

A microinjection study revealed the site of tubulin incorporation in growing MTs (131). Paramecium ciliary tubulin in conjunction with microinjection was used to study MT dynamics in PtK 2 cells which were fixed after different periods after injection. Sites of incorporation were localized with a specific antibody not reacting with vertebrate tubulin.

Immunogold stained cells were observed with nanovid microscopy and EM. In interphase MT growth of  $2.6 \mu\text{m}/\text{min}$  with new centrosomal nucleation was observed. Most cytoplasmic MTs were replaced within 30 min. During mitosis astral microtubules exhibited the same pattern of renewal, but with a complete turnover after 6 min. Incorporation of tubulin into the k-fiber was not observed in prophase and early prometaphase. Only after the k-fiber was established, incorporation at the kinetochore end could be observed.

The turnover of MTs was shown to be dependent on the phase during mitosis (132). LLC-PK cells were microinjected with x-rhodamin tubulin. Spindles in metaphase and anaphase were photobleached. Quantitative analysis with a CCD array did not reveal any

recovery in anaphase. In metaphase cells, however, 70% of all bleached microtubules recovered within 7 min.

Chromosomal movement could be correlated to k-fiber movement by another photobleaching study (87). Mitotic spindle microtubules of LLC-PK cells were photobleached to compare chromosomal movement in relation to the bleached zone which was about 1  $\mu\text{m}$  wide. Results showed that chromosomes moved into this zone. Double labeling demonstrated that bleached microtubules were not severely damaged by the bleaching process.

Another very important aspect is the ability of monopolar spindles to retain the capability to move chromosomes. This rules out several hypotheses about the mechanism of k-fiber function. In a study combining photobleaching with video microscopy no differences between mono- and bipolar spindles were found in relation to MT dynamics, the ability to push chromosomes towards the metaphase plate, and chromosome oscillations along the spindle axes (85). The number of kinetochore microtubules also did not vary, and kinetochore to pole distance was found to be equal in mono- and bipolar oriented spindles.

*In vitro* experiments revealed that poleward movement of chromosomes could be explained by microtubule depolymerization (133). Microtubule chromosome complexes were constructed for this experiment, where crosslinked biotinylated MT seeds served as nucleating structures. Varying concentrations of free tubulin could produce assembly and disassembly conditions. It was shown that disassembling microtubules could move chromosome kinetochore complexes, and that disassembly was located at or near the kinetochore.

A different study, however, showed the opposite effect (134). Injection of additional tubulin was able to push chromosomes. During anaphase PtK cells were injected with biotinylated tubulin. Analysis after 30s showed that tubulin incorporation occurred proximal to the kinetochores. After one minute labeled tubulin was found throughout the k-fiber. The injection even caused a transient reversal of chromosome movement. Incorporation of tubulin also caused MTs to move laterally during reversal, thus increasing the lateral separation of chromosomes.

An open question is the kind of MT attachment at the kinetochore. Several studies were undertaken to reveal the mechanism. Hayden (135) made direct observations. The mitotic spindle in newt pneumocytes is devoid of organelles and vesicles. This allows to record the capture of MTs. In interphase pneumocytes astral microtubules elongated at a rate of  $14.3 \pm 5.1 \mu\text{m}/\text{min}$ . Initial interaction of these growing microtubules with the kinetochore could be directly observed with VDIC microscopy. A series of micrographs demonstrated the capture of a single MT growing from the centrosome to the kinetochore.

The transduction of force through the kinetochore fiber depends on the number of MTs (136). The number of meiotic microtubules in a k-fiber in grasshopper spermatocytes was experimentally reduced with a focused microbeam. The control of irradiation intensity and the counting of surviving MTs allowed an analysis of forces acting on the chromosome per microtubule. Since the number of kinetochore fiber MTs of the opposite non-irradiated kinetochore remained constant, the balanced forces were disrupted. The poleward force

was shown to depend on the number of attached MTs. The velocity with which chromosomes moved, however, was independent of that number. The study was supported with EM analysis, and serial reconstructions confirmed the number of microtubules present in irradiated and normal kinetochore fibers.

A kinetochore fiber dynamics analysis was performed with photo-activation (137). To study the dynamics of the K-fiber, microtubules were copolymerized with caged compound tubulin and photo-activated. Marked areas moved with 0.5  $\mu\text{m}/\text{min}$  poleward during metaphase. The flux was accompanied by MT disassembly at the pole, and poleward flux decreased from early anaphase through late anaphase during mitosis. A significant loss of marked tubulin was encountered, stronger than expected by photobleaching. The marked regions also decreased in brightness during the movement.

### **Particle Translocation Studies**

Endogene as well as injected particles or vesicles can serve as motion analysis probes (138). They may colocalize with cellular structures and indicated the movement of these structures, or indicate intracellular transport. Several studies were undertaken to reveal transport mechanisms by analyzing particle motion.

Saltatory transport was observed by Beckerle (139). Microinjected 269 nm beads exhibit saltatory motions in tissue culture cells. Continuous exposure of fluorescent beads in BS-C-1 cells showed a variety of movements. Particles often followed long linear trajectories, or followed a circular path. A loss of MTs induced by mitotic drugs inhibited those saltatory particle movements. When MTs recovered, motion resumed. Filamentous actin cytoskeleton, however, was not influenced by the nocodazole treatment.

Motor proteins can mediate particle movements. But simple MT depolymerization can dislocate vesicles as well (140). Lysed and extracted *Tetrahymena* cells were used to demonstrate that depolymerizing MTs can exert a pulling force on beads. Pellicles were decorated with short MTs and fixed with EGS. These stubs elongated after addition of purified tubulin. Particles, chromosomes and their attached MTs were perfused into a chamber where MTs attached laterally. After attachment tubulin concentration was lowered. This led to a disassembly of MTs. As a consequence, the shortening MTs pulled particles toward the chromosome. They stopped to move when they reached a small stub of stable MTs attached to the kinetochore. Some particles exhibited linear movement of 16  $\mu\text{m}/\text{min}$  over distances up to 5.5  $\mu\text{m}$ . Other particles exhibited a stop and go behavior with velocities of up to 26  $\mu\text{m}/\text{min}$ . The fastest velocity measured was 80  $\mu\text{m}/\text{min}$ , the average being  $26 \pm 20 \mu\text{m}/\text{min}$ . Chromosomes also exhibited movement when their MTs were attached to a non moving target. Average velocity was  $15 \pm 12 \mu\text{m}/\text{min}$ . Both types of translocations were unaffected by 100 mM ortho-vanadate to exclude ATP hydrolysis as a source of energy.

### **Pharmacological Effects on Spindle Dynamics**

To reveal the dynamics and interactions of spindle microtubules, and ultimately the mechanism of chromosomal transport, pharmacological experiments are often the only approach giving clear cut results. Mitotic drugs are substances which change biochemistry of MTs and associated proteins. Most of the underlying mechanisms of these drugs are well

understood. Changes of k-fiber dynamics were observed under the stabilizing influence of Taxol by (141). Spindle elongation of Ptk cells was observed under the influence of taxol. When added 3 minutes after initial chromatid separation, its effect on anaphase A was minimal. With 20 mM taxol, pole-to-pole separation in anaphase B was reduced to 4 to 9.5%. Average values of pole-pole separation are  $1.0 \pm 0.25 \mu\text{m}/\text{min}$ .

Under influence of taxol a different organization of MTs was observed. MTs in the interzone were depleted, thus forming a narrow gap. Confocal analysis verified that few MTs extend between the gap and each pole. MTs appeared bundled, as judged by the increased thickness and brightness of MT fibers. Controls were made with nocodazole. This drug disassembled MTs, which results in a shortened spindle. A combination of taxol and nocodazole treatment reduced the effects of nocodazole greatly.

A taxol induced anaphase reversal was also observed and imaged in *Haemanthus katherinae* endosperm cells (142). Studies were done with concentrations where mitosis is not arrested, but slowed. Taxol caused formation of new MTs which were often laterally associated with existing ones. The resulting mitotic spindle reorganization caused chromosomes to move back towards the metaphase plate in anaphase. Taxol also led to a depletion of interzonal microtubules.

### **Special Properties of Plant Cytoskeletons**

It is well known that plant cell MTs are different in comparison to animal MTs (143). The nucleus plays an important role in MT organization. Nucleus fragments and nuclear particles are capable of associating and nucleating MTs in plants. These tubulin arrays are very similar to astral arrays of animal cells. Plant tubulin polymerizes on distal ends of already existing MTs, in contrast to mammalian tubulin.

The cell wall also influences MTs. In *Chara* interactions of the cell wall and plasma membrane are mediated by integrins. The cytoskeleton interacts with the membrane and may even have connections to extracellular matrix proteins. MAPs have been isolated which not only cross-linked microtubules, but also act as MT stabilizing agents.

The MT sliding hypothesis is based on the findings in diatoms. Especially in *Cylindrothetica fusiformis* a kinesin related protein has been found to be essential for the process. A classical study of mitosis revealed the first details of k-fiber dynamics without the help of immunocytochemistry (144). Cinematic recordings with high extinction Nomarski interference system of *Haemanthus* endosperm in mitosis showed a "beaded" pattern of the spindle fiber in objects of  $0.3 \mu\text{m}$  in diameter, or even smaller. The pattern was shown to move poleward during metaphase. On kinetochore separation, chromosomes appeared to latch on to the movement of the beaded pattern.

The dynamics of MT arrangements from prometaphase through anaphase in *Haemanthus katherinae* (Baker) endosperm were also observed *in vivo* by VDIC microscopy (145). MTs were seen to rearrange very quickly at the onset of prometaphase. After 10 to 15 minutes they formed bundles or sheets running from chromosomes to the polar regions. These structures could be observed until late anaphase. Bundles of MTs were observed to intermingle and fuse towards the polar areas. In cross sections these bundles appeared as irregular branches. The whole spindle was enveloped by a dense array of MTs, which

formed a perimeter around the spindle. This perimeter had the same lifetime as the mitotic spindle itself. MTs extended from this envelope into the spindle and intermingled with spindle MTs.

### **Intracellular Motion**

Properties of Random walks have been described mathematically (146). In vacuum a particle, regardless of its size, has a kinetic energy associated with it of  $kT/2$ ,  $k$  being the Boltzmann constant and  $T$  the absolute temperature, and the kinetic energy of the particle with mass  $m$  and velocity  $v$  is  $mv^2/2$ . Thus, the mean time square displacement equates to  $v = kT/m$ .

In an aqueous medium the particle would bump into other molecules after a short distance. If we look at the particle with discrete steps (as in video recordings), we can observe the displacement directly as little jumps, with defined velocities and time steps.

### ***Model Systems for Organization***

The principal purpose of model systems is to test hypothesis and make predictions. Model systems cannot prove a hypothesis. Basically all observations on natural systems are taken into consideration. Then the properties of all components are taken into consideration, and a hypothesis is being formed. According to Occam's razor, the hypothesis should rely on as few rules and axioms as possible. The resulting model should explain all observation on the basis of these rules.

All current models for microtubular organization were based on observations of animal microtubules. They usually do not explain the differences in plant and animal microtubules. A perfect model system must account for the differences in organization based on known properties.

Organization is any steady or transitional state of a system different from randomness, and with a well-defined set of properties.

To test for the properties and for randomness we need a set of parameters, which can be dependent or independent of each other. In the case of the cytoskeleton, the preferred parameters are spatial parameters, as they are easy to observe. Computer analysis and measurements may give hard numerical data about morphology and direct quantitation.

Organization can be described on different dimensions. The basic building block for MTs is the tubulin molecule. Since alpha and beta tubulin form dimers, this is already a simple form of organization. The ratio of free tubulin and tubulin dimers is an independent parameter that indicates the amount of polymerization, and in turn the degree of organization. Length of a microtubule and its curvature are parameters of a higher level of organization.

Population dynamics and statistical distribution of MTs is another parameter since directly linked to the microenvironment the MT is growing in. As MTs grow and shrink constantly, the turnover rate is a good measure of MT dynamics, but it is not intrinsically an organizational parameter. A faster turnover rate does not per se change the organization of MTs but only speeds up any changes.



## **Static Models**

Static models try to describe a system at one time. This is a severe limitation, since dynamic systems such as the cytoskeleton obviously are difficult to describe with static models. On the other hand they allow for a higher level of abstraction, since they only regard organizing principles. They are also much easier to compute, since each set of parameters has only one and not several solutions.

## **Dynamic Models**

Dynamic models should start both with a well-defined state and a well-defined set of parameters. Through consecutive cycles of calculations interactions are calculated. The results from each round are again fed as starting parameters into the next round. An example of a dynamic computational model is the simulation of weather conditions used to predict the weather. Here the starting set of parameters is the data from weather stations and satellites. Then, in several successive rounds, the possible changes are being calculated to get a new situation as a result, and that result is again used for another round of calculations.

The major concern with dynamic models is precision and granularity. It is impossible to acquire a complex systems state in infinite precision. Furthermore, calculations themselves only reach a limited precision.

## **Euklidian Models**

Euklidian models use euklidian space and its classical geometric shapes as a basis. The classical shapes are ellipse and polygon. These also include shapes that obtain more stringent parameters such as circles, rectangles, or squares. Rectangular arrays can be formed by parallel microtubules of the same length and the same starting point. Microtubules can be oriented either along the long or the short side of the rectangle. Although MTs cannot directly fuse with one another at a right angle, the analysis of MT arrays yielded several examples of approximations to rectangular organization. Highly parallel arrays are found in *Haemanthus* endosperm in the phragmoplast and in the kinetochore fiber, where MTs are oriented parallel to the long side of the rectangle in the kinetochore fiber. In contrast, they are oriented along the short side in the phragmoplast.

## **Fractal Models**

Fractals are quite different from other models. We try to use fractals to model the organization of microtubules because fractals are well established in describing dynamic processes and morphology in other fields. Fractals generate structures over several orders of magnification. They have characteristic features like self-similarity, describe development of processes by iterations, and can easily be calculated with modern computers. The most famous fractal is certainly Mandelbrot's set. For our purposes we concentrate on a kind of fractal called iterated function system (IFS) which were made popular by Michael Bersley:

*"Fractal geometry will make you see everything differently. [...] You risk the loss of your childhood vision of clouds, forests, galaxies, leaves, feathers, flowers, rocks, mountains,*

*torrents of water, carpets, bricks, and much else beside. Never again will your interpretation of these things be quite the same", wrote Barnsley in his book "Fractals Everywhere", and he continues:*

*"Fractal geometry is an extension of classical geometry. It can be used to make precise models of physical structures from ferns to galaxies. Fractal geometry is a new language. Once you can speak it, you can describe the shape of a cloud as precisely as an architect can describe a house. "*

We describe the morphology and geometry of the MT cytoskeleton with a fractal model in three steps:

1. Identification and description of organizational processes.
2. Formal representation of these processes.
3. Matching the model output to MT structures found *in vivo*.

We thus aim at closely matching fractal theory with observations of morphology and dynamics of microtubule cytoskeleton.

## **L-systems**

The two principal areas of Lindenmayer or L-systems include generation of fractals and modeling of plants. In 1968 Aristide Lindenmayer, a biologist, introduced the L-system fractals. They are originally a string rewriting mechanism. A string is a chain of characters. String rewriting rules determine how single characters are replaced with other chains of characters. L-systems were used to describe branching patterns of plants. By interpreting characters as "turtle graphics" commands similar to the Logo language, graphical representations can be obtained. Logo was developed by Wally Feurzeig and Seymour Papert at BBN Technologies (Cambridge, Massachusetts). An important extension to the original L-systems are bracketed L-systems. They add two symbols:

- [ Means to push the current state of the system on to a stack. Position, direction and possibly other attributes are stored.
- ] Means to pop a pushed state from the stack and to assume the stored position, direction, and attributes.

A development of this system is represented by the state each system is in at a defined step, and later steps are equal to later stages of a natural system.

In this model we use L-systems to model organization of microtubule arrays. The basic principle is to successively replace parts of an initially simple object with a set of rewriting rules. These rules are also called productions. At the start there are two shapes, an initiator and a generator. Both consist of a series of connected straight lines. In the first step the generator replaces each straight line of the initiator. Lines represent MTs or MT bundles. Successive steps in fractal generation are interpreted as successive steps in MT array organization and development.

## **Material and Methods**

This section contains the description of methods used to examine dynamics and organization of MTs and their interference with the cytoplasm and its contents. These methods rely heavily on electronic imaging as well as digital processing and image analysis. Several of these methods were especially developed and will be described in detail.

### **Specimen Preparation**

We selected two different species with unusually large cells for our studies. As a control we selected the Newt epithelial cell. The triploid *Haemaphysalis* endosperm cells are unusually large, with a diameter of around 100  $\mu\text{m}$ . Furthermore, their large chromosomes are easy to observe.

Endosperm cell are suspended in a clear fluid in the fruit body. This fluid serves as a natural physiological solution. To hold the cells in place under the microscope, two layers of GELRITE (Celco Corp.) surround the cells. One layer is attached to the cover glass. The cells are extracted by cutting the fruit open and squeezing the fluid on the coated cover glass. The second layer is then attached so that it seals the cells together with the surrounding fluid. In essence this is a modified hanging drop mounting method, with a bilayer of GELRITE serving to hold the fluid with the cells contained. The chamber is simply mounted on the microscope stage and ready for observation.

### **Video Recording**

Video images are electronic representations of images. We used a multi step acquisition and processing setup (138). First, the image is converted from light to an electrical signal. Secondly, analog and digital processors are processing this signal. The digital processor converts from an analog to a digital data stream, processes the data and reconverts it to an analog signal, which can be displayed on a monitor. The last step also requires a recording with a video tape recorder, digital video recorder, optical disk recorder, or a DVD recorder. By adding a switchboard to the in and out signal, connectors of the two cameras, and the recorders, we could loop video signal through the analog and digital processors and save them as a processed copy. Temporary storage, as a series of digital image on Image1, was possible. Hardcopy printouts were made with a Hewlett Packard Deskjet printer on glossy paper.

### **Video Systems**

Several types of video cameras were available. The selection of a proper camera is crucial for an experiment, since each camera type has its advantages and disadvantages. All camera types can be divided into intensifier, tube and chip type cameras.

All video cameras have the task of converting light into an analog electronic signal. This task requires a conversion process from light to electric current, which is achieved by a layer of photoelectric material. This layer is called the camera target. If a photon reaches the target, it may produce an electron hole pair. The charge produced is proportional to the wavelength of the photon. Over time the charges accumulate at the target.

Thus, quantity of charge is proportional to the number of photons hitting the target. If the charge is measured by equalizing them, the brightness (=number of photons) of an area on the target can be determined. There are several ways to do that, and this is where differences in camera designs lay.

### **Tube Cameras**

All tube cameras consist of a funnel shape tube, which has its target at the wide side and an electron gun on the narrow side. A deflector coil surrounds the electron gun. An electron beam is focused onto the target. The electron flow is modulated by local charges on the target created by photons. This results in a change in current of the electron beam. The difference is amplified and used to generate the video signal. The deflector magnets scan the electron beam over the target in rows. Each video frame is acquired row-by-row by scanning. The standard video signal is defined as an interlaced signal. Only every second row is read during a single sweep. Thus the whole video frame is composed of two fields whereby each field has the full horizontal, but half the vertical resolution. Fields are transmitted with twice the frequency as the full video frame.

Tube cameras have a few drawbacks. They are very sensitive to any magnetic fields, because any disturbance displaces the electron beam. Secondly the guidance system of the beam has to be very precise. A defocused beam would not hit only a small place on the target, but a wider area, resulting in a blurry image. Even small inaccuracies in the beam guidance lead to geometrical distortions in the resulting video image. Additionally the interlacing would be disturbed, and lines may be inaccurately registered.

Additional errors are introduced by excess light, which may produce an overflow of charges on the target. These charges then start spreading, depending on the neighboring charges. The resulting image error is called blooming.

Adjusting the voltage of the electron beam can regulate sensitivity of a tube camera. The higher the voltage is, the higher the sensitivity, since higher voltage leads to higher currents.

### **CCD Cameras**

The Charge Coupled Device (CCD) cameras consist basically of an array of phototransistors located on a large microchip. Therefore these cameras are also called chip cameras. Photons hitting the camera target produce electron hole pairs. The charge is then transferred to a measuring unit on the chip. Each photoelement is read out into a line register. Then each charge is shifted along the line registers. CCD cameras have very different properties in comparison to tube cameras. Unfortunately they are less sensitive, because the lines to transfer charges leave only approximately 20% of the chip area free, so that only 20% of the incoming light is being registered.

On the other hand the chip technology has many advantages. Since the photodiodes are very accurately distributed on the chip, there is no geometrical distortion. Adding a discharge switch acting as an electronic shutter controls sensitivity. All charges are discharged instantly until the switch is turned off. If the time between switching and

readout is short, the sensitivity of the camera is lowered, and an extremely short timeframe of image acquisition is achieved. Consequently motion blur can be eliminated.

Another disadvantage of the CCD chip is the dark current. Even if no photons reach the target, a small current is flowing, which is temperature dependent. To minimize it, the target can be cooled by a Peltier element. Another possibility to rise the sensitivity is to let charges accumulate on the target (slow scan). This leads to a lower readout rate, i.e. fewer pictures per time. The limit is again the dark current which discharges the elements before they are read out, if too few photons reach the target.

Blooming does exist with CCD cameras, too, but it is not as strong as with tube cameras, since photoelements are sufficiently separated from each other.

## **Signal Properties of the Video Signal**

This chapter is a short introduction of the basics in video signal encoding and transmission. Basically the video signal is an amplitude-modulated signal of the local brightness of an image. The maximum voltage is 1 Volt and the lowest 0 Volt. Therefore the ideal signal is a 1V peak-to-peak signal. Since the video frame is transmitted line by line, synchronisation signals are added. They are negative to allow for simple detection. The duration of the signal determines whether it encodes a vertical (short) or horizontal (long) retrace. After a vertical retrace a new video line is started, after a horizontal retrace a new field. As a full video frame is composed of two fields, each field contains every second line only. The interlacing of lines is used to reduce flicker in the final monitor image.

The aspect ratio of the video frame is 4:3. The video signal can be transmitted on a carrier wave, which allows for wireless transmission, i.e. television. Since the modulation and later demodulation of the carrier wave leads to additional noise, high quality video signals are directly transferred over coax wires. The coax wire reduces inductive signal loss and minimizes disturbances by other electromagnetic fields as being produced, for instance, by other monitors. The video signal has a maximum frequency of 5 MHz. The signal can therefore be reflected on wire ends and produce ghost images. Thus, a proper termination on both ends of the video connections is essential, which is achieved by a 75 Ohm resistor.

## **Multimedia**

Digital video is the newest addition to the multimedia world of computers. The principle of multi-media is to convert all information into digital information streams, hence the name. Documents, images and sound are converted into different forms ("formats") of digital information. Many new aspects arise from this technology. Digital information can be quickly reproduced with perfect fidelity, transmitted over long distances, and it is open to automated computer analysis and modification. Many new aspects like digital bandwidth, reproduction fidelity, and digital noise have to be taken into account.

## **Analog to Digital Signal Conversion**

This process is most crucial, because it can determine the success or failure of an analysis, or experiment. The key properties of an analog to digital converter are sampling rate, resolution and linearity.

The sampling rate determines how many values are converted per time. This is an important topic especially with high frequency signals common to video. A 5 MHz signal requires twice the sampling rate to compensate for aliasing. Aliasing leads to mirror frequencies. If a frequency higher than the sampling frequency is fed to the digital to analog converter, a signal with the frequency  $F = F_s - F_a$  appears. To cut all those frequencies out, the sampling rate has to be substantially higher. This holds true for all analog-to-digital conversion processes, regardless whether images or acoustic waves are digitized.

The resolution of a digitizer describes how many values it can differentiate. Since all resulting values of the digitization process are discrete, a new type of noise is introduced: the digital noise. This noise decreases with rise of resolution of the digitizer.

## **Image Processing**

Images contain an enormous wealth of information. The fast development of computers does now allow for processing on inexpensive personal computers and workstations. Image processing is present today in many areas of sciences and serves as a basis for interdisciplinary research.

Image processing serves multiple functions. It enhances structures for better visibility, prepares images for automated analysis, and protects information against image degradation. Realtime image processing is required to extract information existent only in original video frames.

Image processing can be divided into analog and digital processing. Analog processing uses classical amplification and filtering circuits to manipulate the image. Digital processing is a calculation dependent method that applies to the digital datastreams from the analog to digital converters. Digital processing is more flexible than analog processing and can replace any analog circuitry. But since digital filtering begins after digitalization, all processing required before digitalization has to be analog. The digital processor also needs a lot of computing power, since digital datastreams are quite large. Therefore either fast Arithmetic Logical Units (ALUs) have to be employed, or the digital stream has to be deferred by being temporarily stored on digital or analog media.

## **Analog Signal Processing**

Analog processing is used to offer the possibly highest quality signal to the analog to digital converter. The analog processor amplifies a certain part of the signal, boosts or attenuates the sync signal level, corrects for noise in sync and blacklevel parts, and can optionally invert the video signal.

Another basic function is to compensate for shading by differentially attenuating and amplifying the signal. Effectively this reduces the digital noise, which is added during the digitalization process.

Another important application is the amplification of images taken at low intensities of light. During amplification, however, a lot of noise is added. This is visible as "snow" in the image. But the digital processor can average several images, thus reducing snow. Details otherwise invisible can then be visualized.

The analog processor has several dials to adjust. To find optimal adjustments, an oscilloscope is used to control the video signal. Adjustments necessary for image processing and high quality digitization are as follows:

- Offset is an adjustment, which determines the threshold value for the amplification stage. Often only a part, either the darker or the lighter part, of the image should be manipulated. This part can be selected by properly adjusting the offset.
- Level is a simple adjustment, which corresponds to the brightness adjustment of any video monitor or television set. It simply rises or lowers the voltage of the video signal, making it in effect brighter or darker. The level stage precedes the offset, therefore offset has to be readjusted if the level is being changed.
- Sync level simply readjusts the sync signal. Some digitizers take the sync level as a reference for brightness. This adjustment can therefore have a direct influence on the video image.
- Shading control is a four-part adjustment. It is divided into vertical and horizontal controls. Each of them is again divided into linear and parabolic adjustment. Parabolic adjustment is used if only edges of the image should be shaded (or made brighter for that matter). Linear adjustment is used to compensate for shading from one side to the other, i.e., to change the virtual light source.

### **Real Time Digital Processing**

Real time digital processing is required to extract as much information from the original signal as possible, as otherwise information might be lost during the recording process due to low recording frequencies. Our real time processor contained two lookup tables (LUTs, both in, and out), and a storage for four images. Several methods can be applied (or implied) to process the video frames. Nonlinear contrast enhancement uses the LUT to enhance some well-defined parts of the video signal, and to provide for gamma correction. Gamma correction is an exponential transformation of gray values. It translates gray values from those coming from the camera to values that are physiological for the eye.

### **Image Compression**

High-resolution images take a lot of storage space. To produce color images each picture element must be composed of three colors. A photographic film, for example, has a resolution of at least 25 lines/mm. A 35mm color film has the format 36 by 24 mm. Therefore the absolute minimum for storing an adequate digital representation of this image without loss of information is:

$$(36\text{mm} * 25 \text{ lines/mm} ) * (24\text{mm} * 25 \text{ lines/mm} ) * 4 \text{ pixel/sample} * 3 \text{ bytes/pixel} \\ = 6,480,000 \text{ bytes}$$

To prevent aliasing problems, it is necessary to double the sampling frequency resulting in two-fold oversampling to prevent aliasing.

To reduce the amount of storage space of an image, the information has to be compressed. Compression algorithms generally make use of the fact that images contain a lot of redundant information. Other algorithms divide the image in according to important and reduce information in the less important parts. All compression algorithms can be divided

into lossless and lossy algorithms. Lossless algorithms can always reproduce the original image, as no information is lost during the compression/decompression process. The disadvantage is that lossless compressions are totally ineffective for some kind of images. Lossy compression algorithms use the fact that some parts of the image contain information that is not so important to reproduce with high fidelity than others. As a result some information is lost, but this loss is often not noticeable, and these algorithms allow for a guaranteed reduction in information.

### **Lossless Image Compression Techniques**

Digital data in images has several properties that allow often for an effective lossless compression. One feature is the normal distribution of gray values. Usually, mid range values are more often than high or low values. Furthermore, neighboring pixels are usually very similar, if not equal, in value.

The optical memory disk recorder (OMDR) we used is a recorder working with two lasers and a write-once medium. The stronger writing laser changes the reflective property of the disks surface by melting an imbedded material. The weaker reading laser can read these changes and thus reproduce the image. The laser track is a spiral growing from small to larger radius.

OMDRs do not use digital coding for video images. Instead they use a method known as pulse code modulation (PCM). High frequencies are coded by short laser pulses resulting in a fast repeating pattern of reflecting and non-reflecting stripes. Low frequencies are coded by longer pulses resulting in longer stripes. The length of stripes is variable and not fixed as with digital coding.

One disk has space for 16,000 frames. At a video rate of 30 images/s this equals to 8min 53s. In digital terms the disk has a capacity of 16,000 frames \* (540\*480) pixel/frame \* 1byte/pixel = 4.05 Gigabyte.

Control of the OMDR is achieved through an RS-224 interface at variable baud rate settings. The internal controller of the OMDR is incapable to process more than 4 commands/s, therefore practically limiting the amount of data flowing through the bus to about 150 baud. The Image1 software used does not handle communications with the OMDR properly during termination. Therefore a small program had to be developed to reset the communication line.

OMDRs allow to frame step by step and to deliver excellent still images, as well as accelerated playback up to 3 times without any modification to video adjustments. In our setup the offline frame analysis was only possible through the computer-controlled interface.

### **Image Analysis**

Image analysis comprises a variety of methods and applications in biology. It generally consists of two steps. The first step summarizes all methods to distinguish the object from its background and from irrelevant, unwanted structures. It uses information such as color and brightness as parameters.



In a second step objects are analyzed by evaluating the pixels selected from the first step. Areas or volumes can be measured by counting all interconnected pixels, i.e., pixel of similar values. Different morphological parameters can be calculated from spatial distribution of these pixels.

The results are basically grouped into four sections. These sections correspond to differences in technical approaches. In our case the first section contains all results that give information about the static organization of microtubules in *Haemanthus* endosperm cells observed by immunocytochemical studies. The second section concerns motion analysis of vesicles and chromosomes. Dynamics of microtubules themselves are studied in the third part. The fourth section bases on the former sections, because in successive steps the modeling of static arrays and the dynamics is described. It is important to observe the successive nature of the three sections, because one section bases on the results of the other. This dependency is not in the results per se, but lays in the specific design of the experiments.

### **Basic Morphology of Microtubules During the Cell Cycle**

During the cell cycle, microtubules form different arrays. With the immunogold method and brightfield microscopy, these microtubule arrays were visualized, and their images were transferred to PhotoCD™ (Kodak, Rochester, NY). Pertinent digital processing was undertaken. Processed images were reproduced on a HP Laserjet 4M/PS. The images serve to introduce the specific morphology and particularities of MT arrays in *Haemanthus* endosperm cells.

### **Motion Analysis**

Motion analysis was performed on different levels of magnification, in different stages of the cell cycle, and on microtubules, intracellular particles, and chromosomes. Generally, tracking and kymography were used for analysis.

Motion analysis was performed for all structures and areas of the cell where transport was visible, or where other dynamic processes were discernible.

These processes were the following: lateral movement of microtubules during anaphase, MT flux of the K-fiber, particle transport in phragmoplast and K-fiber, and chromosomal movement under the influence of APM.

Transport phenomena were analyzed with video kymography in the following experiments. The phase contrast images of a forming phragmoplast were visualized with a Zeiss 60/0.9 PH dry lens on a Zeiss Photoscope (Carl Zeiss, Jena, Germany). Video images were recorded with Pullnix TM-7 EX, a CCD 1/2 inch target chip camera. After preprocessing with the Colorado Video analog processor and IMAGE1 digital image processor, images were recorded at a frame rate of 5 frames/s on the Panasonic OMDR. Motion analysis was performed with the custom developed program (138).

### **Motion Analysis at the Kinetochore**

Motion and transport of particles close to the kinetochore were analyzed in this experiment which represents a special case since the chromosome is a non disjunct chromosome: It

remained at the cell plate until all other chromosomes reached the pole. Only then it started to move in the same fashion as normal chromosomes. For our observation this late start has a great advantage: the kinetochore fiber lays relatively open and free, since there are no neighboring k-fibers or other dense microtubule arrays. Furthermore, particles would be free to leave this area if they are either unattached or pushed out by chromosomes.

Consequently, this analysis allows the distinction of particles pushed by chromosomes in a caterpillar like fashion from particles that are attached to microtubules and being passively dragged by them. Particles pushed by chromosomes would have a tendency to escape to the sides, while the firmly attached particles would not be able to escape.

Any unattached particles should exhibit random movement in all directions due to Brownian motion but biased by pushing by chromosomes.

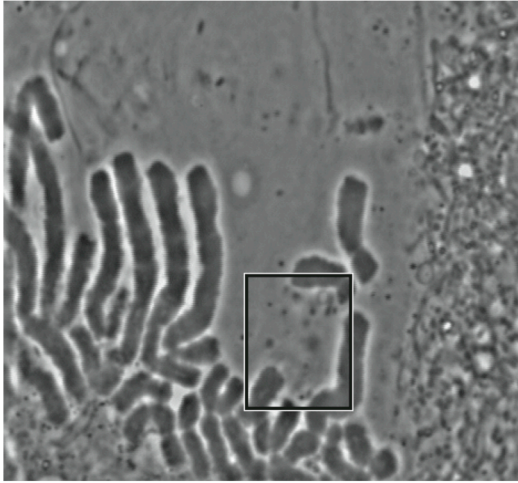
Motion was analyzed over a timespan of 1.5 s. The analysis frame was rotated by  $20^\circ$  to align the Y axes to the spindle axis and thus parallel to the MTs. Images were taken at rate of 10 frames/s.

In total, 277 particles were found. 12 particles could be traced through several frames and yielded a longer path. The path graph shows a direct movement along the spindle axis and very little side movement. Moving particles were found in varying distances from the chromosome.

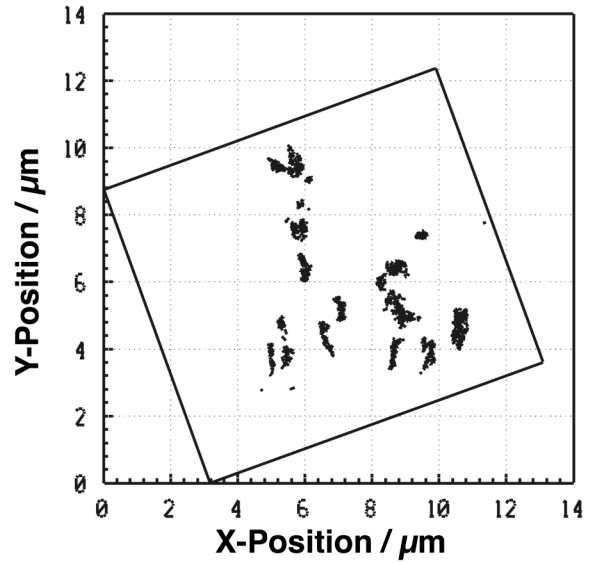
The Y axis kymograms shows basically two types of particles. Unattached particles appear as short randomly oriented lines, which indicate random oscillations. Attached particles show longer straight lines. Interestingly, the angles of these lines vary with the distance from the kinetochore. The further the lines are away from the kinetochore the smaller the angle. Motion across the spindle axis is zero for all attached particles. This indicated a very strong attachment.

Tracing of particles shows that relative distances between particles shrink. Particles closest to the kinetochore move with the same velocity as the kinetochore. The further away the particles are, the slower they move. The shortening of distances and differences in speed could be explained by a compression of the kinetochore fiber. This finding matches the observation with irradiated kinetochore fibers (130). A loss of tubulin along the kinetochore fiber and kind of a telescoping action could explain how microtubules move the kinetochores. It also explains the loss of fluorescence observed during anaphase (137).

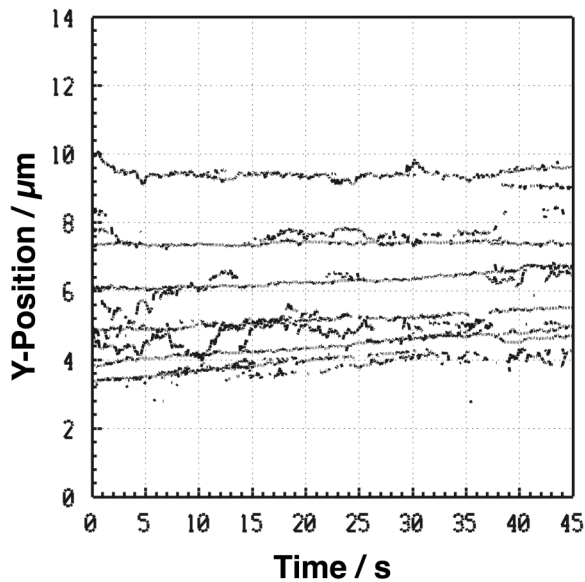
### Phase Contrast Image



### Particle Path



### Axial Movement



### Orthogonal Movement

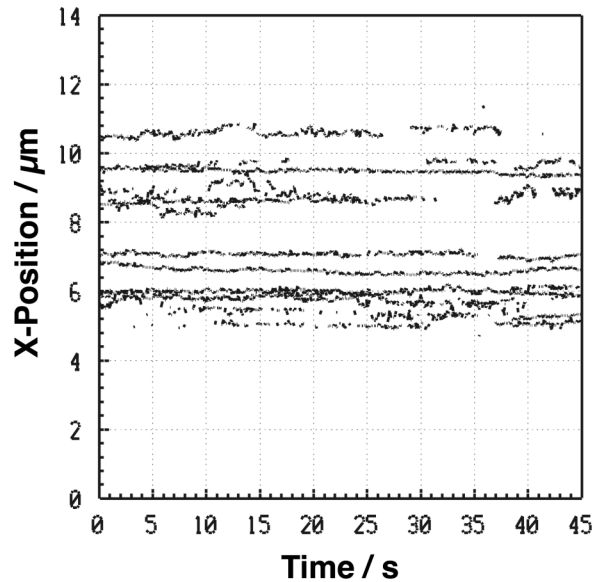


**Figure 26: Particle Motion Analysis at the Kinetochore**

The phase contrast image shows the first frame of the motion sequence. The black rectangle indicates the analyzed area. The particle path graph shows the reconstruction of all particles during a 45 s sequence. All of the visual particles move along the kinetochore fiber axis. The axial movement graph shows the decrease in distance between the particles. The orthogonal movement graph does not show any movement perpendicular to the kinetochore fiber axis.

### MT Bundling

MT bundling is an ubiquitous process in living cells. We especially looked at bundling and MT dynamics at the metaphase to anaphase transition. This transition is marked by an

event where chromosomes start moving toward the opposite poles (anaphase a). We recorded the transition at high magnification with DIC and analog plus digital enhancement. These processing steps amplified small differences in contrast to become visible without amplifying noise. The analog processor amplified the amplitude of the analog signal to match the dynamic range of the Image1 digitizer.

The image series was then transformed into a series of kymograms. One set of kymograms was obtained registering particle movements parallel to the kinetochore fiber, and one kymograph movements occurring perpendicular to the spindle axis. Because the kinetochore fiber rotated slightly, angular adjustments were necessary to gain parallel kymograms.

The axial kymogram (Figure 28) shows clearly the movement of microdomains, similar to the observation of (144), and matches the observation of Mitchison in terms of velocity of microtubule flux (147).

The orthogonal kymogram reveals extensive amounts of MT bundling. The light microscope cannot completely resolve the real distances of microtubules. However, the distance of larger bundles can be clearly resolved. The kymogram shows several instances of decrease in distance, but never an increase. This excludes the possibility of simple lateral movement. Lateral movements would exhibit an equal number of areas with decreasing and increasing distance. Thus we can demonstrate that bundling is an intrinsic process in the kinetochore fiber of *Haemaphysalis katherinae*.

Close lateral association can also be observed in electron microscopy. Although the picture is static, this close association presents additional evidence for bundling processes in kinetochore fibers.

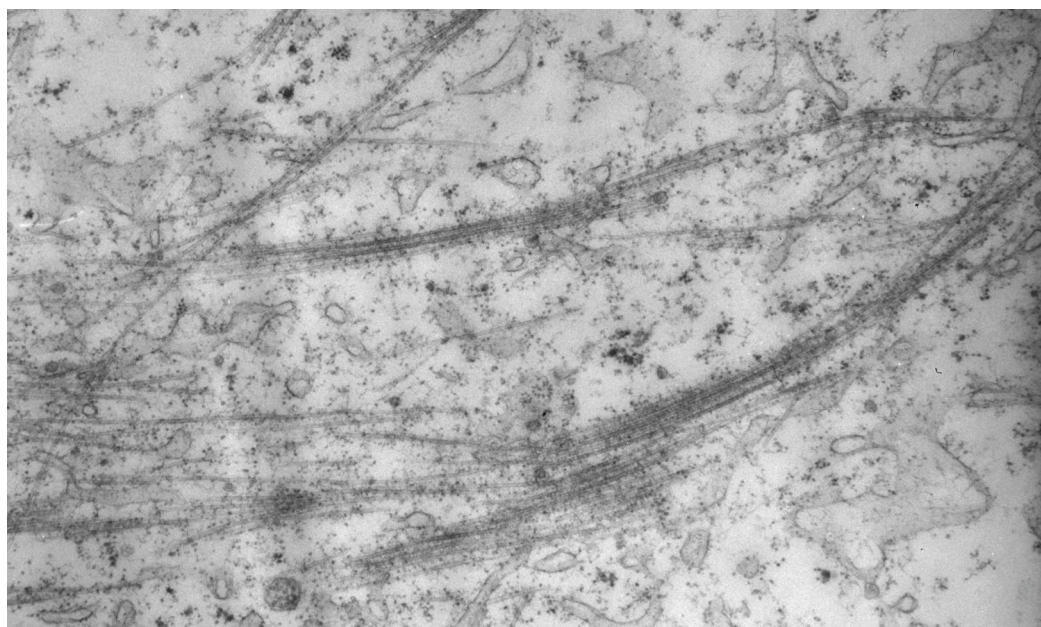
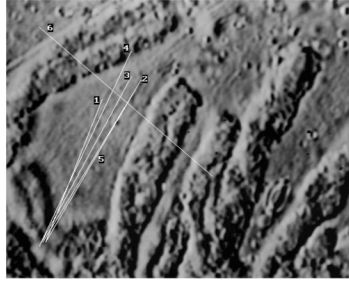


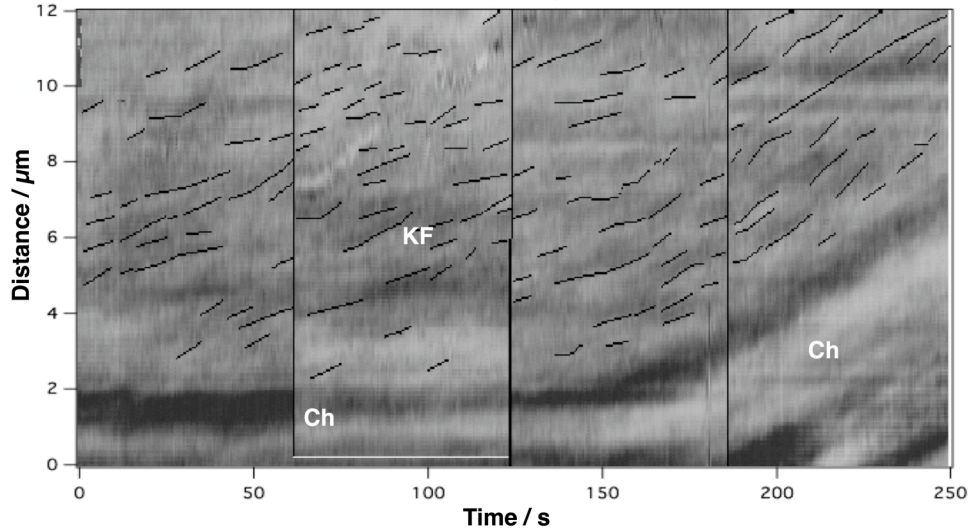
**Figure 27: Electron micrograph of microtubules**

*Electron micrograph of microtubules in the kinetochore fiber of Haemaphysalis katherinae. The dark parallel lines are microtubules. Denser areas represent microtubule bundles. Image courtesy of Andrew Bajer.*



Video Frame with orientation of kymogram vectors.  
 Angles for k-fiber parallel vectors had to be reoriented, because the kinetochore fiber tilted slowly during the experiment. The reorientation is visible as vertical lines in the kymogram.  
 The orthogonal vector did not have to be reoriented.

### Axial Kymogram



### Orthogonal Kymogram

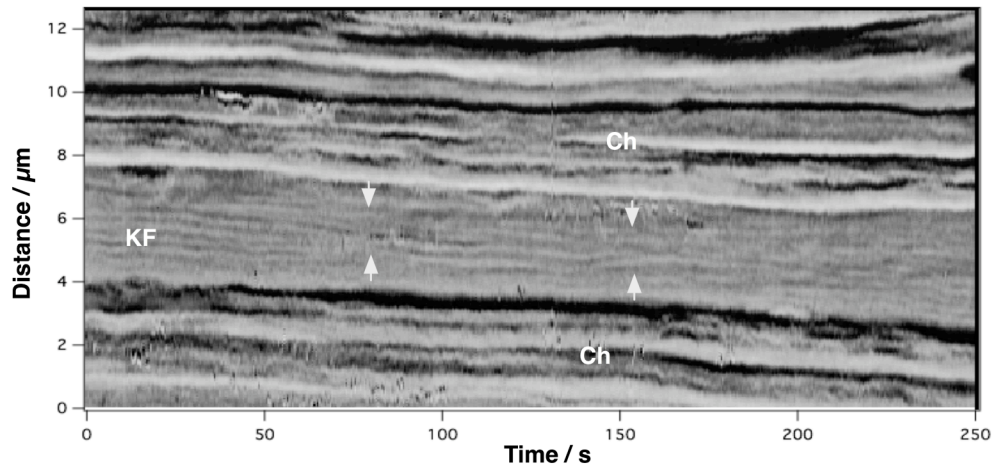


### Figure 28: Kymogram of Kinetochore Fiber Dynamics

The video frame shows the chromosomes and kinetochore fibers. The lines indicate the localization and orientation of kymogram vectors. The axial kymogram shows the trace patterns for microtubules and kinetochores at the end of metaphase and beginning of anaphase. The orthogonal kymogram shows the movement and bundling (see arrows) of microtubules. Ch = chromosome, KF = kinetochore fiber, arrows indicate bundling



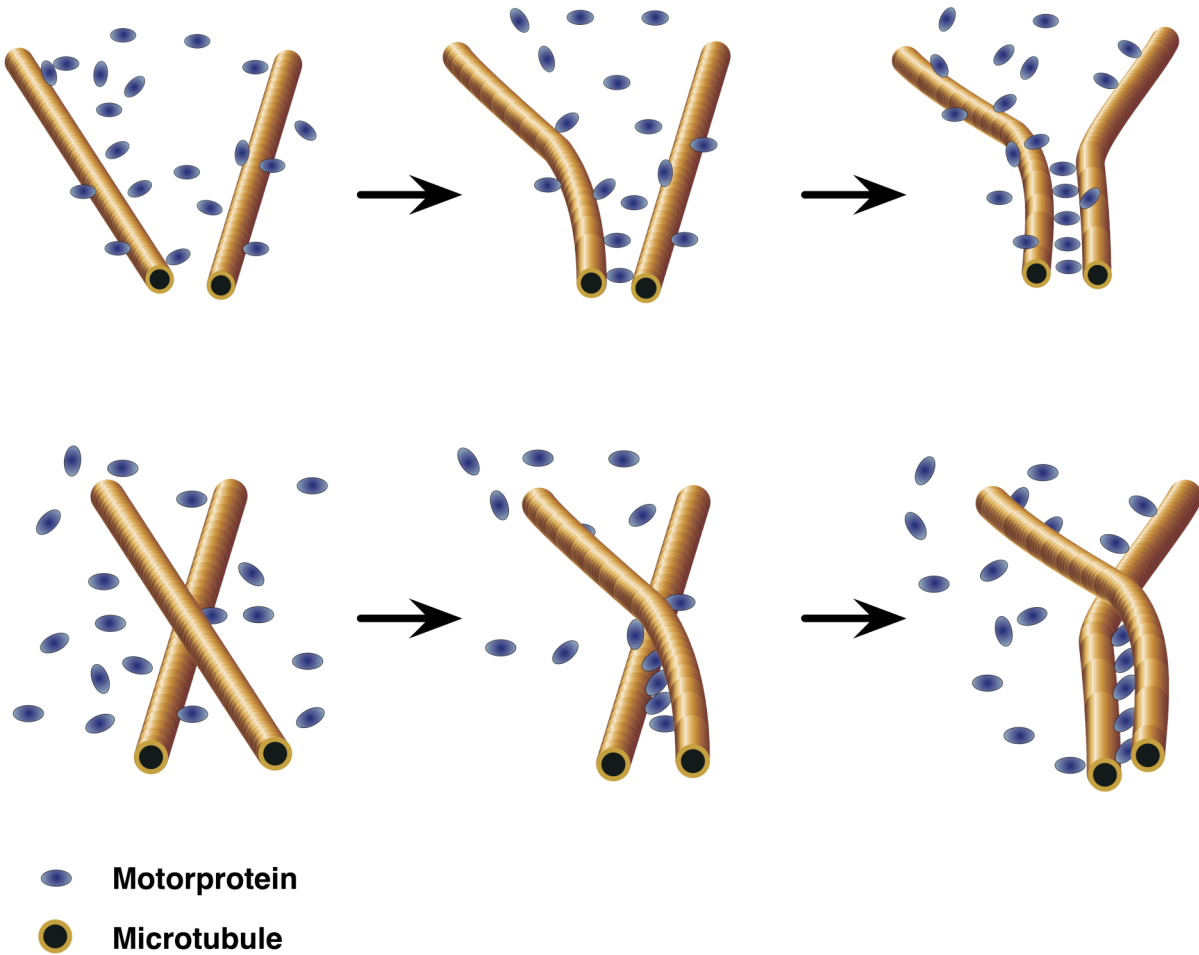


**Figure 29: Microtubule Bundling**

*The image illustrates how V-shaped or X shaped microtubule configurations become Y-shaped by bundling with motor proteins. Motor proteins: blue, microtubules: brown*

### **Microtubule Self-Organization**

Microtubule arrays can form spontaneously in plant cells. Because cells are very large (sometimes 100  $\mu\text{m}$  in diameter) it is easy to fragment them during preparation. During preparation the cells often lose small pieces of cytoplasm. These cytoplasts do not have a cell nucleus and are basically packets of cell plasma with a surrounding membrane. However, MTs are able to form complete arrays in these cytoplasts. Some form even complete mitotic spindles without the presence of chromosomes. This self-organization process happens without a visible, special cellular architecture and the signals it would provide. So we have to assume that microtubules and the associated proteins “know” how to form these arrays without outside signals or discrete organizing centers, i.e. they do this by self assembly processes driven by intrinsic conditions.

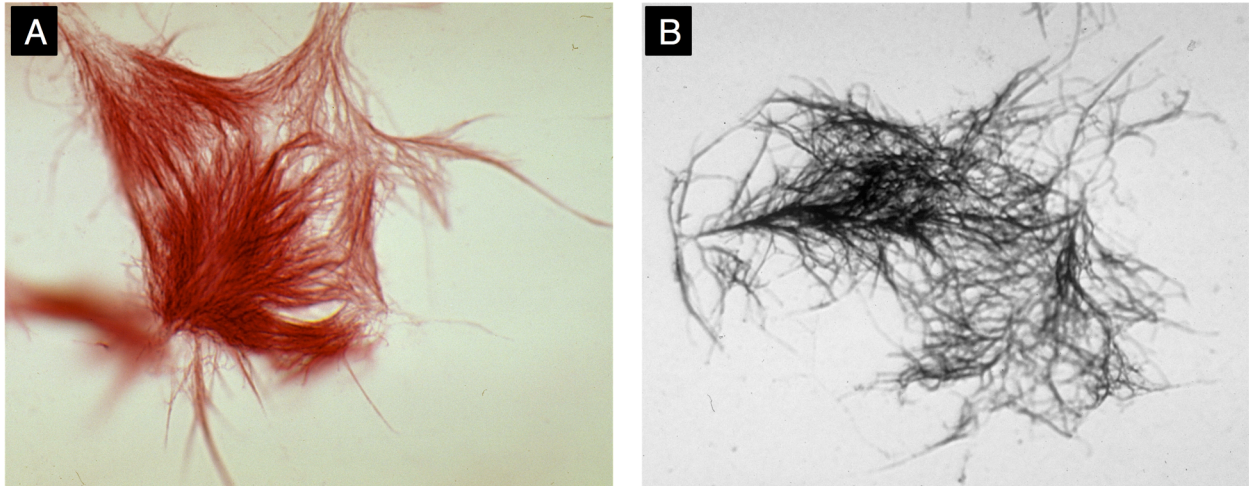


**Figure 30: Self-organizing Microtubules in Cytoplasts**

The two pictures show microtubules stained with the immuno-gold method. A) The cytoplast develops a spindle like organization on the left side, and microtubules show pointed arrays. B) The array is less well organized as in A. However, the sample shows microtubule bundles

### **Fragments May Work like a Complete Systems**

After we saw that fragments can organize microtubules into complex arrays, the question remained how functional these arrays are. To answer this question, we looked at kymographic motion analysis of a fragmented mitotic spindle formed by a complete cell which had been accidentally fragmented during preparation. If the mitotic spindle requires both a careful balance of forces and counter forces and the interaction of microtubules of opposite polarity, fragments should be expected stopping to function.

We recorded a phase contrast movie of a chromosome that had been pushed to the periphery of the cell, and we could clearly observe the movement of that chromosome.

To find out if this movement was caused by kinetochore microtubules we performed a kymographic analysis. The kymogram showed both the shortening of the kinetochore fiber and the movement of the isolated chromosome. This result indicates that in *Haemaphysalis* each part of the mitotic spindle may function as an independent unit. Chromosome movements only require the kinetochore fiber MTs, but not a complete spindle machinery, to move to the pole. The forces required to move a chromosome are very small, so the anchoring of the fragmented spindle was still sufficient to allow for that process. This could explain why mitotic spindles in plants do not need a clearly defined spindle pole and do not need dedicated microtubule organizing centers. The evidence thus seems to point toward a distributed processing system.

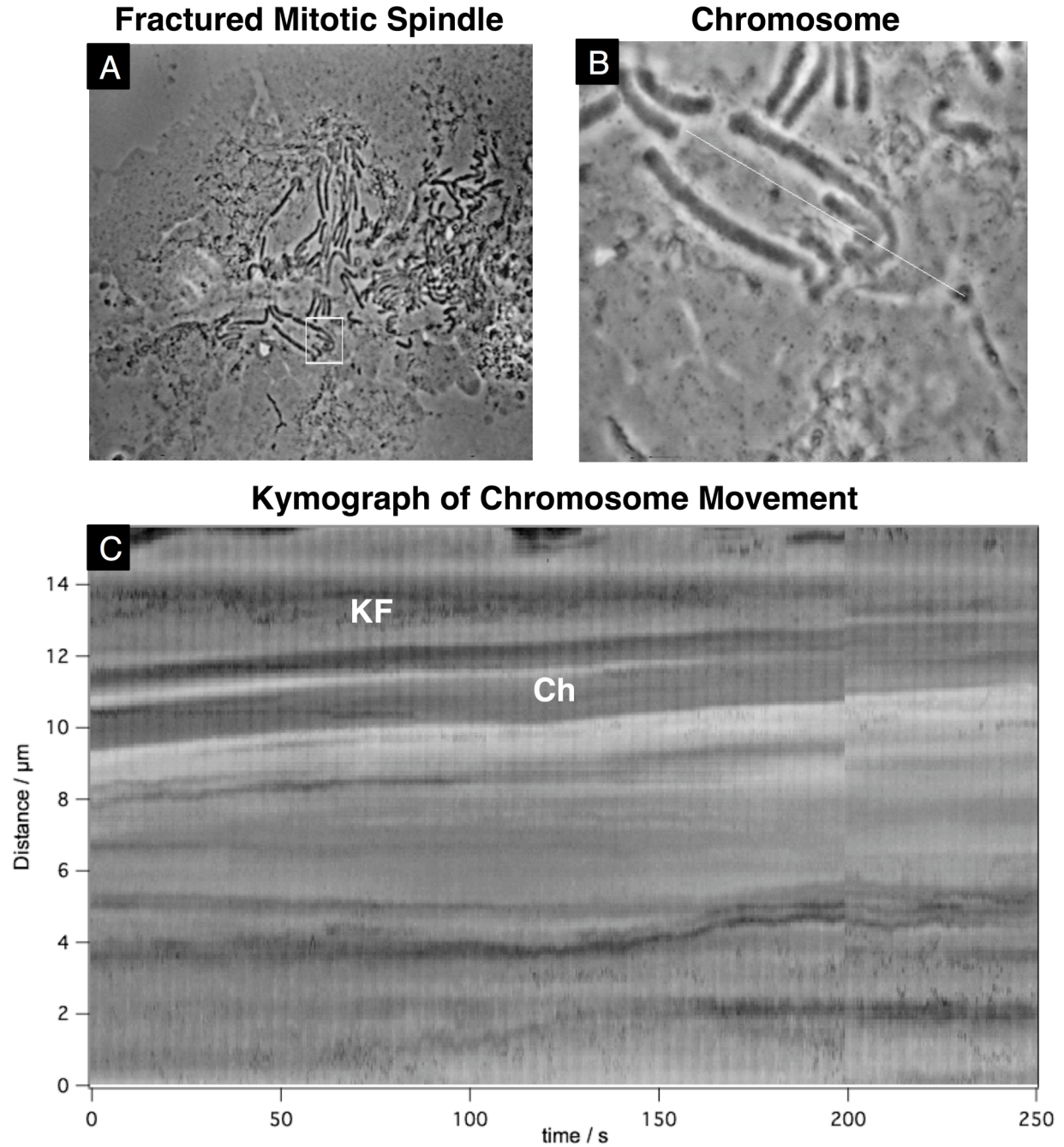


**Figure 31: Function of a Fractured Mitotic Spindle**

A) Phase contrast image of a *Haemanthus endosperm* cell fractured into many pieces during sample preparation. The white rectangle indicates the analyzed area. B) Higher magnification of the chromosome in phase contrast. The white line indicates the vector of the kymogram. C) The kymogram shows the movement of the chromosome (Ch) as well as the kinetochore fiber (KF). The lower half shows the motion of particles that were influenced by the chromosome movement.



## ***Describing Microtubule Arrays with L-System Fractals***

L-system fractals describe branching systems. They found wide application in computer graphics to model plants and plant growth. We apply the same principles to the growth and morphology of plant microtubules. However, to simply apply a branching system to straight non-branching microtubules and microtubule arrays does not help to explain any new observations. Current models explain genesis of microtubule arrays by assuming a sliding process that bundles microtubules in star like formations. If that process is biased to one side, directional fan shaped arrays may result.

However, there is one microtubule array that cannot be explained by these linear processes: spirals made up of MTs, which can form naturally in cytoplasts, or under conditions of rapid assembly.

The hallmark of spirals is that microtubules are slightly bent (Figure 32). Therefore we test the hypothesis that spirals are similar to the linear tree like arrays, except that the assembly process has a slight tilt.

We start with a regular linear branching model. Although the resulting fractal is very regular and the naturally occurring arrays are more disorganized (Figure 32), we can still see a strong resemblance. However, if we change the formula by introducing a small bias to one side, we get a spiral after 5 iterations (Figure 33).

Two factors are critical: The branching angle must be exactly 23 degrees, or the spiral would not form. The second condition is that at most one branch is added to each linear segment. If either criteria are not met, the spiral will not form.

We looked at the intermediate iterations of the fractal representation (Figure 33). Surprisingly these iterations show array configurations that are frequently observed in *Haemanthus* (148). Because these intermediate arrays exist in many cells, we can speculate that these might be precursors to spiral arrangements.

But, finally, how do these fractal models enhance our understanding of microtubule organization? First we could demonstrate that a bundling process alone can explain complex arrays that could not be explained before. Microtubule bundling has been attributed to MAPs and motor proteins. Our results shed new light on the function of motor proteins. What if their primary function is not transport, but to organize microtubules into scaffolds by cross-linking and bundling? This hypothesis would explain a lot of the findings about microtubule dynamics. It explains why bundling occurs without energy (ATP), and with truncated proteins. Furthermore, a redundant system of MAPs and motor proteins would explain why a single knockout often does not produce a severe phenotype.

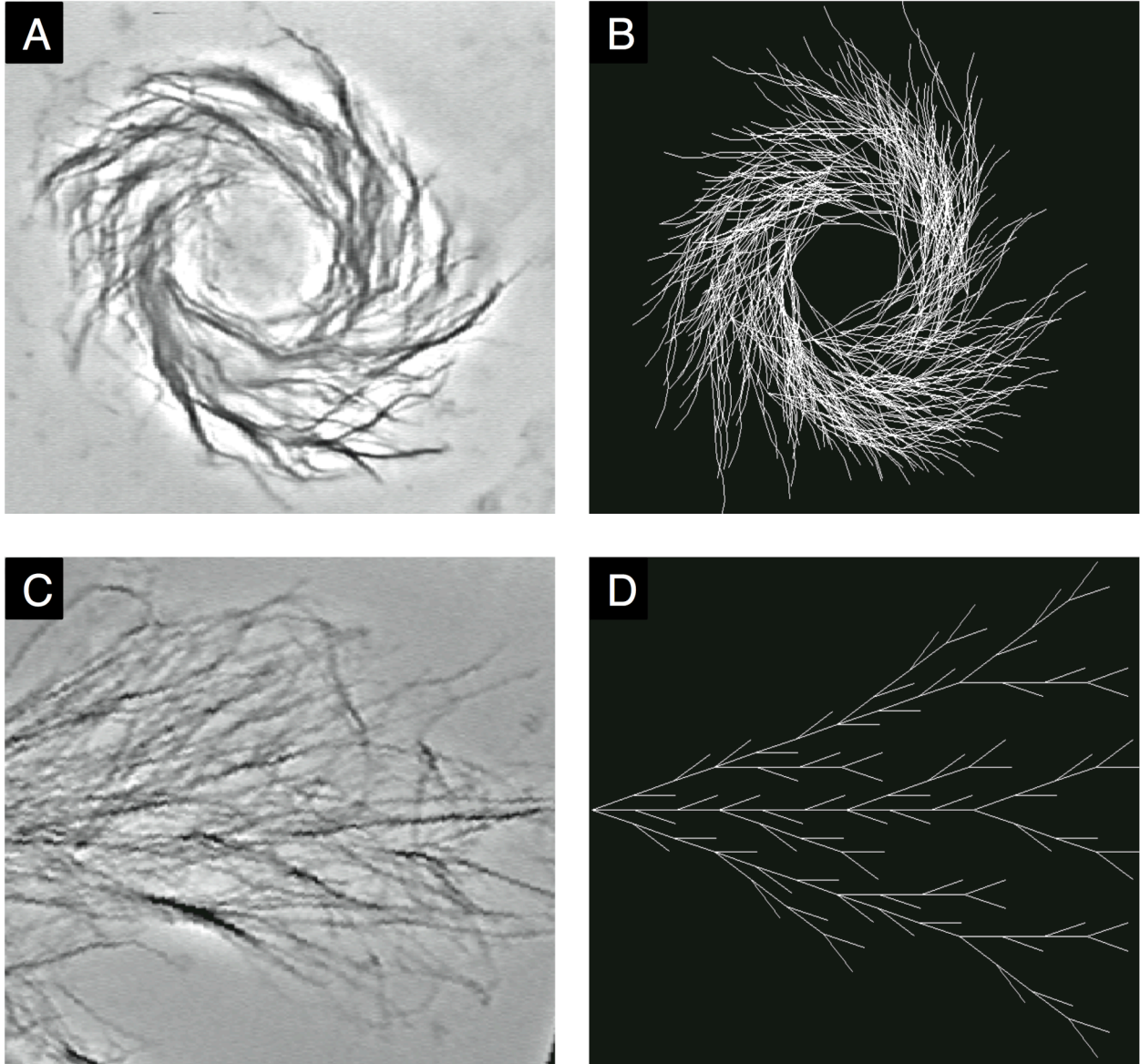


**Figure 32: Fractals and Microtubule Arrays**

*A) Video enhanced image of a microtubule spiral stained with immuno-gold. B) The corresponding L-systems fractal. C) Cell with fan shaped microtubule arrays. D) Fractal model of fan shaped arrays.*

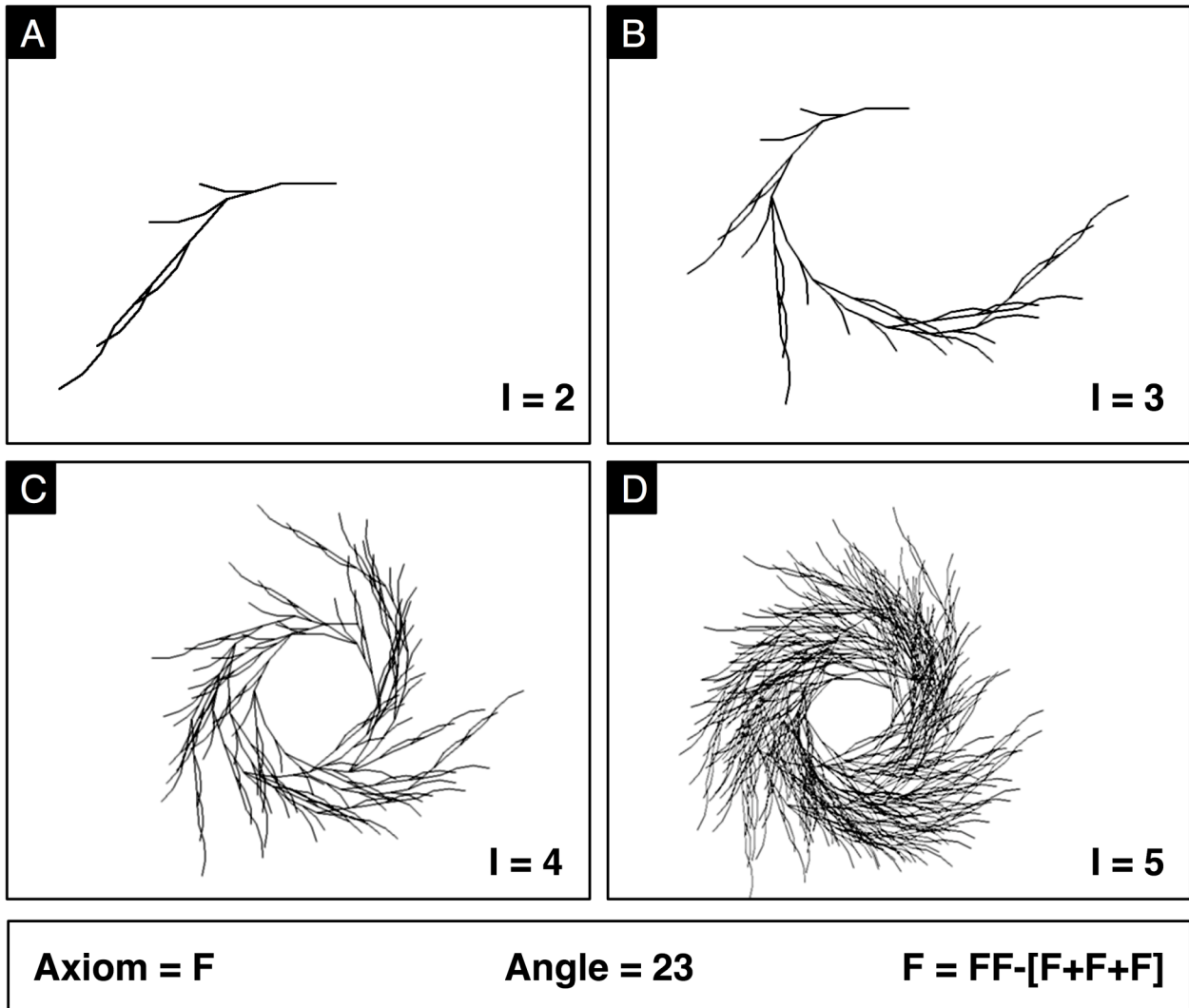


**Figure 33: Iterations of L-System Spirals**

*A-D) Graphs show the iterations 2 through 5 of the spiral fractal. Microtubule arrays resembling these iterations can be found in cells.*

## Conclusion

The computer and software become more important for discovery in the life sciences. The development is not even over the different areas of life science research, but no area can be excluded. The role of the computer changes from a supporting instrument to an essential device for discovery.

The human genome project represented a sea change in the life sciences. One of the hallmarks of this project is the rapid development of bioinformatics. Sequencing and analyzing genomes are unthinkable without the computer. Advances and discovery in genetics depend on bioinformatics. Sequencing is performed by computer controlled automated high throughput methods. Whole genome shotgun assembly of the gene fragments requires supercomputer capabilities. Genetics is at the forefront of bioinformatics revolution, but not the only area where the computer became the essential tool for discovery.

The computer has a growing importance in cell biology and microscopy. Video microscopy and digital cameras are a mainstay in modern microscopy. They predate the computer revolution. But advanced imaging methods such as confocal, 2 photon and, stimulated emission depletion cannot be performed without the help of a computer. Image processing and analysis becomes the pivotal tool for quantitation, visualization, and modeling. The computer is a crucial tool for discovery in high-resolution multidimensional imaging.

Volume visualization software allows us to explore complex imaging data. To create state-of-art visualization software we combined advances in software development methodology, hardware graphics acceleration, and processor design. The rendering algorithms are optimized for speed for interactivity and account for human visual perception. These advances allowed the investigation of such diverse processes as development of zebrafish pituitary on a cellular level and the degeneration of nerve fibers after injury.

Physiological imaging poses significant challenges, because the imaging process can influence and even kill the cells under observation. A low impact imaging method in combination with a signal analysis software allowed us to generate drug response curves for single cells. These measurements help to identify and characterize receptors that modulate calcium oscillations and augment drug discovery and development.

Modeling of self-organizing molecular processes poses significant challenges. Microtubules form a complex network in conjunction with motor proteins and other MAPs. Fractals are a useful tool to describe self-similar branching structures. We demonstrated that fractals explain structures such as spirals and features such as self-similarity, which can not be explained by other models.

In summary we demonstrated how the development of new software allowed advances in three areas of microscopy: Volume visualization of multimodal multidimensional images in confocal microscopy, quantitation of drug effects on cellular calcium fluxes, and a fractal modeling of microtubule organization.

## References

1. Stevens JK, Mills LR, Trogadis JE. Three-Dimensional Confocal Microscopy: Volume Investigation of Biological Specimen. Buetow DE, Cameron IL, Padilla GM, Zimmerman AM, editors. San Diego, CA: Academic Press Inc.; 1994.
2. White NS. Visualization systems for multidimensional CLSM images. In: JB P, editors. Handbook of Biological Confocal Microscopy. New York: Plenum; 1995. p. 211– 254.
3. Lichtenbelt B, Crane R, Naqvi S. Introduction to Volume Rendering. Upper Saddle River, NJ, 07458: Prentice Hall PTR; 1998.
4. Schroeder, Martin, Lorensen. The Visualization Toolkit: An Object-Oriented Approach to 3-D Graphics. Prentice-Hall; 1997.
5. Allard J, Raffin B. A shader-based parallel rendering framework., in *Visualization, 2005 VIS 05 IEEE*. (2005).
6. Kruger J, Westermann R. Acceleration techniques for GPU-based volume rendering., in *Visualization, 2003 VIS 2003 IEEE*. (2003).
7. Vega-Higuera F, Hastreiter P, Fahlbusch R, Greiner G. High performance volume splatting for visualization of neurovascular data., in *Visualization, 2005 VIS 05 IEEE*. (2005).
8. Westerhoff M. Efficient Visualization and Reconstruction of 3D Geometric Models from Neuro-Biological Confocal Microscope Scans, *Dissertation*. (2004).
9. Espinha R, Celes W. High-Quality Hardware-Based Ray-Casting Volume Rendering Using Partial Pre-Integration., in *Computer Graphics and Image Processing, 2005 SIBGRAPI 2005 18th Brazilian Symposium on*. (2005).
10. Persoon MP, Serlie IWO, Post FH, Truyen R, Vos FM. Visualization of noisy and biased volume data using first and second order derivative techniques., in *Visualization, 2003 VIS 2003 IEEE*. (2003).
11. Clendenon JL, Phillips CL, Sandoval RM, Fang S, Dunn KW. Voxx: a PC-based, near real-time volume rendering system for biological microscopy. *Am J Physiol Cell Physiol*. 2002;282:C213-8.
12. Rosset A, Spadola L, Ratib O. OsiriX: an open-source software for navigating in multidimensional DICOM images. *J Digit Imaging*. 2004;17:205-16.
13. van der Voort HT, Brakenhoff GJ, Baarslag MW. Three-dimensional visualization methods for confocal microscopy. *J Microsc*. 1989;153 :123-32.
14. Lorenzen, Cline. Marching cubes: A high resolution 3D surface construction algorithm., in *Computer Graphics (SIGGRAPH 87 Proceedings)*. (1987).
15. Hendee WR, Wells PNT. The Perception of Visual Information. New York, Berlin, Heidelberg: Springer Verlag; 1993.
16. Zakia R. Perception and Imaging. Focal Press; 2002.

17. Messerli JM, Perriard JC. Three-dimensional analysis and visualization of myofibrillogenesis in adult cardiomyocytes by confocal microscopy. *Microsc Res Tech.* 1995;30:521-30.
18. Upson C, Jr. TF, Kamins D, Laidlaw DH, Schlegel D, Vroom J, et al. The Application Visualization System: A Computational Environment for Scientific Visualization. *Computer Graphics and Applications.* 1989;9:30-42.
19. Zernike F. How I discovered phase contrast. *Science.* 1955;121:345-9.
20. Nomarski G. From phase contrast to contrast by interference. *Rev Hematol.* 1957;12:439-42.
21. Haugland RP. *Handbook of Fluorescent Probes and Research Products.* Grgory JG, editors. Molecular Probes; 2002.
22. Hicks BW. *Green Fluorescent Protein: Applications Protocols.* Humana Press; 2002.
23. Harper IS. Fluophores and Their Labeling Procedures for Monitoring Various Biological Signals. In: Periasamy A, editors. *Methods in Cellular Imaging.* Oxford University Press; 2001.
24. Kerr R, Lev-Ram V, Baird G, Vincent P, Tsien RY, Schafer WR. Optical imaging of calcium transients in neurons and pharyngeal muscle of *C. elegans*. *Neuron.* 2000;26:583-94.
25. Lakowicz JR, Szmacinski H, Nowaczyk K, Johnson ML. Fluorescence lifetime imaging of free and protein-bound NADH. *Proc Natl Acad Sci U S A.* 1992;89:1271-5.
26. Lemasters JJ, Qian T, Trollinger DR, Muller-Borer BJ, Elmore SP, Cascio WE. *Laser Scanning Confocal Microscopy Applied to Living Cells and Tissues.* In: Periasamy A, editors. *Methods in Cellular Imaging.* Oxford University Press; 2001.
27. Hell SW. Toward fluorescence nanoscopy. *Nat Biotechnol.* 2003;21:1347-55.
28. Hammond AT, Glick BS. Raising the speed limits for 4D fluorescence microscopy. *Traffic.* 2000;1:935-40.
29. Truong K, Ikura M. The use of FRET imaging microscopy to detect protein-protein interactions and protein conformational changes in vivo. *Curr Opin Struct Biol.* 2001;11:573-8.
30. Bouma BE, Tearney GJ. *Handbook of Optical Coherence Tomography.* Bouma BE, Tearney GJ, editors. Marcel Dekker; 2001.
31. Perlman ZE, Slack MD, Feng Y, Mitchison TJ, Wu LF, Altschuler SJ. Multidimensional drug profiling by automated microscopy. *Science.* 2004;306:1194-8.
32. Andrews PD, Harper IS, Swedlow JR. To 5D and beyond: quantitative fluorescence microscopy in the postgenomic era. *Traffic.* 2002;3:29-36.
33. Liu NA, Liu Q, Wawrowsky K, Yang Z, Lin S, Melmed S. Prolactin receptor signaling mediates the osmotic response of embryonic zebrafish lactotrophs. *Mol Endocrinol.* 2005;20:871-80.

34. Liu S, Weaver DL, Taatjes DJ. Three-dimensional reconstruction by confocal laser scanning microscopy in routine pathologic specimens of benign and malignant lesions of the human breast. *Histochem Cell Biol.* 1997;107:267-78.
35. Gillingwater TH, Wishart TM, Chen PE, Haley JE, Robertson K, MacDonald SH, et al. The neuroprotective WldS gene regulates expression of PTTG1 and erythroid differentiation regulator 1-like gene in mice and human cells. *Hum Mol Genet.* 2006;15:625-35.
36. Miledi R, Slater CR. On the degeneration of rat neuromuscular junctions after nerve section. *J Physiol.* 1970;207:507-28.
37. Lunn ER, Perry VH, Brown MC, Rosen H, Gordon S. Absence of Wallerian Degeneration does not Hinder Regeneration in Peripheral Nerve. *Eur J Neurosci.* 1989;1:27-33.
38. Gillingwater TH, Haley JE, Ribchester RR, Horsburgh K. Neuroprotection after transient global cerebral ischemia in Wld(s) mutant mice. *J Cereb Blood Flow Metab.* 2004;24:62-6.
39. Bijlstra PJ, Russel FG, Thien T, Lutterman JA, Smits P. Effects of tolbutamide on vascular ATP-sensitive potassium channels in humans. Comparison with literature data on glibenclamide and glimepiride. *Horm Metab Res.* 1996;28:512-6.
40. Soll AH. Review: antisecretory drugs: cellular mechanisms of action. *Aliment Pharmacol Ther.* 1987;1:77-89.
41. Erxleben C. Stretch-activated current through single ion channels in the abdominal stretch receptor organ of the crayfish. *J Gen Physiol.* 1989;94:1071-83.
42. Kawada T, Yamazaki T, Akiyama T, Uemura K, Kamiya A, Shishido T, et al. Effects of Ca<sup>2+</sup> channel antagonists on nerve stimulation-induced and ischemia-induced myocardial interstitial acetylcholine release in cats. *Am J Physiol Heart Circ Physiol.* 2006.
43. Neher E, Sakmann B. Single-channel currents recorded from membrane of denervated frog muscle fibres. *Nature.* 1976;260:799-802.
44. Hamill OP, Marty A, Neher E, Sakmann B, Sigworth FJ. Improved patch-clamp techniques for high-resolution current recording from cells and cell-free membrane patches. *Pflugers Arch.* 1981;391:85-100.
45. Lino. Single molecule imaging of green fluorescent proteins in living cells: E-cadherin forms oligomers on the free cell surface. *Biophys. J.* 2001;80:2667-2677.
46. Sonleitner A, Mannuzzu LM, Terakawa S, Isacoff EY. Structural rearrangements in single ion channels detected optically in living cells. *Proc Natl Acad Sci U S A.* 2002;99:12759-64.
47. Zou H, Lifshitz LM, Tuft RA, Fogarty KE, Singer JJ. Visualization of Ca<sup>2+</sup> entry through single stretch-activated cation channels. *Proc Natl Acad Sci U S A.* 2002;99:6404-9.
48. Berridge MJ. The AM and FM of calcium signalling. *Nature.* 1997;386:759-60.
49. Zhang CL, Wu BJ. Development of calcium fluorescent probes and their application in life sciences. *Sheng Li Ke Xue Jin Zhan.* 1996;27:37-42.

50. Ben-Shlomo A, Wawrowsky KA, Proekt I, Wolkenfeld NM, Ren SG, Taylor J, et al. Somatostatin receptor type 5 modulates somatostatin receptor type 2 regulation of adrenocorticotropin secretion. *J Biol Chem*. 2005;280:24011-21.
51. Farkas DL, Baxter G, DeBiasio RL, Gough A, Nederlof MA, Pane D, et al. Multimode light microscopy and the dynamics of molecules, cells, and tissues. *Annu Rev Physiol*. 1993;55:785-817.
52. Eggertsen R, Hansson L. Vasodilators in hypertension--a review with special emphasis on the combined use of vasodilators and beta-adrenoceptor blockers. *Int J Clin Pharmacol Ther Toxicol*. 1985;23:411-23.
53. Bonnefont X, Fiekers J, Creff A, Mollard P. Rhythmic bursts of calcium transients in acute anterior pituitary slices. *Endocrinology*. 2000;141:868-75.
54. Kwiecien R, Robert C, Cannon R, Vigues S, Arnoux A, Kordon C, Hammond C. Endogenous pacemaker activity of rat tumour somatotrophs. *J Physiol*. 1998;508 ( Pt 3):883-905.
55. Schlegel W, Winiger BP, Mollard P, Vacher P, Wuarin F, Zahnd GR, et al. Oscillations of cytosolic Ca<sup>2+</sup> in pituitary cells due to action potentials. *Nature*. 1987;329:719-21.
56. Kwiecien R, Hammond C. Differential management of Ca<sup>2+</sup> oscillations by anterior pituitary cells: a comparative overview. *Neuroendocrinology*. 1998;68:135-51.
57. Gill DL, Patterson RL. Toward a consensus on the operation of receptor-induced calcium entry signals. *Sci STKE*. 2004;2004:pe39.
58. Tse A, Lee AK. Voltage-gated Ca<sup>2+</sup> channels and intracellular Ca<sup>2+</sup> release regulate exocytosis in identified rat corticotrophs. *J Physiol*. 2000;528 Pt 1:79-90.
59. Berridge MJ, Lipp P, Bootman MD. The versatility and universality of calcium signalling. *Nat Rev Mol Cell Biol*. 2000;1:11-21.
60. Shuttleworth TJ, Mignen O. Calcium entry and the control of calcium oscillations. *Biochem Soc Trans*. 2003;31:916-9.
61. Fiekers JF, Konopka LM. Spontaneous transients of [Ca<sup>2+</sup>]<sub>i</sub> depend on external calcium and the activation of L-type voltage-gated calcium channels in a clonal pituitary cell line (AtT-20) of cultured mouse corticotropes. *Cell Calcium*. 1996;19:327-36.
62. Adler M, Sabol SL, Busis N, Pant HC. Intracellular calcium and hormone secretion in clonal AtT-20/D16-16 anterior pituitary cells. *Cell Calcium*. 1989;10:467-76.
63. Charles AC, Piros ET, Evans CJ, Hales TG. L-type Ca<sup>2+</sup> channels and K<sup>+</sup> channels specifically modulate the frequency and amplitude of spontaneous Ca<sup>2+</sup> oscillations and have distinct roles in prolactin release in GH3 cells. *J Biol Chem*. 1999;274:7508-15.
64. Nogales E, Wang HW. Structural mechanisms underlying nucleotide-dependent self-assembly of tubulin and its relatives. *Curr Opin Struct Biol*. 2006;16:221-9.
65. Nogales E, Wolf SG, Downing KH. Structure of the alpha beta tubulin dimer by electron crystallography. *Nature*. 1998;391:199-203.



66. Tirnauer JS, Salmon ED, Mitchison TJ. Microtubule plus-end dynamics in *Xenopus* egg extract spindles. *Mol Biol Cell*. 2004;15:1776-84.
67. Sammak PJ, Borisy GG. Direct observation of microtubule dynamics in living cells. *Nature*. 1988;332:724-6.
68. Mitchison TJ, Kirschner M. Dynamic instability of microtubule growth. *Nature*. 1984;312:237-42.
69. Euteneuer U, Jackson WT, McIntosh JR. Polarity of spindle microtubules in *Haemaphysalis endosperm*. *J Cell Biol*. 1982;94:644-53.
70. Kuriyama R. In vitro polymerization of flagellar and ciliary outer fiber tubulin into microtubules. *J Biochem (Tokyo)*. 1976;80:153-65.
71. Sackett DL, Bhattacharyya B, Wolff J. Local unfolding and the stepwise loss of the functional properties of tubulin. *Biochemistry*. 1994;33:12868-78.
72. Cytrynbaum EN, Rodionov V, Mogilner A. Computational model of dynein-dependent self-organization of microtubule asters. *J Cell Sci*. 2004;117:1381-97.
73. Hotani H, Horio T. Dynamics of microtubules visualized by darkfield microscopy: treadmilling and dynamic instability. *Cell Motil Cytoskeleton*. 1988;10:229-36.
74. Mandelkow EM, Mandelkow E, Milligan RA. Microtubule dynamics and microtubule caps: a time-resolved cryo-electron microscopy study. *J Cell Biol*. 1991;114:977-91.
75. Mitchison TJ, Kirschner MW. Properties of the kinetochore in vitro. II. Microtubule capture and ATP-dependent translocation. *J Cell Biol*. 1985;101:766-77.
76. Wolf KW. Behavior of C-shaped microtubule endings in the cell. *Cell Motil Cytoskeleton*. 1990;17:59-67.
77. Goshima G, Nédélec F, Vale RD. Mechanisms for focusing mitotic spindle poles by minus end-directed motor proteins. *J Cell Biol*. 2005;171:229-40.
78. Mitchison TJ, Maddox P, Gaetz J, Groen A, Shirasu M, Desai A, et al. Roles of polymerization dynamics, opposed motors, and a tensile element in governing the length of *Xenopus* extract meiotic spindles. *Mol Biol Cell*. 2005;16:3064-76.
79. Goshima G, Vale RD. The roles of microtubule-based motor proteins in mitosis: comprehensive RNAi analysis in the *Drosophila* S2 cell line. *J Cell Biol*. 2003;162:1003-16.
80. Vallee RB, Williams JC, Varma D, Barnhart LE. Dynein: An ancient motor protein involved in multiple modes of transport. *J Neurobiol*. 2004;58:189-200.
81. McDonald HB, Stewart RJ, Goldstein LS. The kinesin-like *ncd* protein of *Drosophila* is a minus end-directed microtubule motor. *Cell*. 1990;63:1159-65.
82. Howard J. The movement of kinesin along microtubules. *Annu Rev Physiol*. 1996;58:703-29.
83. Bastmeyer M, Russell DG. Characterization of *Pales* spermatocyte spindles, with reference to an MTOC-associated protein. *J Cell Sci*. 1987;87 ( Pt 3):431-8.

84. McBeath E, Fujiwara K. Microtubule detachment from the microtubule-organizing center as a key event in the complete turnover of microtubules in cells. *Eur J Cell Biol.* 1990;52:1-16.
85. Cassimeris L, Rieder CL, Salmon ED. Microtubule assembly and kinetochore directional instability in vertebrate monopolar spindles: implications for the mechanism of chromosome congression. *J Cell Sci.* 1994;107 ( Pt 1):285-97.
86. Wolf R. The cytaster, a colchicine-sensitive migration organelle of cleavage nuclei in an insect egg. *Developmental Biology.* 1978;62:464-472 .
87. Gorbsky GJ, Sammak PJ, Borisy GG. Chromosomes move poleward in anaphase along stationary microtubules that coordinately disassemble from their kinetochore ends. *J Cell Biol.* 1987;104:9-18.
88. Cassimeris L, Pryer NK, Salmon ED. Real-time observations of microtubule dynamic instability in living cells. *J Cell Biol.* 1988;107:2223-31.
89. Belmont LD, Hyman AA, Sawin KE, Mitchison TJ. Real-time visualization of cell cycle-dependent changes in microtubule dynamics in cytoplasmic extracts. *Cell.* 1990;62:579-89.
90. Caplow M, Ruhlen RL, Shanks J. The free energy for hydrolysis of a microtubule-bound nucleotide triphosphate is near zero: all of the free energy for hydrolysis is stored in the microtubule lattice. *J Cell Biol.* 1994;127:779-88.
91. Dye RB, Flicker PF, Lien DY, Williams RC. End-stabilized microtubules observed in vitro: stability, subunit, interchange, and breakage. *Cell Motil Cytoskeleton.* 1992;21:171-86.
92. Sammak PJ, Borisy GG. Detection of single fluorescent microtubules and methods for determining their dynamics in living cells. *Cell Motil Cytoskeleton.* 1988;10:237-45.
93. Parsons SF, Salmon ED. Microtubule assembly in clarified *Xenopus* egg extracts. *Cell Motil Cytoskeleton.* 1997;36:1-11.
94. Wymer CL, Fisher DD, Moore RC, Cyr RJ. Elucidating the mechanism of cortical microtubule reorientation in plant cells. *Cell Motil Cytoskeleton.* 1996;35:162-73.
95. Schulze E, Kirschner M. Dynamic and stable populations of microtubules in cells. *J Cell Biol.* 1987;104:277-88.
96. O'Brien ET, Salmon ED, Erickson HP. How calcium causes microtubule depolymerization. *Cell Motil Cytoskeleton.* 1997;36:125-35.
97. Baas PW, Ahmad FJ. The plus ends of stable microtubules are the exclusive nucleating structures for microtubules in the axon. *J Cell Biol.* 1992;116:1231-41.
98. Hunt JM, Redman RS, Silinsky EM. Reduction by intracellular calcium chelation of acetylcholine secretion without occluding the effects of adenosine at frog motor nerve endings. *Br J Pharmacol.* 1994;111:753-8.
99. Oakley CE, Oakley BR. Identification of gamma-tubulin, a new member of the tubulin superfamily encoded by mipA gene of *Aspergillus nidulans*. *Nature.* 1989;338:662-4.

100. Melki R, Vainberg IE, Chow RL, Cowan NJ. Chaperonin-mediated folding of vertebrate actin-related protein and gamma-tubulin. *J Cell Biol.* 1993;122:1301-10.
101. Purohit A, Tynan SH, Vallee R, Doxsey SJ. Direct interaction of pericentrin with cytoplasmic dynein light intermediate chain contributes to mitotic spindle organization. *J Cell Biol.* 1999;147:481-92.
102. Schueler MG, Sullivan BA. Structural and Functional Dynamics of Human Centromeric Chromatin. *Annu Rev Genomics Hum Genet.* 2006.
103. Mitchison TJ, Kirschner MW. Properties of the kinetochore in vitro. I. Microtubule nucleation and tubulin binding. *J Cell Biol.* 1985;101:755-65.
104. Hirokawa N. Microtubule organization and dynamics dependent on microtubule-associated proteins. *Curr Opin Cell Biol.* 1994;6:74-81.
105. Chang-Jie J, Sonobe S. Identification and preliminary characterization of a 65 kDa higher-plant microtubule-associated protein. *J Cell Sci.* 1993;105 ( Pt 4):891-901.
106. Umeyama T, Okabe S, Kanai Y, Hirokawa N. Dynamics of microtubules bundled by microtubule associated protein 2C (MAP2C). *J Cell Biol.* 1993;120:451-65.
107. Vale RD, Toyoshima YY. Rotation and translocation of microtubules in vitro induced by dyneins from *Tetrahymena* cilia. *Cell.* 1988;52:459-69.
108. Sawin KE, Endow SA. Meiosis, mitosis and microtubule motors. *Bioessays.* 1993;15:399-407.
109. Howard J, Hudspeth AJ, Vale RD. Movement of microtubules by single kinesin molecules. *Nature.* 1989;342:154-8.
110. Hyman AA, Mitchison TJ. Two different microtubule-based motor activities with opposite polarities in kinetochores. *Nature.* 1991;351:206-11.
111. Ault JG, Rieder CL. Centrosome and kinetochore movement during mitosis. *Curr Opin Cell Biol.* 1994;6:41-9.
112. Adams MC, Salmon WC, Gupton SL, Cohan CS, Wittmann T, Prigozhina N, Waterman-Storer CM. A high-speed multispectral spinning-disk confocal microscope system for fluorescent speckle microscopy of living cells. *Methods.* 2003;29:29-41.
113. Bajer AS, Molè-Bajer J. Asters, poles, and transport properties within spindlelike microtubule arrays. *Cold Spring Harb Symp Quant Biol.* 1982;46 Pt 1:263-83.
114. Thompson-Coffe C, Coffe G, Schatten H, Mazia D, Schatten G. Cold-treated centrosome: isolation of centrosomes from mitotic sea urchin eggs, production of an anticontrosomal antibody, and novel ultrastructural imaging. *Cell Motil Cytoskeleton.* 1996;33:197-207.
115. Baas PW, Ahmad FJ, Pienkowski TP, Brown A, Black MM. Sites of microtubule stabilization for the axon. *J Neurosci.* 1993;13:2177-85.
116. Casal J, González C, Ripoll P. Spindles and centrosomes during male meiosis in *Drosophila melanogaster*. *Eur J Cell Biol.* 1990;51:38-44.

117. Jensen CG. Dynamics of spindle microtubule organization: kinetochore fiber microtubules of plant endosperm. *J Cell Biol.* 1982;92:540-58.
118. Bajer A S, Smirnova E A, Mole-Bajer J, Wawrowsky K A, Wolf R. Centrosomal complex is not needed for self-reorganization of the cytoskeleton in higher plants., in *Cold Spring Harbor Symposium.* (1993).
119. Wawrowsky K A, Wolf R, Mole-Bajer J, Bajer A S. Selforganizing properties of higher plant microtubules: Real-time observations of microtubule dynamics in higher plant cells show all properties of a self-organizing polymer-motor system., in *Cold Spring Harbor Symposium.* (1993).
120. Brandt R, Lee G. Orientation, assembly, and stability of microtubule bundles induced by a fragment of tau protein. *Cell Motil Cytoskeleton.* 1994;28:143-54.
121. Harris PJ, Clason EL. Conditions for assembly of tubulin-based structures in unfertilized sea urchin eggs. Spirals, monasters and cytasters. *J Cell Sci.* 1992;102 ( Pt 3):557-67.
122. Maekawa T, Leslie R, Kuriyama R. Identification of a minus end-specific microtubule-associated protein located at the mitotic poles in cultured mammalian cells. *Eur J Cell Biol.* 1991;54:255-67.
123. Gaglio T, Dionne MA, Compton DA. Mitotic spindle poles are organized by structural and motor proteins in addition to centrosomes. *J Cell Biol.* 1997;138:1055-66.
124. Pizon V, Gerbal F, Diaz CC, Karsenti E. Microtubule-dependent transport and organization of sarcomeric myosin during skeletal muscle differentiation. *EMBO J.* 2005;24:3781-92.
125. Bastiaens P, Caudron M, Niethammer P, Karsenti E. Gradients in the self-organization of the mitotic spindle. *Trends Cell Biol.* 2006;16:125-34.
126. Spurck TP, Stonington OG, Snyder JA, Pickett-Heaps JD, Bajer A, Mole-Bajer J. UV microbeam irradiations of the mitotic spindle. II. Spindle fiber dynamics and force production. *J Cell Biol.* 1990;111:1505-18.
127. Ault JG, Nicklas RB. Tension, microtubule rearrangements, and the proper distribution of chromosomes in mitosis. *Chromosoma.* 1989;98:33-9.
128. Bajer AS, Vantard M. Microtubule dynamics determine chromosome lagging and transport of acentric fragments. *Mutat Res.* 1988;201:271-81.
129. Cassimeris L, Salmon ED. Kinetochore microtubules shorten by loss of subunits at the kinetochores of prometaphase chromosomes. *J Cell Sci.* 1991;98 ( Pt 2):151-8.
130. Czaban BB, Forer A, Bajer AS. Ultraviolet microbeam irradiation of chromosomal spindle fibres in *Haemanthus katherinae* endosperm. I. Behaviour of the irradiated region. *J Cell Sci.* 1993;105 ( Pt 2):571-8.
131. Geuens G, Hill AM, Levilliers N, Adoutte A, DeBrabander M. Microtubule dynamics investigated by microinjection of *Paramecium* axonemal tubulin: lack of nucleation but

proximal assembly of microtubules at the kinetochore during prometaphase. *J Cell Biol.* 1989;108:939-53.

132. Gorbsky GJ, Borisy GG. Microtubules of the kinetochore fiber turn over in metaphase but not in anaphase. *J Cell Biol.* 1989;109:653-62.

133. Koshland DE, Mitchison TJ, Kirschner MW. Polewards chromosome movement driven by microtubule depolymerization in vitro. *Nature.* 1988;331:499-504.

134. Shelden E, Wadsworth P. Microinjection of biotin-tubulin into anaphase cells induces transient elongation of kinetochore microtubules and reversal of chromosome-to-pole motion. *J Cell Biol.* 1992;116:1409-20.

135. Hayden JH, Bowser SS, Rieder CL. Kinetochores capture astral microtubules during chromosome attachment to the mitotic spindle: direct visualization in live newt lung cells. *J Cell Biol.* 1990;111:1039-45.

136. Hays TS, Salmon ED. Poleward force at the kinetochore in metaphase depends on the number of kinetochore microtubules. *J Cell Biol.* 1990;110:391-404.

137. Mitchison TJ, Salmon ED. Poleward kinetochore fiber movement occurs during both metaphase and anaphase-A in newt lung cell mitosis. *J Cell Biol.* 1992;119:569-82.

138. Wawrowsky K A. Motion and Transport of Intracellular Particles during Mitosis, *Diploma Thesis.* (1991).

139. Beckerle MC. Microinjected fluorescent polystyrene beads exhibit saltatory motion in tissue culture cells. *J Cell Biol.* 1984;98:2126-32.

140. Coue M, Lombillo VA, McIntosh JR. Microtubule depolymerization promotes particle and chromosome movement in vitro. *J Cell Biol.* 1991;112:1165-75.

141. Amin-Hanjani S, Wadsworth P. Inhibition of spindle elongation by taxol. *Cell Motil Cytoskeleton.* 1991;20:136-44.

142. Bajer AS, Cypher C, Molè-Bajer J, Howard HM. Taxol-induced anaphase reversal: evidence that elongating microtubules can exert a pushing force in living cells. *Proc Natl Acad Sci U S A.* 1982;79:6569-73.

143. Shibaoka H, Nagai R. The plant cytoskeleton. *Curr Opin Cell Biol.* 1994;6:10-5.

144. Hard R, Allen RD. Behaviour of kinetochore fibres in *Haemanthus katherinae* during anaphase movements of chromosomes. *J Cell Sci.* 1977;27:47-56.

145. Bajer AS. Interaction of microtubules and the mechanism of chromosome movement (zipper hypothesis). 1. General principle. *Cytobios.* 1973;8:139-60.

146. Berg HC. Princeton University Press. Princeton, New Jersey: Princeton University Press; 1993.

147. Mitchison TJ. Mechanism and function of poleward flux in *Xenopus* extract meiotic spindles. *Philos Trans R Soc Lond B Biol Sci.* 2005;360:623-9.

148. Bajer AS, Smirnova EA. Reorganization of microtubular cytoskeleton and formation of cellular processes during post-telophase in haemanthus endosperm. *Cell Motil Cytoskeleton*. 1999;44:96-109.

## Danksagung

Diese Arbeit wäre ohne die tatkräftige Unterstützung vieler nicht zustande gekommen.

Besonders möchte ich meinem Betreuer, Dr. Rainer Wolf für seine unermüdliche Unterstützung und seine enorme Geduld danken. Er hat mich über die Jahre sowohl mit praktischem als auch persönlichem Engagement unterstützt. Er hat immer wieder sehr wertvolle Anregungen geliefert und ohne seine Inspiration auf dem Gebiet der Wahrnehmungsforschung, wäre diese Arbeit nicht zustande gekommen.

Er war ein guter Freund und hat jederzeit geduldig mit Rat und Tat zur Seite gestanden. Besonders danke ich auch Dorothea Wolf, die mit ihren ermutigenden und freundlichen Ratschlägen immer zur Seite stand und mit ihrer kreativen Kunst für Anregungen sorgte.

Prof. Dr. Dieter Weiss danke ich für den kreativen Raum, den er für mich an der Universität Rostock geschaffen hat, um neue Methoden in der Videomikroskopie, Datenübermittlung und Verarbeitung zu entwickeln. Er setzte für mich den Impuls, die Softwareentwicklung speziell in der biologischen Forschung voranzutreiben.

Den Leica Mitarbeitern Dr. Werner Knebel und Dr. Johan Engelhardt danke ich für meine Einführung in die Konfokalmikroskopie und die vielen Tips und Tricks, Diskussionen und Anregungen.

Prof. Dr. Shlomo Melmed danke ich für seine Unterstützung der Konfokalmikroskopie am Cedars-Sinai Medical Center. Er unterstützte das Labor sowohl finanziell als auch wissenschaftlich. Er hat viele neue Türen in der Erforschung der zellbiologischen Grundlagen von Hormonerkrankungen eröffnet.

Dr. Anat Ben Shlomo, Dr. Ning-Ai Liu, Dr. Vera Chesnokova und Dr. Ines Donangelo danke ich für die interessanten wissenschaftlichen Projekte, an denen wir in Los Angeles zusammenarbeiten konnten.

Dr. Andrew Bajer and Dr. Jadwiga Bajer danke ich für die Gelegenheit, an der Dynamik und Organisation der Mikrotubuli in der Pflanzenzelle arbeiten zu können.

Meinen Eltern danke ich, daß Sie mich für viele Jahre unterstützt haben ohne den Mut zu verlieren oder an dem Projekt gezweifelt zu haben.

## **Lebenslauf**

Name: **Kolja Alexander Wawrowsky**

geboren: 12.06.1963 in Düsseldorf

### **Ausbildung:**

1969 - 1974            Grundschule (Düsseldorf, Paulus Platz)

1974 - 1983            Humboldt-Gymnasium (Düsseldorf), Abschluss: Abitur

1983 - 1984            Grundwehrdienst

1984 - 1991            Studium der Biologie mit Nebenfach Physik an der Ludwig-Maximilian  
Universität Würzburg, Abschluss: Diplom

ab 1992                Promotionsstudium an der Fakultät für Biologie der Universität  
Würzburg, Betreuer: PD Dr. habil. Rainer Wolf.

### **Berufstätigkeit:**

Jan 1996 - Mai 1998            Softwareentwickler für Leica Microsystems, Heidelberg

Juni 1998 - September 2001    Applikationsentwickler für Leica Microsystems, Exton, USA

ab Oktober 2001            Manager der Konfokalmikroskopie am Burns und Allen  
Forschungszentrum des Cedars-Sinai Krankenhaus, Los Angeles,  
USA



## Publikationsliste

1. Lee BS, Fujita M, Khazenzon NM, Wawrowsky KA, Wachsmann-Hogiu S, Farkas DL, et al. Polycefin, a new prototype of a multifunctional nanoconjugate based on poly(beta-L-malic acid) for drug delivery. *Bioconjug Chem.* 2006;17:317-26.
2. Chen CR, Chazenbalk GD, Wawrowsky KA, McLachlan SM, Rapoport B. Evidence that Human Thyroid Cells Express Uncleaved, Single Chain Thyrotropin Receptors on their Surface. *Endocrinology.* 2006.
3. Gillingwater TH, Wishart TM, Chen PE, Haley JE, Robertson K, MacDonald SH, et al. The neuroprotective WldS gene regulates expression of PTTG1 and erythroid differentiation regulator 1-like gene in mice and human cells. *Hum Mol Genet.* 2006;15:625-35.
4. Scoles DR, Yong WH, Qin Y, Wawrowsky K, Pulst SM. Schwannomin inhibits tumorigenesis through direct interaction with the eukaryotic initiation factor subunit c (eIF3c). *Hum Mol Genet.* 2006;15:1059-70.
5. Barcia C, Thomas CE, Curtin JF, King GD, Wawrowsky K, Candolfi M, et al. In vivo mature immunological synapses forming SMACs mediate clearance of virally infected astrocytes from the brain. *J Exp Med.* 2006;203:2095-107.
6. Noushmehr H, D'Amico E, Farilla L, Hui H, Wawrowsky KA, Mlynarski W, et al. Fatty acid translocase (FAT/CD36) is localized on insulin-containing granules in human pancreatic beta-cells and mediates fatty acid effects on insulin secretion. *Diabetes.* 2005;54:472-81.
7. Ben-Shlomo A, Wawrowsky KA, Proekt I, Wolkenfeld NM, Ren SG, Taylor J, et al. Somatostatin receptor type 5 modulates somatostatin receptor type 2 regulation of adrenocorticotropin secretion. *J Biol Chem.* 2005;280:24011-21.
8. Abbud RA, Takumi I, Barker EM, Ren SG, Chen DY, Wawrowsky K, Melmed S. Early multipotential pituitary focal hyperplasia in the alpha-subunit of glycoprotein hormone-driven pituitary tumor-transforming gene transgenic mice. *Mol Endocrinol.* 2005;19:1383-91.
9. Liu NA, Liu Q, Wawrowsky K, Yang Z, Lin S, Melmed S. Prolactin receptor signaling mediates the osmotic response of embryonic zebrafish lactotrophs. *Mol Endocrinol.* 2005;20:871-80.
10. Suwelack D, Hurtado-Lorenzo A, Millan E, Gonzalez-Nicolini V, Wawrowsky K, Lowenstein PR, Castro MG. Neuronal expression of the transcription factor Gli1 using the Talpha1 alpha-tubulin promoter is neuroprotective in an experimental model of Parkinson's disease. *Gene Ther.* 2004;11:1742-52.

11. Wawrowsky K A, Molè-Bajer J, Wolf R, Bajer A S. Self organization of plant microtubule arrays can be modeled with l-system fractals. *Molecular Biology of the Cell (Suppl)*. 1999;10:256.
12. Bajer A S, Smirnova E A, Mole-Bajer J, Wawrowsky K A, Wolf R. Centrosomal complex is not needed for self-reorganization of the cytoskeleton in higher plants, in *Cold Spring Harbor Symposium* (1993).
13. Wawrowsky K A, Wolf R, Molè-Bajer J, Bajer A S. Selforganizing properties of higher plant microtubules: Real-time observations of microtubule dynamics in higher plant cells show all properties of a selforganizing polymer-motor system, in *Cold Spring Harbor Symposium* (1993).
14. Wawrowsky K A , Mole-Bajer J, Bajer A S . Selforganizing properties of higher plant microtubules: Real-time observations of microtubule dynamics in higher plant cells show all properties of a self-organizing polymer-motor system., in *Cold Spring Harbor Symposium* (1993).
15. Wawrowsky K A, Bajer A S, Molè-Bajer J. Fully Automated Analysis of Intracellular Traffic during Mitosis. *Molecular Biology of the Cell (Suppl)*. 1992;3.
16. Wawrowsky K. Motion and Transport of Intracellular Particles During Mitosis, in *Diploma Thesis* (1991).

## **Ehrenwörtliche Erklärung**

Hiermit erkläre ich ehrenwörtlich, dass die vorliegende Arbeit von mir selbständig und nur unter Verwendung der angegebenen Quellen und Hilfsmittel angefertigt wurde. Weiterhin habe ich noch keinen Promotionsversuch unternommen oder diese Dissertation in gleicher oder ähnlicher Form in einem anderen Prüfungsverfahren vorgelegt.

Los Angeles, 13. Februar 2007

Kolja Wawrowsky